

NOTICE WARNING CONCERNING COPYRIGHT RESTRICTIONS:

The copyright law of the United States (title 17, U.S. Code) governs the making of photocopies or other reproductions of copyrighted material. Any copying of this document without permission of its author may be prohibited by law.

Thermal Imaging for Robotic Applications in Outdoor Scenes

C. Caillas

CMU-RI-TR-90-08₂

**The Robotics Institute
Carnegie Mellon University
Pittsburgh, Pennsylvania 15213**

April 1990

©1990 Carnegie Mellon Univeristy

This research was sponsored by NASA under Grant NAGW 1175. C. Caillas is on leave of absence from GIAT (France): Industrial Group for Terrestrial Armements and is supported by DGA (France): General Delegation for Armement. His permanent address is: AMX-APX 13, route de la miniere, Satory 78013 Versailles (France). The views and conclusions contained in this document are those of the author and should not be interpreted as representing the official policies, either expressed or implied, of NASA or the US Government.

Contents

1	Introduction	1
2	Thermal Tutorial. Application: Thermal Imaging	3
2.1	General Principles	3
2.1.1	Infrared and Thermal Radiation	3
2.1.2	Basic Definitions for Thermal Radiation	4
2.1.3	Black and Real Body	5
2.2	Infrared Technologies	8
2.2.1	Thermal Camera	8
2.2.2	New Technology of Sensors	9
3	Thermal Imaging Model in Outdoor Scene	11
3.1	Modeling Body	12
3.2	Defining Orientation of the Sun	12
3.3	Modeling Total Radiation Falling on a Horizontal Plane	13
3.4	Modeling Heat Conduction	18
3.5	Modeling Heat Exchanges	19
3.6	Calculating Surface Temperature	21
3.6.1	Thermal Inertia Influence	23
3.6.2	Material Emissivity Influence	26
3.6.3	Material Reflectivity Influence	27
3.6.4	Wind Speed Influence	28
3.6.5	Latitude Influence	28
3.7	Calculating Thermal Inertia	28
3.8	Experiments	32
3.8.1	Acquiring Data	32
3.8.2	Interpreting Data	38
3.8.3	Using Data to Calculate Thermal Inertia	41
3.9	Limitations of the Model	41
3.10	How to Use the Model?	44

4 Thermal and Range Fusion 48

4.1 Thermal Imaging Segmentation 48

4.1.1 Splitting Method 48

4.1.2 Results 49

4.2 Range Segmentation 52

4.2.1 Range Jumps and Normal Variation Detection 54

4.2.2 Results 54

4.3 Thermal and Range Fusion 55

4.3.1 Principle of the Fusion 55

4.3.2 Results 58

5 Application for Autonomous Vehicles: a Case Study, the Mars Rover 60

5.1 Infrared Technology for Mars 60

5.2 Known Characteristics of Martian Materials 63

5.3 Determining Size of the Grain 63

5.3.1 Relation Thermal Inertia, Grain Size 64

5.3.2 Using the Model to Determine Grain Size 66

5.4 Vision Architecture to Identify Objects 67

5.5 Applications 69

5.5.1 Determining Footfall Positions 69

5.5.2 Determining Material Collection Site 71

6 Discussions and Future Work 73

A Analytical Calculations 76

A.1 One-dimensional Heat Equation 76

A.2 Calculating Body Temperature 77

B Phoenix Parameters 84

Table of Symbols 85

Acknowlegments 87

List of Figures

2.1	Thermal wavelengths in the spectrum of radiation	4
2.2	Blackbody radiation at different temperatures	7
2.3	Synoptic of a classical thermal camera	9
3.1	Semi-infinite body	13
3.2	Sun position from the Earth	14
3.3	What is solar declination?	14
3.4	Radiation reaching a horizontal surface	16
3.5	Heat exchanges	19
3.6	Surface temperature of material as a function of time and thermal inertia	25
3.7	Influence of the emissivity on surface temperature	26
3.8	Influence of the reflectivity on surface temperature	27
3.9	Influence of the wind speed on surface temperature	29
3.10	Influence of the latitude on surface temperature	30
3.11	Thermal inertia as a function of input parameters	31
3.12	Sandbox and big rock at the top	33
3.13	Thermal image of the sandbox at night (10:38pm)	34
3.14	Thermal image of the sandbox at night (3:36am)	34
3.15	Thermal image of the sandbox at sunrise, close to the contrast inversion (8:16am)	35
3.16	Thermal image of the sandbox during sunshine (10:21am)	35
3.17	Thermal image of the sandbox during sunshine (2:37pm)	36
3.18	Thermal image of the sandbox at sunset, close to the contrast inversion (6:09pm)	36
3.19	Calibration curve of the thermal camera	37
3.20	Experimental and theoretical temperature for sand and rock	40
3.21	Image of thermal inertia during sunshine (2:37pm)	42
3.22	Image of thermal inertia at night (3:36am)	42
3.23	Surface temperature of material as a function of time and thermal inertia at the equator, for $V_a = 0m/s$	46
3.24	Surface temperature of material as a function of time and thermal inertia at the equator, for $V_a = 10m/s$	47

4.1	Phoenix applied to nightly thermal image (10:38pm)	50
4.2	Phoenix applied to daily thermal image (2:37pm)	51
4.3	Phoenix applied to a thermal image: two rocks one big and one small are in the scene (10:38am)	52
4.4	Phoenix applied to an image of the sandbox taken by a black and white camera (10:38am)	53
4.5	Phoenix applied to an image of the sandbox taken by a black and white camera (1:45pm)	53
4.6	Range image of the sandbox (top) and reflectance image (bottom)	55
4.7	Range jump detection of the sandbox	56
4.8	Normal vector along x,y,z axis	56
4.9	Normal variation detection of the sandbox	57
4.10	Occlusion of two rocks in the field of view of the imager	58
4.11	Segmentation of the two rocks	59
5.1	The Ambler	61
5.2	Martian landscape viewed by the Viking 2 lander	61
5.3	Conductivity as a function of gas pressure	65
5.4	Temperature difference between several materials	68
5.5	Vision architecture for the Mars Rover	70
5.6	Pebble set on the soil (left), pebble at soil level (right)	72
A.1	Heat flux along the x-axis	76

List of Tables

3.1	Sand and rock characteristics	38
3.2	Thermal inertia of sand and rock	41
5.1	British Soil Classification	66

Abstract

This report describes thermal imaging techniques to identify different types of materials in outdoor scenes. First, we present the model that we developed to calculate the temperature of materials. By applying this model, we show how to calculate thermal inertia, a key physical characteristic of the material. Second, we analyze how applying vision segmentation algorithms to thermal images allows for discriminating between materials such as rock and sand. We then show how combining thermal and range information improves discrimination between occluding objects that are composed of the same material. Third, we examine how an autonomous robot can use these techniques to explore other planets. In particular, we show how a legged robot can use thermal inertia to select where to place its foot next or which material to sample.

Chapter 1

Introduction

This report describes thermal imaging techniques that can distinguish between different materials in outdoor scenes. We present a model of heat phenomena that permits calculating physical characteristics of real objects from thermal image data.

Although still a relatively new technology, thermal imaging has found, during the past ten years, applications in several fields (military, medical, inspection, ...). In military domain, for example, armored vehicles can be detected because their engines, tracks or wheels, and weapons, are usually warmer than the background. In medical domain, tumors in a human body can be detected because they are usually warmer than surrounding tissue of body.

Here, we investigate a new application field: **robotic sensing in outdoor scenes**. While many robots already incorporate visible light cameras such as black and white or color cameras, few of them use thermal imaging devices. One reason for not using thermal imaging techniques is that most robots are working in indoor environments where all objects tend to have the same temperature. In an outdoor environment, the objects are heated by the sun. Solar heating produces much greater diversity in object temperature depending on certain physical characteristics of the object.

Since thermal imaging is not often used by robotic researchers, **Chapter 2** presents basic notions about physics of thermal radiation and infrared technologies.

To understand the thermal behavior of natural objects in outdoor scenes, we have developed in **Chapter 3**, a novel model for calculating the temperature of the surface of objects by considering heat exchanges with the environment. By making several assumptions about the heat exchanges and the shape of the body, we obtain an expression of the temperature as a function of two main parameters: thermal inertia of the object viewed, and time of day at which the image is taken. We can therefore calculate the thermal inertia of bodies by using this expression of temperature, a thermal camera that gives temperature information and a watch that gives time. Finally, by using some table of physical constants, we can precisely relate the thermal inertia to the type of material. Thus, knowing the thermal inertia allows us, to some extent, to discriminate among different objects in the scene. Although assumptions of the model cover a broad class of conditions, quantitative results are not perfectly reliable because parameters other than the thermal inertia, temperature and

time involved in our model are difficult to model, for example meteorological parameters such as wind. On the other hand, qualitative results are sufficiently accurate to reliably distinguish materials. Results, obtained on a scene composed of sand and rock that are the main constituents of other planets such as Mars, fit fairly well with the real behavior of these materials. The application that we have in mind is an exploratory mission on another planet conceivably Mars.

We have a model describing the thermal behavior of bodies. We apply it for determining the thermal inertia of materials but quantitative results are not accurate enough to segment thermal image as a function of the thermal inertia information. We therefore explore pure computer vision techniques to discriminate between objects. Since we have an image of the scene, it is quite natural to apply vision techniques such as segmentation methods. Grouping portions of the image into units that are homogeneous with respect to the feature temperature results in a segmented image. We describe these techniques in **Chapter 4** and apply them on a scene composed of sand and rock. Segmenting techniques can handle many of the cases on Mars. But, we need other techniques to discriminate two objects that occlude each other. Because two objects composed of the same material will have the temperature, thermal imaging cannot be used to differentiate occluding objects. To solve this problem, we use 3D vision techniques. Segmentation of range images is performed by extracting features such as edges and surface normal variation that usually correspond to the contours of objects. We show that combining thermal imaging and 3D techniques allows us to handle most of the problems encountered on Mars. Calculating thermal inertia of the different regions in the image can then be performed to determine the type of materials.

Chapter 5 presents an application for thermal imaging: planetary exploration by an autonomous robot on another planet [3]. The robot, currently being developed at Carnegie Mellon University, is a six legged robot called Ambler. To explore new regions and collect material samples, the Ambler must traverse unknown and geographically diverse areas. For that purpose, the prototype of the robot constructs a geometric representation of the terrain. Understanding the geometry of the terrain is necessary but not sufficient to evaluate the safety of a proposed path for the Ambler. Information about soil properties would be a major advantage. In this chapter, we show how thermal imaging allows us to determine the type of the material such as sand by remotely determining the size of its grain. The legged robot can then use the grain size information to select where to place its feet or which material to sample.

The report concludes in **Chapter 6** by discussing the limitations of the previous methods and presenting future work.

Chapter 2

Thermal Tutorial. Application: Thermal Imaging

Thermal images are created by thermal cameras that basically transform thermal radiation from the scene in an electronic signal. The two goals of this tutorial are first to present basic notions about the physics of thermal radiation and then to present elementary knowledge about infrared technologies for thermal cameras.

In the rest of the chapters of this report, we will refer several times to this tutorial to precisely relate certain underlying concepts of physics, to define some parameters and to explain some formulas which will be used for calculation. This chapter is written for the reader who is unfamiliar with some of the basics of thermal imaging. The reader may opt to read this body of material now or he can refer back to this tutorial as he encounters unfamiliar terms or concepts.

2.1 General Principles

2.1.1 Infrared and Thermal Radiation

The infrared radiation is an electromagnetic radiation like the light or Hertzian waves. Electromagnetic waves occur over a wide range of wavelengths, from 10^{-16} m (cosmic waves) to 10^6 m (electric power waves). A schematic of the complete electromagnetic wave spectrum is shown in Figure 2.1. Thermal radiation is in the range $\lambda = 10^{-1}\mu m$ to $\lambda = 10^3\mu m$ that includes the visible spectrum, $0.4\mu m \leq \lambda \leq 0.7\mu m$. The spectrum of infrared radiation goes from the red to the millimetric waves that respectively correspond to 0.75 micrometers and 1 millimeter. As presented in Section 2.2.1, only a small part of this spectrum is used by current thermal cameras: the bands $3 - 5\mu m$ and $8 - 12\mu m$. Thermal radiation is emitted by atomic excitation of any substance. The difference between thermal radiation and other electromagnetic waves lies in the mechanism of formation: Thermal waves are caused by temperature excitation while other types of electro-magnetic waves

are caused by mechanisms such as the following: electron bombardment of a metal (X-rays), nuclear reactions (gamma rays), excitation of a crystal of substances (radio waves), and so on.

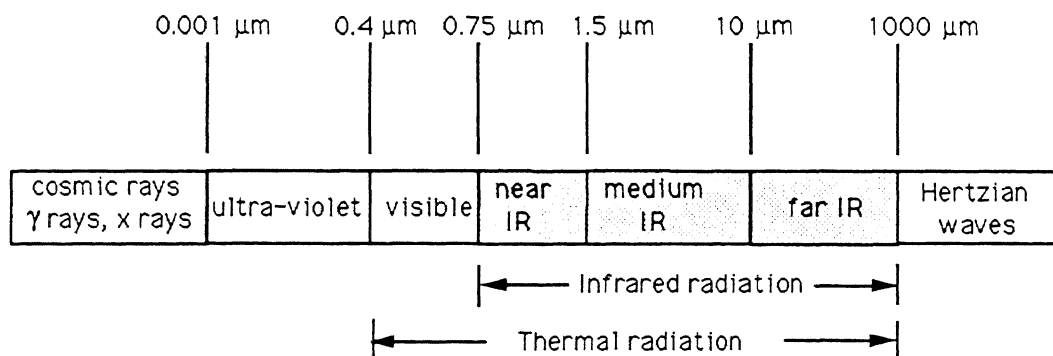


Figure 2.1: Thermal wavelengths in the spectrum of radiation

The only difference between thermal and infrared radiation is visible light as represented in Figure 2.1. As an object's temperature remains below approximately 1000K, object will emit infrared radiation that is also thermal radiation. In the other chapters of this report, we will use undifferently the terms infrared and thermal because terrestrial or martian temperature are only a few hundred Kelvins.

2.1.2 Basic Definitions for Thermal Radiation

The basic definitions used in thermal radiation theory that are necessary to understand the following chapters of this technical report are given in the present section. If you want to know more, consult the bibliography [11, 45, 46, 51].

- **Emissive Power**

The *emissive* power is the emitted radiation leaving a surface, per unit time and per unit area of surface (in W/m^2). The emissive power of a surface summed over all directions and all wavelengths is called total emissive power. The total emissive power is found to be dependent upon the temperature of the emitting surface, the substance of which the surface is composed, and the nature of the surface structure (i.e., roughness, etc.). The emission from a surface is distributed among the wavelengths in the thermal band. The monochromatic emissive power, denoted by the symbol E_λ is then defined as the rate, per unit of area, at which a surface emits thermal radiation at a particular wavelength λ . Thus, the total and monochromatic emissive powers are related by

$$E = \int_0^\infty E_\lambda d\lambda \quad (2.1)$$

- **Radiosity**

The emissive power does not include any energy resulting from the reflection of any incident radiation. Indeed, all the radiation leaving a surface that includes reflected energy is called radiosity. Since there is almost no reflected energy in the infrared wavelength bands used by thermal cameras, the radiosity is the same as the emissive power and those two terms will be used undifferently to denote the infrared radiation leaving the body.

- **Irradiation**

Irradiation is the term used to denote the rate per unit time and unit area at which thermal energy is incident on a surface (in W/m^2). The irradiation incident on a surface is the result of emissions and reflections from other surfaces and may be spectrally dependent.

$$G = \int_0^{\infty} G_{\lambda} d_{\lambda} \quad (2.2)$$

where G_{λ} and G are respectively the monochromatic and total irradiation.

In the following chapters, we will use the notions of emissive power (or radiosity) E , irradiation G to express heat exchanges between body and environment. Indeed, E will also be used to denote in Chapter 3 all other kinds of energy such as reflected, convective and conducted energy leaving the body surface.

2.1.3 Black and Real Body

- **Blackbody**

The concept of blackbody is useful in order to describe the radiation characteristics of real surfaces. A blackbody is an ideal body that one cannot find in the nature. By definition, it is able to absorb all incident energy. Consequently, that means that there is no reflected and no transmitted energy: $\alpha = 1$ and $\rho = \tau = 0$ where α is the absorptivity, ρ is the reflectivity and τ is the transmissivity of the material. The term blackbody is used because of the similarity to a black surface absorbing all incident radiation in the visible range. Since a blackbody absorbs all the incident radiation, the only radiation from a blackbody is original emission. The monochromatic emitted radiation E_{λ} such as defined previously depends on the wavelength λ and the temperature T of the surface and is given by Planck's law [46].

$$E_{\lambda} = \frac{c_1}{\lambda^5 (e^{\frac{c_2}{\lambda T}} - 1)} \quad (2.3)$$

where

$$\begin{cases} c_1 = 2\hbar c^2 \\ c_2 = \hbar c/k_B \\ k_B = 1.38 \times 10^{-23} JK^{-1} : \text{Boltzman constant} \\ \hbar = 6.62 \times 10^{-34} Js^2 : \text{Planck constant} \\ c = 3 \times 10^8 ms^{-1} : \text{light speed in the vaccum} \end{cases} \quad (2.4)$$

The monochromatic emissive power E_λ can be represented as a function of λ and T by the set of curves in Figure 2.2. Several comments should be made about these curves.

1. Note the logarithmic scale of the abscissa and ordinate. Because of the logarithmic scale of the abscissa, the major part of the emitted energy (about 75%) lies to the right of the maximum.
2. At all wavelengths, the emissive power increases with the temperature.
3. Solar radiation ($T = 5800K$) has its peak power in the middle of the visible light range.
4. The coordinates of the maximum of the peaks of the curves are bound by the relation called Wien's displacement law $\lambda T = 2897.8 \mu mK$.
5. By integrating Planck's law over the entire spectrum, one gets the emissive power E that only depends on the temperature. This dependence is called the Stephan-Boltzman law:

$$E = \sigma T^4 \quad (2.5)$$

in which σ is the Stephan-Boltzman constant. E is a function of the fourth power of the temperature which means that E increases with the temperature. This law is very important since it calculates the energy lost by radiation by the surface. It will be used in Chapter 3 to calculate heat exchanges between surfaces and their environment. In the mechanism of heat transfer, when the temperature is greater than 1000K, heat radiation usually dominates the other two types of heat transfer, conduction and convection. For terrestrial or martian temperature (a few hundred Kelvins), we will need to take into account these other types of heat transfer for modeling body temperature in Chapter 3.

• Real body

A real body exhibits an absorptivity α less than unity because it reflects and transmits some part of the received energy [11, 45, 46, 51]. Its value may depend on the wavelength of the incident radiation. The radiant characteristics of real surfaces differ from blackbody surfaces in different ways. First the monochromatic emissive power of a real surface at a given temperature has not the same amount and the same spectral distribution as a blackbody surface. Unlike blackbody surfaces, real surfaces may also exhibit non diffuse behavior. For real bodies one defines a coefficient $\epsilon(\lambda)$ called monochromatic emissivity. If $E(\lambda, T)$ represents the hemispherical monochromatic emissive power of a real surface at the temperature T and

monochromatic emitted radiation E_λ in $\text{W}/\text{cm}^2/\mu\text{m}$

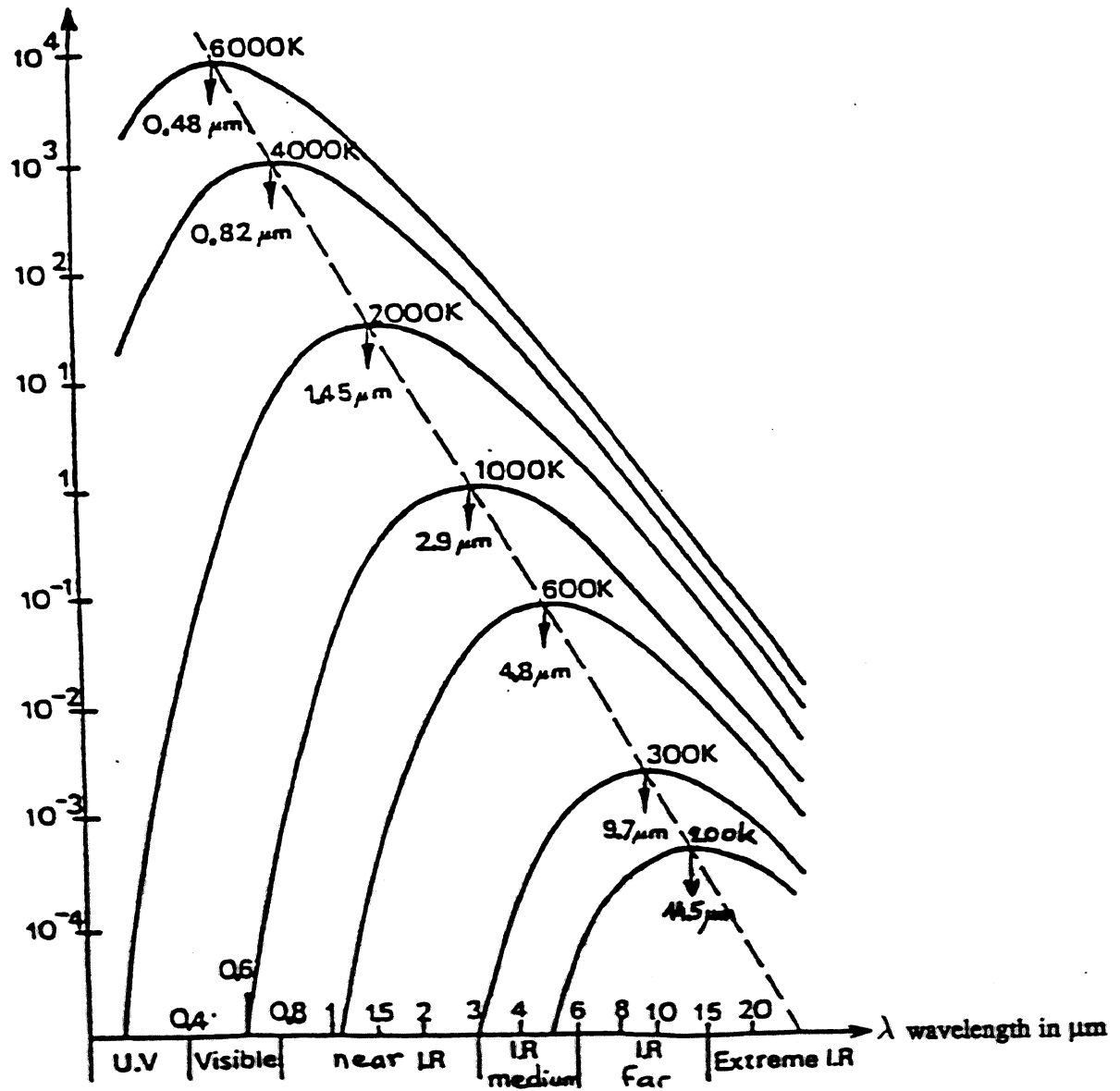


Figure 2.2: Blackbody radiation at different temperatures

$E_b(\lambda, T)$ the hemispherical emissive power for the blackbody then $\epsilon(\lambda, T)$ is defined as the ratio between these two powers:

$$\epsilon(\lambda, T) = \frac{E(\lambda, T)}{E_b(\lambda, T)} \quad (2.6)$$

However, the temperature dependence is generally small and ignored. Moreover it may be noted that the emissivity of certain surfaces shows a strong dependence with the wavelength whereas for others it is almost constant. Bodies with ϵ equal to a constant (independent of λ) are called grey bodies. The hemispherical emissive power is then given by :

$$E = \epsilon \sigma T^4 \quad (2.7)$$

In the following chapters, we will consider that bodies are grey bodies since it is a good approximation for natural bodies in outdoor scenes. We will use Equation 2.7 to calculate the amount of radiation emitted by bodies in outdoor scenes.

2.2 Infrared Technologies

2.2.1 Thermal Camera

Most of the infrared cameras are built on the same model. The detection chain integrates the following elements [38, 50]:

- A window protecting the optical system and allowing infrared light to enter.
- An optical system for focusing and correcting the chromatical and spherical aberrations.
- A scanning system consisting of rotating mirrors allows the detector to see the entire scene by sequentially analyzing the image.
- A system of infrared filters for selecting the desired wavelength band.
- A sensor that transforms the infrared thermal energy into an electrical signal. Two types of configuration are distinguished for the detectors: serial and parallel. The configuration is serial when the barrette of detectors is horizontal and parallel when the barette is vertical. The scanning of the image is done line by line and frame by frame. Figure 2.3 gives an overview of a classical thermal camera.
- An amplifier for the electrical signal.

Since it does not exist detectors with enough cells, manufacturers use detectors with a limited number of elements. The most simple camera uses a mono-element detector. The structures of sensors used for thermal imaging are photodiode, photocapacity, photoconductor or pyroelectric [2]. The detectors are either sensitive in the $3 - 5\mu m$ or the $8 - 12\mu m$ bands. There are two main reasons why manufacturers use these two bands:

- The main part of the radiant energy is emitted in those two bands for terrestrial applications where objects have a typical temperature of $300K$ (see Figure 2.2). Because the temperature on Mars is much lower than on Earth, Section 5.1 will explain that these wavelength bands are not satisfactory for applications on Mars.
- They correspond to transmission windows in the atmosphere. Outside these windows, the infrared energy is attenuated when propagating in the atmosphere essentially caused by carbon dioxide and water vapor [53].

All the technologies of sensors except pyroelectric technology involve a cooling system which minimizes the noise present in the electronic signal and allows to get the high necessary detectivity. The detector is cooled for the band $8 - 12\mu m$ at $-190^{\circ}C$ (liquid nitrogen in a dewar bottle), or cooled for the band $3 - 5\mu m$ at $70^{\circ}C$.

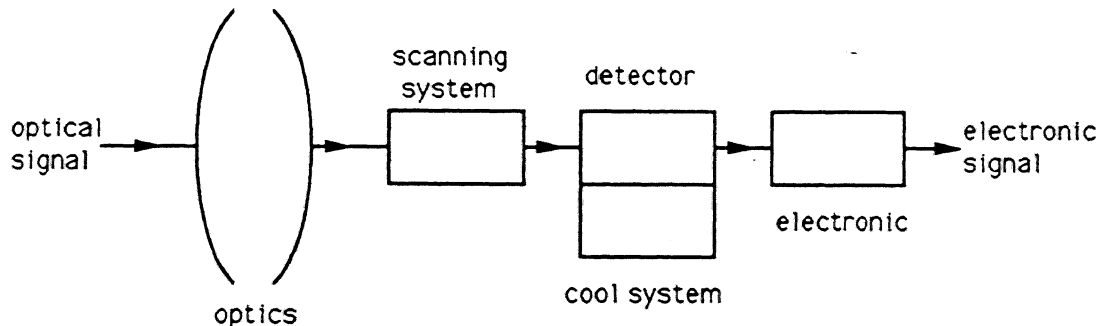


Figure 2.3: Synoptic of a classical thermal camera

2.2.2 New Technology of Sensors

Nowadays, three types of technology emerge [12]:

- Photovoltaic barrette coupled with a CCD sensor in the $3 - 5\mu m$ and $8 - 12\mu m$ bands.
- Schottky effect used in conjunction with a metal-semiconductor (MS) in the $3 - 5\mu m$ band. The most well known are made of PtSi. Their resolution can reach 512×512 pixels that is comparable with performances of color CCD cameras.

- Metal-insulator-semiconductor (MIS) in the $3 - 5\mu m$ band made of InSb whose resolution can be 128×128 pixels.

The most promising technique seems to be the hybridation of detectors PV HgCdTe with a silicon CCD circuit (IRCCD PV HgCdTe) that works in the $2 - 12\mu m$ band. This technique currently allows to build detectors 64×64 in resolution.

It appears that the $8 - 12\mu m$ is the technology the best adapted for thermal imaging at terrestrial temperature but is also the less developed. Cameras with baretttes of cells is only a transitionally step. New sensor technologies begin to appear on the market. The basic idea is to build sensors with many more cells in order to avoid the scanning system to see all the scene. Thus, a thermal camera would look like more to a conventional camera such as a CCD camera. An important work concerning the infrared imagers for the future is being done. This work concerns the structure of the elementary point as well as the architecture of the focal plane. Conceptually, sensors 1000×1000 pixels are foreseen for the year 2000 [2].

Chapter 3

Thermal Imaging Model in Outdoor Scene

In this chapter we present the model that we developed to understand the thermal behavior of materials in outdoor scene. By applying the physical laws of heat transfer, we show that it is possible to calculate body temperature as a function of two main parameters: time (t) and thermal inertia (I), where I is a physical characteristic of materials. The basic idea of the model is to derive the thermal inertia as a function of temperature and time. Since the thermal inertia is a characteristic of materials, its knowledge should allow us to determine the type of materials by using tables of physical constants. There is however a fundamental difficulty behind this reasoning because the measurement of thermal inertia does not necessarily identify a single material. In the following, we will assume that we are not in that case because materials such as sand and rock that we are studying more particularly in this report have different thermal inertia. For interpreting outdoor scenes, one can notice that other approaches than using thermal inertia information have been investigated [35]. For example, it was shown that the ratio between the conducted and absorbed heat fluxes in the body are useful features. An approach for modelling outdoor scene objects which are imaged by thermal cameras is also presented in [10].

To calculate the a priori unknown thermal inertia, we need to know body temperature information. In Section 3.8, we will acquire body temperature by using a thermal imager that delivers radiosity information¹ for every pixel in the image. We also need to model body temperature. To do that, we need to model the different components of our outdoor problem. In Section 3.1, we model the shape of the body. In Section 3.2, we define the position of the sun relating to the body. In Section 3.3 we model the radiation falling on the body. In Section 3.4 and Section 3.5, we model respectively the conduction of heat inside the body and the heat exchanges between the body and its surrounding environment. Modeling heat exchanges at the surface of the body leads to an equation called boundary condition while modeling conduction of heat leads to the heat conduction equation. These two equations allow us, in Section 3.6, to express the temperature as a function of numerous elementary parameters. These parameters include solar time, thermal inertia, latitude, solar declination, wind speed, material emissivity, material reflectivity, atmosphere transmissivity

¹ See Chapter 2 for the definition of the radiosity.

and atmosphere temperature. They will be introduced and defined along the presentation of the model.

Then, we present results of experiments that used two kinds of materials: sand and rock. Lastly, we analyze in details the different limitations of the model for determining accurate values of temperature or thermal inertia.

3.1 Modeling Body

We model the body as an homogeneous semi-infinite body whose surface is an horizontal plane (see Figure 3.1). The assumption of homogeneity will allow us to consider that the physical characteristics of body such as conductivity k , density ρ_m and specific heat c_p are the same everywhere within the body. Since the body is supposed to be semi-infinite with a planar surface, we may consider that the flux of heat is monodimensional and flows in a direction which is perpendicular to the surface. Practically, a body can be considered semi-infinite if its dimensions are sufficiently large. The calculation of body dimension essentially depends on its capacity to conduct heat. If the body does not easily conducts heat then its dimensions can be small since interactions from different parts of the body are limited; otherwise, its dimensions must be larger. More precisely, the dimensions depend on k , ρ_m and c_p as presented in Section 3.9. Moreover, the surface of the body is considered to be horizontal in order to simplify the mathematical aspect of modeling radiation falling on the body and exchanging energy with its environment.

Although this modeling does not correctly take into account the real shape of body, it is often used in heat transfer problems to find approximate solutions. A more realistic modeling would be to model the surface of the body by juxtaposing elementary planes whose orientation can vary. The resolution of the problem is then much more delicate because the radiation falling on inclined planes is more difficult to model than for horizontal planes. Heat fluxes from different planes of the same object can interact with each other thereby leading to a complex heat transfer problem. For such complex geometries, analytical solutions can not always be found and we are forced to use numerical calculations by a finite element method [44]. For simplicity, we will limit our analysis to the case of the horizontal semi-infinite body. We also assume that the body does not contain any internal heat source which is, in general, the case for natural objects.

3.2 Defining Orientation of the Sun

In this section, we present the two angles usually used to position the sun [28]. One of this angle, the solar altitude will be used in the following to calculate solar radiation falling on the body. Let's consider a point noted P at the surface of the Earth. From this point, imagine the plane tangent to the planet; this plane defines the horizon. We reference this plane by two vectors indicating the directions South-North (S-N) and East-West (E-W). The position of the sun is then specified in

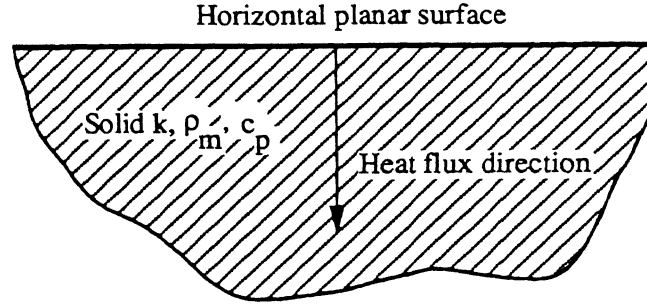


Figure 3.1: Semi-infinite body

terms of two angles: the solar altitude angle α_s , and the solar azimuth angle a_s , as represented in Figure 3.2. The solar altitude angle α_s measures the angular distance of the sun from the horizon whereas the azimuth angle measures the sun angular distance from the south direction. The solar altitude depends upon the solar time, solar declination δ , latitude L and angular speed of the Earth ω ($\omega = 2\pi/24$) according to the following formula whose geometric demonstration can be found in [28]:

$$\sin \alpha_s = \sin L \sin \delta - \cos L \cos \delta \cos \omega t \quad (3.1)$$

Since in the following of the sections, we are only interested in modeling the radiation falling on a horizontal plane, a_s is not needed. Only the solar altitude angle α_s is used. The solar declination angle δ measures the angle between the Earth-Sun vector and the equatorial plane as represented in Figure 3.3. Notice that sunrise and sunset occur when the solar altitude angle α_s is 0. Then, by applying Equation 3.1, we find that the solar time t for sunrise (t_{sr}) and for sunset (t_{ss}) are respectively:

$$t_{sr} = (\pi/\omega) \left[1 + (1/\pi) \cos^{-1}(-\tan L \tan \delta) \right] \quad (3.2)$$

$$t_{ss} = (\pi/\omega) \left[1 - (1/\pi) \cos^{-1}(-\tan L \tan \delta) \right] \quad (3.3)$$

The expression of t_{sr} and t_{ss} above, will be used to calculate the temperature of objects in Section 3.6.

3.3 Modeling Total Radiation Falling on a Horizontal Plane

One of the most important points in determining the temperature of bodies in an outdoor scene is to be able to know accurately enough the magnitude of solar radiation. In this section, we model solar radiation by making several assumptions.

The total radiation G also called irradiation (see the definition in Section 2.1.2) falling on a body can be decomposed in three parts: G_s that is directly communicated by the sun to the body, G_a that

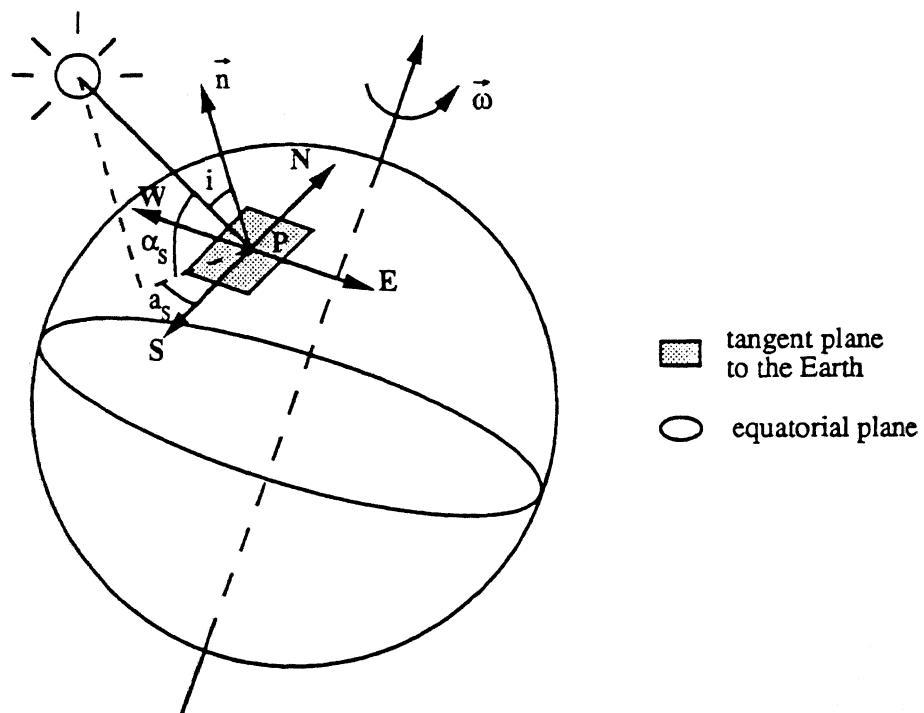


Figure 3.2: Sun position from the Earth

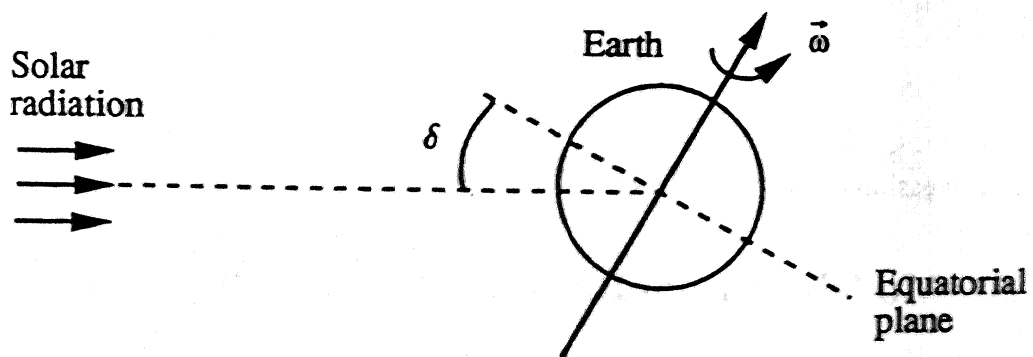


Figure 3.3: What is solar declination?

is first absorbed by the atmosphere and then reemitted in all directions, G_g that is first absorbed by the ground and then diffused in all directions.

$$G = G_s + G_a + G_g \quad (3.4)$$

The goal of the modeling is to express these three components as a function of the basic parameters (in particular solar time). As stated in Section 3.1, the body will be considered as semi infinite with a planar and horizontal surface.

• Direct Solar Radiation

Direct solar radiation G_s is dependent on the cloudiness of the sky [36, 39]. For example, sun radiation can be scattered by a factor of 80% due to the presence of clouds. We limit our analysis to the case of a clear sky without any clouds.

To express direct solar radiation, we introduce the parameter called atmosphere transmissivity. The atmosphere transmissivity, τ , is the ratio of the direct solar radiation G_s reaching the Earth over the radiation G_0 outside the atmospheric layer² before it becomes attenuated by the atmosphere. In other words, G_s is proportional to τ and G_0 . Furthermore, the direct solar radiation that reaches the horizontal planar surface is proportional to $\cos i$ where i is the solar incidence angle measured between the normal vector \vec{n} to the horizontal surface and the direction of the solar beams (see Figure 3.2). The direct solar radiation G_s can therefore be expressed by the relation:

$$G_s = \tau G_0 \cos i \quad (3.5)$$

In fact, the atmosphere transmissivity τ is a function of the length of the path for the solar beams through the atmosphere. The path through the atmosphere is itself a function of the solar incidence angle i of the sun in the sky [28, 39]; for example, at sunset and sunrise, the path through the atmosphere is longer than at noon. Therefore, τ is a function of i . As a first approximation, we will however consider that τ is a constant.

Because i and α_s are complementary angles (see Figure 3.2), we have:

$$\cos i = \sin \alpha_s \quad (3.6)$$

By replacing $\sin \alpha_s$ by its expression given in Equation 3.1, we obtain the relation between i , L , δ and t :

$$\cos i = \cos L \cos \delta \cos [\omega(t - 12)] + \sin L \sin \delta \quad (3.7)$$

By replacing Equation 3.7 in Equation 3.5, G_s becomes:

$$G_s = \tau G_0 \cos L \cos \delta \cos [\omega(t - 12)] + \sin L \sin \delta \quad (3.8)$$

² G_0 is called solar constant. Although the solar output varies slightly over a sunspot cycle, the solar constant remains within one percent of 1353 W/m^2 .

This expression is valid only during the day, between sunrise and sunset ($t_{sr} \leq t \leq t_{ss}$), when the plane does intercept the radiation emitted by the sun. During the night ($0 \leq t \leq t_{sr}$ or $t_{ss} \leq t \leq 2\pi/\omega$), $G_s = 0$. Then:

$$G_s(t) = \begin{cases} \tau G_0 \{ \sin L \sin \delta + \cos L \cos \delta \cos [\omega(12 - t)] \} & \text{if } t \in [t_{sr}, t_{ss}] \\ 0 & \text{otherwise} \end{cases} \quad (3.9)$$

that is graphically represented in Figure 3.4 for one entire day.

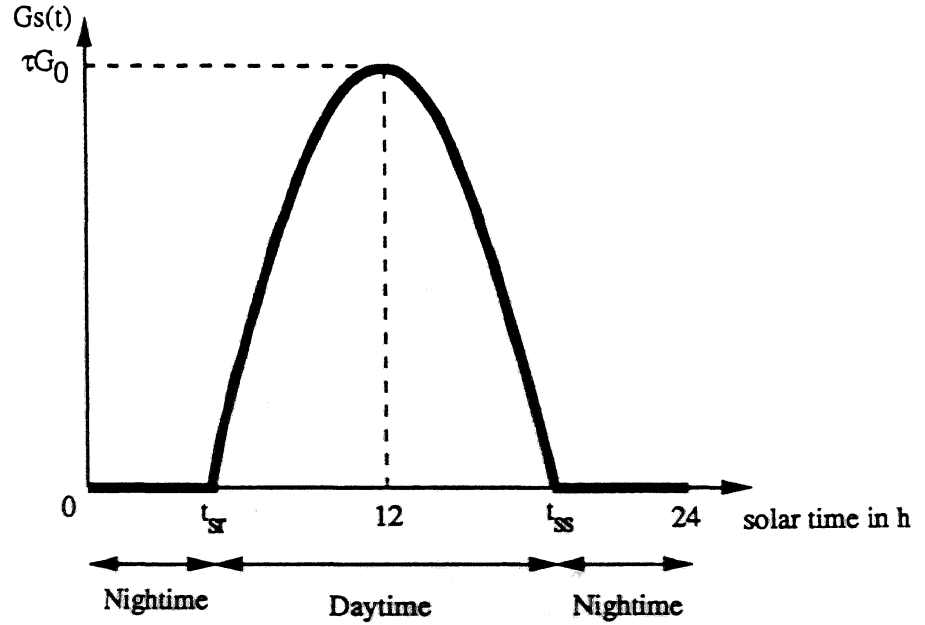


Figure 3.4: Radiation reaching a horizontal surface

- **Diffuse Radiation from the Atmosphere**

The diffuse radiation or emitted radiation from the atmosphere G_a reaching the surface can be written:

$$G_a = \epsilon_a \sigma T_a^4 \quad (3.10)$$

where G_a consists of the following parameters: atmosphere emissivity (ϵ_a), the Stephan-Boltzman constant (σ) and the atmosphere temperature T_a . The complete modeling of G_a takes into account the fact that the emissivity of the atmosphere depends upon the atmosphere temperature and the atmosphere temperature itself, depends upon the time. First, we model the atmosphere emissivity ϵ_a by using the relation presented in [53] (see page 3-15):

$$\epsilon_a = 1 - 0.261 \exp \left[-7.77 \times 10^{-4} (273 - T_a)^2 \right] \quad (3.11)$$

Second, we model T_a as a sinusoidal function of time that is usually a good approximation of the atmosphere temperature by clear sky:

$$T_a = T_1 - T_2 \sin(\omega t) \quad (3.12)$$

where T_1 and T_2 are constants depending on experimental conditions (see Section 3.8 for details about the choice of these parameters). For simplicity, T_a is set to its mean value T_1 in Equation 3.11. Finally, from Equation 3.10, Equation 3.11 and Equation 3.12, it comes

$$G_a = \left\{ 1 - 0.261 \exp \left[-7.77 \times 10^{-4} (273 - T_1)^2 \right] \right\} \sigma [T_1 - T_2 \sin(\omega t)]^4 \quad (3.13)$$

• Diffuse Radiation from the Ground

The ground is considered to be a horizontal plane. Since we have also modeled the body by a horizontal plane, we can consider that the horizontal object plane does not intercept the radiation emitted by the ground. Therefore the body does not receive any energy from the ground and $G_g = 0$. The object does only receive some radiation from the sky. One can notice that for an inclined plane, the diffuse radiation from the ground would not be equal to zero since the plane would face the ground. The modeling of this radiation in the case of an inclined plane can be found in [39] but will not be used in this report.

• Total Radiation

Finally, by using Equation 3.9 and Equation 3.13, we find the complete expression of the radiation $G = G_s + G_a$ falling on a horizontal plane:

$$G(t) = \begin{cases} \tau G_0 \{ \sin L \sin \delta + \cos L \cos \delta \cos [\omega(12 - t)] \} + \epsilon_a \sigma [T_1 - T_2 \sin(\omega t)]^4 & \text{if } t \in [t_{sr}, t_{ss}] \\ \epsilon_a \sigma [T_1 - T_2 \sin(\omega t)]^4 & \text{otherwise} \end{cases} \quad (3.14)$$

where ϵ_a is expressed by Equation 3.11. One can notice that $G(t)$ is a periodic function whose period is $2\pi/\omega = 24h$.

In conclusion of this section, the important point to notice is that we were able to analytically model the radiation G that falls on a horizontal plane as a function of the following parameters: solar time t , latitude L , solar declination δ , transmissivity of the atmosphere τ , solar constant G_0 and temperature of the atmosphere as defined by its mean value T_1 and amplitude T_2 . This analytical modeling will allow us to find in Section 3.6 an analytical expression of the temperature for understanding the thermal behavior of bodies. A better way to know total solar radiation would be simply to measure it. Although this method would give more accurate values, we do not investigate it in this report because it involves the search of a numerical solution for the temperature while we are looking for an analytical solution.

3.4 Modeling Heat Conduction

When different parts of a body are at different temperatures heat flows from the hotter parts to the cooler parts. This phenomenon is at the origin of the conduction of heat in solids (and also in gases and liquids). Experiments have shown that the rate of heat flow from one point to another separated by the distance Δx and with a difference of temperature ΔT is directly proportional to ΔT and inversely proportional to Δx (the coefficient of proportionality is called conductivity noted k). Therefore, the radiation conducted in the interior of the body and noted E_{cd} can be written in one dimension:

$$E_{cd} = -k \left(\frac{\partial T(x, t)}{\partial x} \right) \quad (3.15)$$

if we suppose $T(x, t)$ as being a continuous function whose derivatives exist. Starting from that basic relation, it is possible to show [40] (page 5-4) that the variation of temperature of bodies is governed by an equation called heat conduction equation that can be written in its most general form as follows:

$$\rho_m c_p \frac{\partial T}{\partial t} = \nabla \cdot (k \nabla T) \quad (3.16)$$

where

- T is a function of point coordinates (x, y, z) and time t ,
- The symbol \cdot denotes the dot product,
- ∇ is the gradient operator,
- $\nabla \cdot$ is the divergence operator.

Equation 3.16 can be simplified by taking into account the different assumptions of our model. If we assume the body modeled in Section 3.1, then, the conductivity, k , is a constant since the material is homogeneous. Moreover, the heat flows in only one direction noted x . Therefore the temperature of a point only depends on its coordinate x and not on y and z . Equation 3.16 can then be written as a differential equation of the second order depending on time t and depth x in the material.

$$\frac{\partial T(x, t)}{\partial t} = a \frac{\partial^2 T(x, t)}{\partial x^2} \quad (3.17)$$

where $a = k/(\rho_m c_p)$ is called the diffusivity of the material. A demonstration of Equation 3.17 is presented in Section A.1 in order to precisely understand its origin.

3.5 Modeling Heat Exchanges

In this section, we model the heat exchanges at the surface of the body as schematically represented in Figure 3.5. As we have seen in Section 3.3, the sun is the heat source emitting some radiation G called irradiation. The body reflects one part E_r of the incident energy, transmits by conduction one other part E_{cd} in the perpendicular direction Ox of the surface of the body³ and absorbs the last part of energy. This absorbed energy is reemitted by radiation E_{rad} and convection E_{cv} . The basic

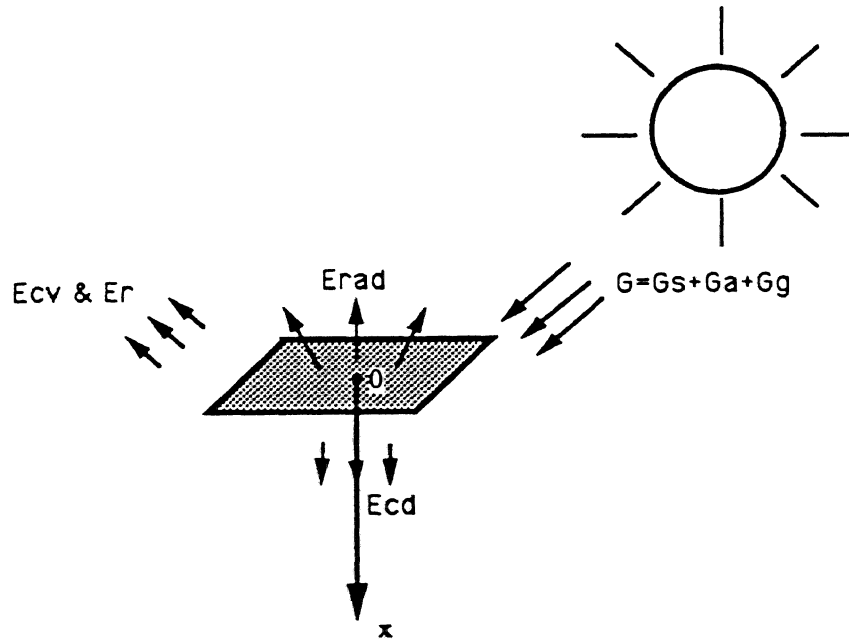


Figure 3.5: Heat exchanges

relation that bounds G , E_r , E_{cd} , E_{rad} and E_{cv} is the equation of energy conservation:

$$G = E_r + E_{rad} + E_{cd} + E_{cv} \quad (3.18)$$

Since we have already discussed G in Section 3.3, the remainder of the present section expounds upon the four terms in the above equation.

- **Reflected Radiation**

The reflected part of G can be written:

$$E_r = \rho G \quad (3.19)$$

where ρ is the reflectivity of the surface.

³The axis Ox is such that the origin O is placed at the surface of the object.

- **Conductive Radiation**

The conductive radiation E_{cd} through the body is proportional to the gradient of temperature as a function of the depth x in the material (see Equation 3.15). By applying this equation for $x = 0$, the radiation conducted at the surface of the body can be written:

$$E_{cd} = -k \left(\frac{\partial T(x, t)}{\partial x} \right)_{x=0} \quad (3.20)$$

- **Emitted Radiation**

By applying Equation 2.7, we can see that the emitted radiation from the surface is:

$$E_{rad} = \epsilon_s \sigma T^4(0, t) \quad (3.21)$$

where ϵ_s is the body emissivity and $T(0, t)$ is the surface temperature at time t .

- **Convective Radiation**

The convective radiation E_{cv} is proportional to the difference of temperature between the surface and the atmosphere:

$$E_{cv} = h[T(0, t) - T_a(t)] \quad (3.22)$$

In this equation, the coefficient of convection h depends on wind speed V_a [53] (page 3-15) and can be approximate by the following relation:

$$h = 4 + 3.8V_a^{0.8} \quad (3.23)$$

if the dimensions of the regions are on the order of 5m that corresponds to a mean value for outdoor object dimensions and if the mean difference of temperature between the surface and the atmosphere is about 10°C.

Then, by replacing the expressions found in Equation 3.19, and Equation 3.22 the heat balance equation can be written:

$$(1 - \rho) [G_s(t) + G_a(t)] = \epsilon_s \sigma T^4(0, t) + h[T(0, t) - T_a(t)] - k \left(\frac{\partial T(x, t)}{\partial x} \right)_{x=0} \quad (3.24)$$

where G_s is expressed by Equation 3.9 and G_a is expressed by Equation 3.13.

3.6 Calculating Surface Temperature

The variation of the Earth temperature has been discussed by many authors [25, 27, 36, 42, 48]. In solar radiation literature, we found some models for calculating the body temperature but usually they can only be applied in very specific cases. For instance, the temperature of an object has been calculated at the equator, in the ideal case where there is no convective heat transfer with the atmosphere [6, 9, 16]. To get the expression of the surface temperature, we have to solve the following system of two equations:

$$\begin{cases} \frac{\partial T(x, t)}{\partial t} = a \frac{\partial^2 T(x, t)}{\partial x^2} \\ (1 - \rho) [G_s(t) + G_a(t)] = \epsilon_s \sigma T^4(0, t) + h[T(0, t) - T_a(t)] - k \left(\frac{\partial T(x, t)}{\partial x} \right)_{x=0} \end{cases} \quad (3.25)$$

The first equation, called the equation of heat conduction, is a differential equation of the second order of the variables x and t that describes the temperature behavior inside the body (see Section 3.4). The second equation, the boundary condition equation, binds T and t at the surface of the body (see Section 3.5).

The boundary condition equation is a non-linear function of T since $T^4(0, t)$ occurs in this equation. To solve this system of equations, it is necessary to linearize the second equation. This consists of finding a linear approximation of the term $\sigma T^4(0, t)$. Such an approximation is given in [53] page 3-16 and can be written as follows for T expressed in K :

$$\sigma T^4 \approx A + BT \text{ where } A = -945 \text{ and } B = 4.62 \quad (3.26)$$

The equality in the above equation is obtained for $T = 273K$ ($0^\circ C$) that is taken as a mid value for the temperature. The range of material temperatures in which we are interested on do not exceed $323K$ ($50^\circ C$) (material temperature on the Earth). The error, for the radiant energy, due to the linear approximation, is about 10% for $T = 323K$ but is still acceptable. The linear approximation can not be used when the range of temperature is too high because the error is too high for the radiant energy. For example, on the planet Mars at Viking landing site, soil temperatures are between about $150K$ and about $300K$ [26]. So, the difference of temperature between a mid point of the range (taken as the point for linearizing the emitted radiance) and the highest or lowest temperature is about $75K$. This difference leads to error higher than 25% for the emitted radiance which is unacceptable for calculating material temperatures on Mars. In that case, we would need to use numerical method [23, 44].⁴

The resolution of the previous system of equations for Earth conditions leads to the expression of the temperature as a function of $t, I, \omega, G_0, \delta, L, \epsilon_s, \epsilon_a, \rho, \tau, T_a$ and V_a . The details of the temperature calculations are presented in Appendix A. In fact, the previous parameters are present in Equation 3.27 via other parameters ($G'_0, \lambda, \mu, \nu, p, q, \xi, u, r, \theta$ and θ_n) that have no obvious

⁴Jaeger [23] used the Schmidt method that is well adapted to the problem of non-linearity of the differential equation.

meaning but allow us to simplify the expression of the temperature. The temperature can then be written:

$$\begin{aligned}
T(\xi, t) = & \frac{\mu}{\nu} + \frac{G'_0}{\nu\pi} \left\{ u \cos^{-1}(-u/r) + r \sqrt{1 - (u/r)^2} \right\} + \\
& + p \frac{\sin(\omega t - \xi - \theta)}{\sqrt{1 + 2q + 2q^2}} \exp(-\xi) + \\
& + \frac{G'_0}{\nu\pi} \left\{ u \sqrt{1 - (u/r)^2} - r \cos^{-1}(-u/r) \right\} \frac{\cos(\omega t - \xi - \theta)}{\sqrt{1 + 2q + 2q^2}} \exp(-\xi) + \\
& + \sum_{n=2}^{\infty} \frac{2G'_0}{\nu\pi} \frac{(-1)^n}{1 - n^2} \left\{ \frac{u}{n} \sin \left[n \cos^{-1} \left(\frac{-u}{r} \right) \right] + \right. \\
& \left. + r \sqrt{1 - (u/r)^2} \cos \left[n \cos^{-1} \left(\frac{-u}{r} \right) \right] \right\} \frac{\cos(n\omega t - \xi\sqrt{n} - \theta_n)}{\sqrt{1 + 2qn^{1/2} + 2q^2n}} \exp(-\xi\sqrt{n}) \quad (3.27)
\end{aligned}$$

where:

$$G'_0 = \tau(1 - \rho)G_0 \quad (3.28)$$

$$\lambda = -(\epsilon_a B + h)T_2 \quad (3.29)$$

$$\mu = A [(1 - \rho)\epsilon_a - \epsilon_s] + T_1 [(1 - \rho)\epsilon_a B + h] \quad (3.30)$$

$$\nu = \epsilon_s B + h \quad (3.31)$$

$$p = \lambda/\nu \quad (3.32)$$

$$q = \frac{k}{\nu} \sqrt{\frac{\omega}{2a}} = \sqrt{\frac{\omega}{2}} \frac{I}{\nu} \quad (3.33)$$

$$\xi = x \sqrt{\frac{\omega}{2a}} \quad (3.34)$$

$$u = \sin L \sin \delta \quad (3.35)$$

$$r = \cos L \cos \delta \quad (3.36)$$

$$\theta = \tan^{-1} \left(\frac{q}{1 + q} \right) \quad (3.37)$$

$$\theta_n = \tan^{-1} \left(\frac{qn^{1/2}}{1 + qn^{1/2}} \right) \quad (3.38)$$

Equation 3.27 gives the temperature for any depth x in the body and any time t . Notice that Equation 3.27 can be simplified in the particular case of the equator ($L = 0$), no convection with the atmosphere ($h = 0$) and no radiation from the atmosphere ($G_a = 0$). The expression of the temperature is then the same as the one found in [6].

Thermal imagers can see only the body's surface temperature and not the temperature of its interior. We are therefore interested in understanding the behavior of Equation 3.27 for $x = 0$. The surface temperature $T(0, t)$ is obtained for $\xi = 0$ since x appears in Equation 3.27 via ξ (see Equation 3.34). Then, it comes:

$$\begin{aligned}
T(0, t) = & \frac{\mu}{\nu} + \frac{G'_0}{\nu\pi} \left\{ u \cos^{-1}(-u/r) + r\sqrt{1 - (u/r)^2} \right\} + \\
& + p \frac{\sin(\omega t - \theta)}{\sqrt{1 + 2q + 2q^2}} + \\
& + \frac{G'_0}{\nu\pi} \left\{ u\sqrt{1 - (u/r)^2} - r \cos^{-1}(-u/r) \right\} \frac{\cos(\omega t - \theta)}{\sqrt{1 + 2q + 2q^2}} + \\
& + \sum_{n=2}^{\infty} \frac{2G'_0}{\nu\pi} \frac{(-1)^n}{1 - n^2} \left\{ \frac{u}{n} \sin \left[n \cos^{-1} \left(\frac{-u}{r} \right) \right] + \right. \\
& \left. + r\sqrt{1 - (u/r)^2} \cos \left[n \cos^{-1} \left(\frac{-u}{r} \right) \right] \right\} \frac{\cos(n\omega t - \theta_n)}{\sqrt{1 + 2qn^{1/2} + 2q^2n}} \quad (3.39)
\end{aligned}$$

For the purpose of understanding Equation 3.39, we successively analyze in Section 3.6.1, Section 3.6.2, Section 3.6.3, Section 3.6.4 and Section 3.6.5 the influence of material parameters (thermal inertia, emissivity, reflectivity) and the influence of other parameters such as wind speed and latitude on the surface temperature of body.

3.6.1 Thermal Inertia Influence

The conductivity k , density ρ_m and specific heat c_p of the material do not appear separately in the expression of the temperature but are bound within the same expression called thermal inertia and noted I :

$$I = \sqrt{k\rho_m c_p} \quad (3.40)$$

The thermal inertia I is present in Equation 3.27 via the variable q (see Equation 3.33) that is proportional to I . Equation 3.39 is relatively complicated and does not allow us to figure out simply the influence of the thermal inertia on the temperature. We can rewrite Equation 3.39 as a function of t and I :

$$\begin{aligned}
T(t, I) = & C_0 + \frac{1}{\sqrt{1 + 2a_0 I + 2a_0^2 I^2}} [C_1 \sin(\omega t - \theta) + C_2 \cos(\omega t - \theta)] + \\
& + \sum_{n=2}^{\infty} \frac{C_3(n)}{\sqrt{1 + 2a_0 n^{1/2} I + 2a_0^2 n I^2}} \cos(n\omega t - \theta_n) \quad (3.41)
\end{aligned}$$

where

$$C_0 = \frac{\mu}{\nu} + \frac{G'_0}{\nu\pi} \left\{ u \cos^{-1}(-u/r) + r\sqrt{1 - (u/r)^2} \right\} \quad (3.42)$$

$$C_1 = p \quad (3.43)$$

$$C_2 = \frac{G'_0}{\nu\pi} \left\{ u\sqrt{1 - (u/r)^2} - r \cos^{-1}(-u/r) \right\} \quad (3.44)$$

$$C_3(n) = \frac{2G'_0}{\nu\pi} \frac{(-1)^n}{1 - n^2} \left\{ \frac{u}{n} \sin \left[n \cos^{-1} \left(\frac{-u}{r} \right) \right] + \right. \\ \left. + r\sqrt{1 - (u/r)^2} \cos \left[n \cos^{-1} \left(\frac{-u}{r} \right) \right] \right\} \quad (3.45)$$

$$a_0 = \frac{1}{\nu} \sqrt{\frac{\omega}{2}} \quad (3.46)$$

$$(3.47)$$

Equation 3.41 shows that the amplitude of T decreases with I while its mean value C_0 is independent of I . In order to illustrate Equation 3.27 and to further analyze the influence of the thermal inertia on the temperature, we calculated the temperature as a function of time for the conditions of the experiment described in Section 3.8 (i.e., $\tau = 0.76$, $\epsilon = 0.92$, $\rho = 0.24$, $V_a = 1.9m/s$, $T_a = 294 \pm 7.5K$, $L = 40^\circ$, $\delta = 10^\circ$) and for the different values of thermal inertia from 0 (ideal body which does not conduct heat) to $4500Ws^{1/2}/m^2K$ (some metallic solid for example). The results are presented in Figure 3.6. Large amounts of information can be extracted from this set of curves:

- Each of the curves achieves a maximum and a minimum temperature in the period of one day. The maximum value occurs at about $2pm$ and the minimum at about $5am$. However, maxima and minima are slightly shifted as a function of time from one curve to another. This behavior can be explained by the phase terms θ and θ_n of Equation 3.27 that depend on the thermal inertia; the phase angle θ or θ_n can vary between 0 for $I = 0$ and $\pi/4$ for I infinite.
- The higher the thermal inertia is, the lower the maximum value of the temperature and the higher the minimum value. In other words, as the thermal inertia increases, the rate of temperature increases at a slower rate. By applying Equation 3.27 in the extreme case where the thermal inertia is infinite, we see that surface temperature becomes independent of time and equal to its constant term C_0 .
- Each curve intersects each of the other curves in only two points whose coordinates depend on thermal inertia values. However, the time coordinates of each of these points from one curve to another is relatively confined to a short interval of time not exceeding a few hours. These intersection points are called contrast inversion points because they correspond to a sign change of the difference of temperature between two curves. This has a visual meaning: two thermal images of the same scene, one taken before the inversion, one after the inversion are such that white objects in the first image become dark in the second one and dark objects become white (see Figure 3.13 and Figure 3.17 of Section 3.8).

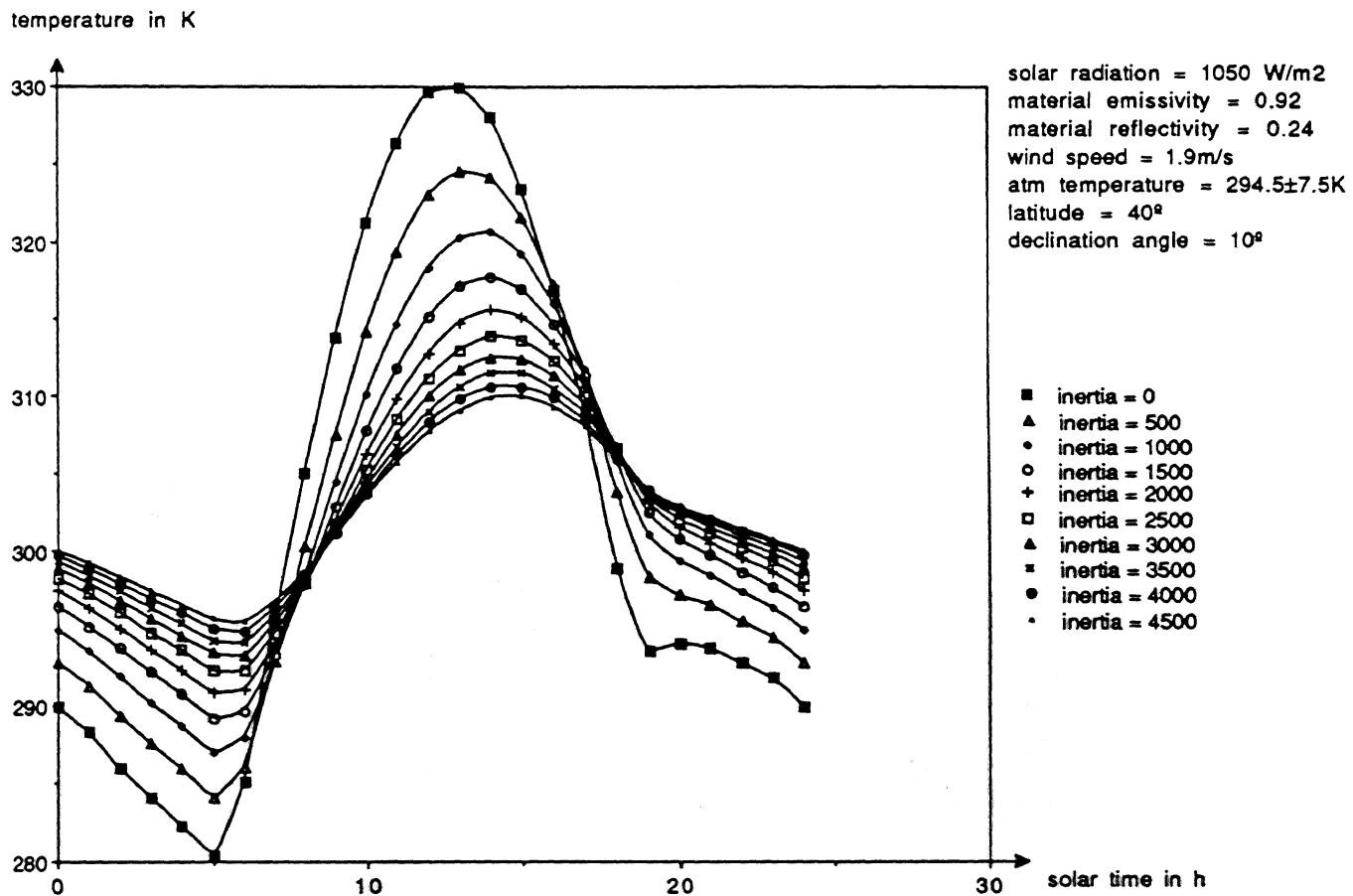


Figure 3.6: Surface temperature of material as a function of time and thermal inertia

3.6.2 Material Emissivity Influence

The radiant energy is proportional to the material emissivity ϵ_s . The lower the emissivity is, the lower the radiant energy leaving the material. Thus, during sunshine, the material retains more heat than when the emissivity is low. Then, the lower the emissivity is, the higher the temperature. Results from the model, presented in Figure 3.7, confirm this qualitative interpretation. We used a

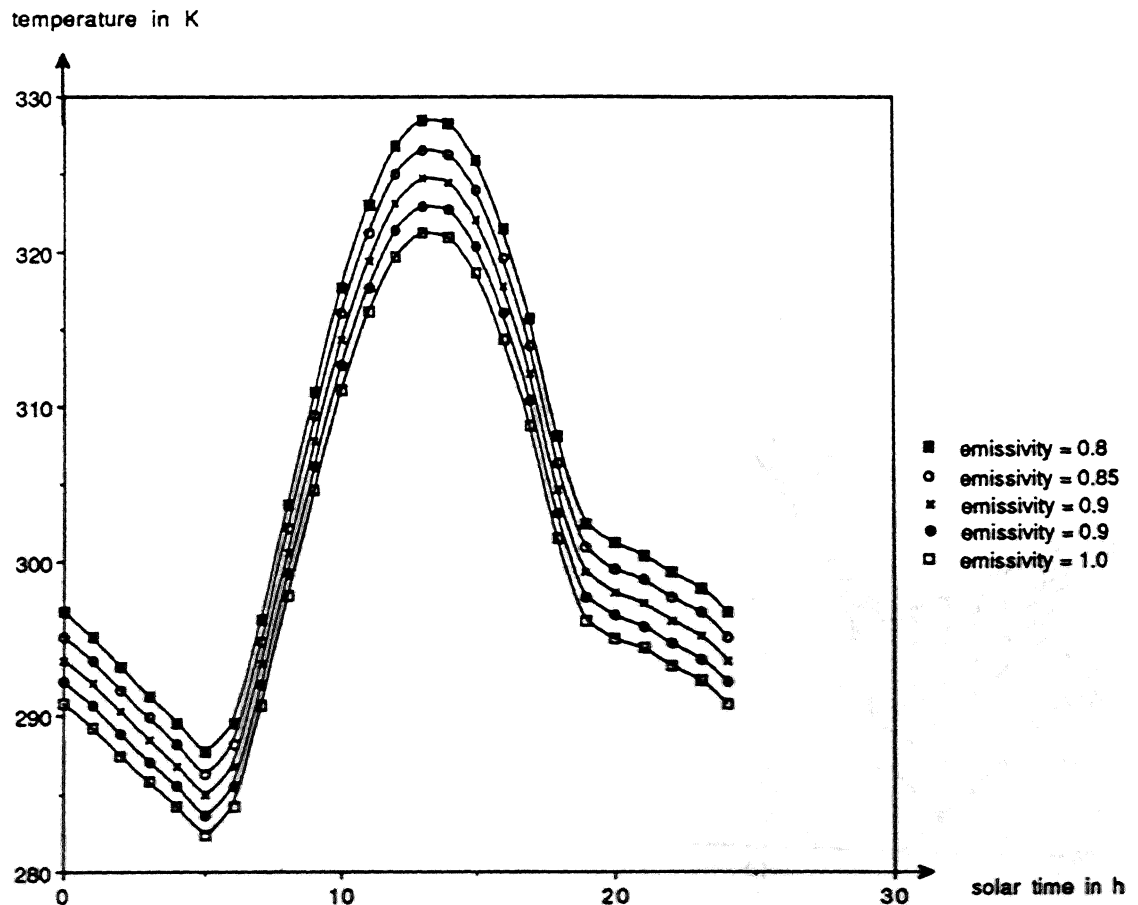


Figure 3.7: Influence of the emissivity on surface temperature

mean value equal to 0.92 for thermal emissivity of sand and rock. In fact, $\epsilon_s = 0.9$ for sand while there is an incertitude ($0.88 \leq \epsilon_s \leq 0.95$) for the rock. In the worst case, $\epsilon_s = 0.88$ instead of 0.92, this gives rise to an error of a few degrees (2 or 3K) for the rock temperature.

To analyze the influence of the emissivity, reflectivity, wind speed and latitude we will set the thermal inertia to a typical value, say $500 \text{Ws}^{1/2}/\text{m}^2\text{K}$, that corresponds to sand and we calculate the

temperature as a function of time by using Equation 3.39 for the experimental conditions presented in Section 3.8.

3.6.3 Material Reflectivity Influence

The reflective energy is proportional to the surface reflectivity ρ . The higher ρ is, the higher the reflective energy and the lower the energy capable of raising material temperatures. So, during sunshine, high reflectivity means lower surface temperature. Results about reflectivity influence are presented in Figure 3.8 for values between 0 and 0.3. Since the material does not receive any radiation during the night, notice that the influence of ρ is less during the night than during sunshine. We set the reflectivity value to 0.24 which is a good approximation for sand and rock.

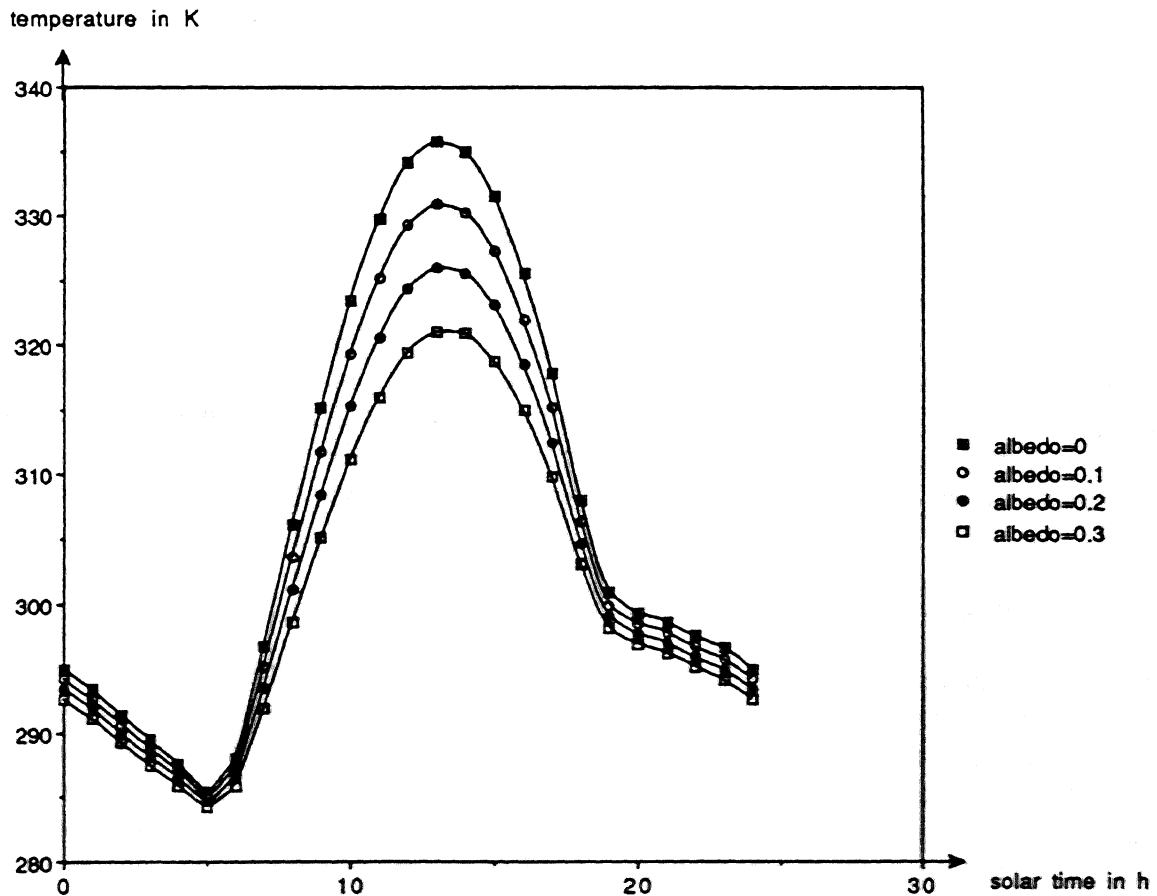


Figure 3.8: Influence of the reflectivity on surface temperature

3.6.4 Wind Speed Influence

The results of wind speed's influence is presented as a set of curves (see Figure 3.9) for different values of wind speed varying from 0 to 20m/s. The higher the wind speed is, the lower the temperature, as intuitively expected. This is true during sunshine but, surprisingly, this is not true during the night. In fact, we saw in Section 3.5 that the wind speed V_a is present in the expression of the convective radiation E_{cv} such that $E_{cv} = (4 + 3.8V_a^{0.8})(T - T_a)$ where T is the surface temperature of the body and T_a is the atmosphere temperature. During the night, atmospheric temperature and the temperature of a body are almost the same; therefore body temperature via E_{cv} is little dependent on V_a . During sunshine, the temperature is highly dependent on wind speed (see Figure 3.9), particularly for low values of wind speed. As an example, the variation of the maximum temperature for $V_a = 0$ and $V_a = 2m/s$ is about 15°C. Unfortunately, this strong dependence argues in favor of the difficulty of calculating the temperature values without precise wind speed measurements.⁵

3.6.5 Latitude Influence

The temperature variation as a function of time accross different latitudes shows the strong dependence of temperature on the latitude (see Figure 3.10). As expected, the closer is an object to the poles, the lower the temperature. Since the equatorial plane is inclined on the elliptical plane, (declination angle $\neq 0$ at the time of the experiment), temperatures for the same latitude with one being positive, the other one negative, are not the same. The maximum of the temperature as a function of time is strongly dependent on the latitude (330K at 0° latitude and 305K at -60°). However, regardless of what the latitude is, the maximum temperature always occurs at about 1am. This analysis shows the importance to take into account the latitude parameter in the model to obtain accurate temperature values. In particular, comparison on the quantitative point of view, between theory and experiment could not be performed in Section 3.8 without this parameter.

3.7 Calculating Thermal Inertia

Figure 3.11 presents a schematic representation calculating the thermal inertia for different input and output parameters of the model. As we said at the beginning of this chapter three physical characteristics of the material are involved in our model: thermal inertia, reflectivity and emissivity. At that point in the development of our model, we meet a substantial difficulty: how can we find the nature of the material with only one equation (Equation 3.27) and three unknown characteristics for the material? To resolve this difficulty we need to add more constraints to our model. Fortunately, we can reduce the number of unknown material characteristics to one: thermal inertia.

⁵For simplicity, we assumed that wind speed is constant over the day, equal to its mean value. For example for the experiment presented in Section 3.8, wind speed fluctuated between 0m/s and 12m/s.

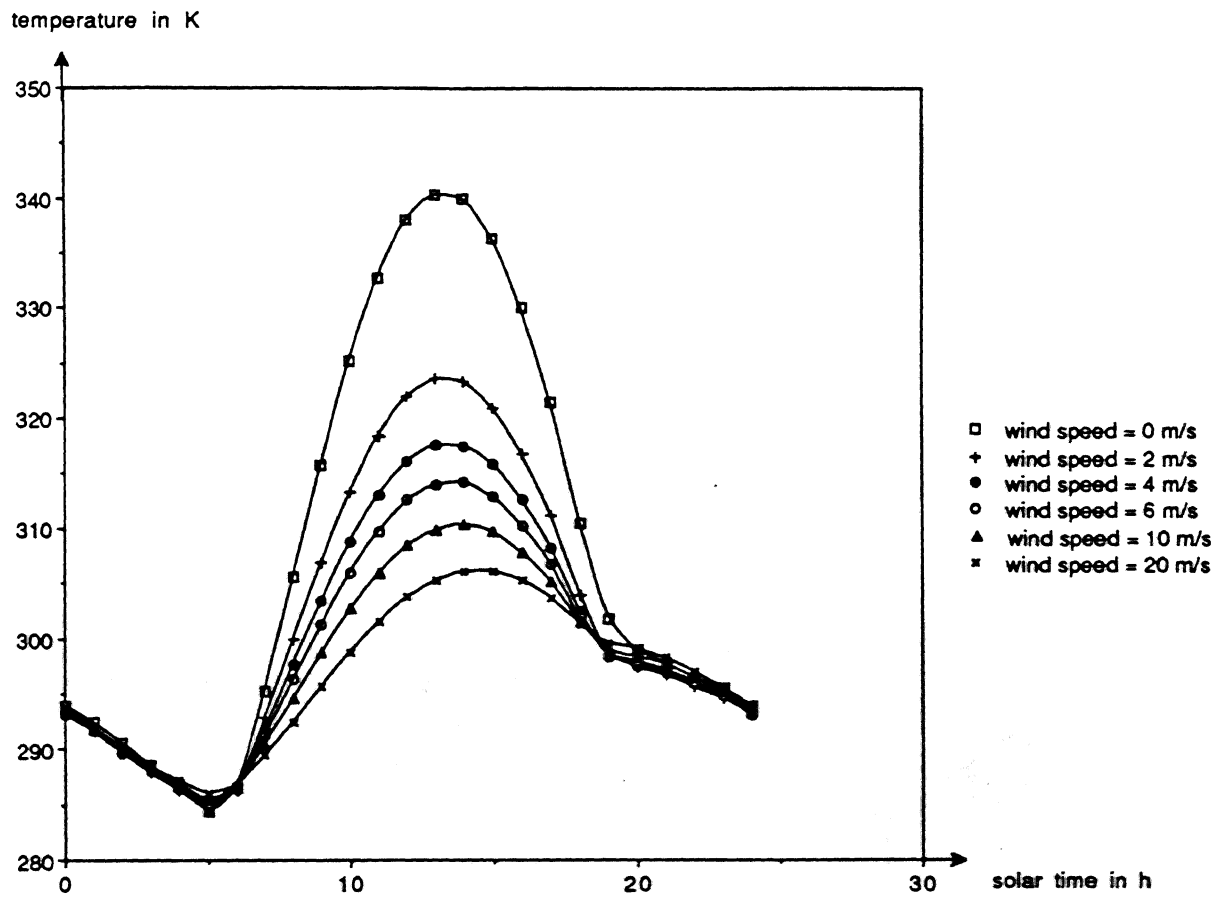


Figure 3.9: Influence of the wind speed on surface temperature

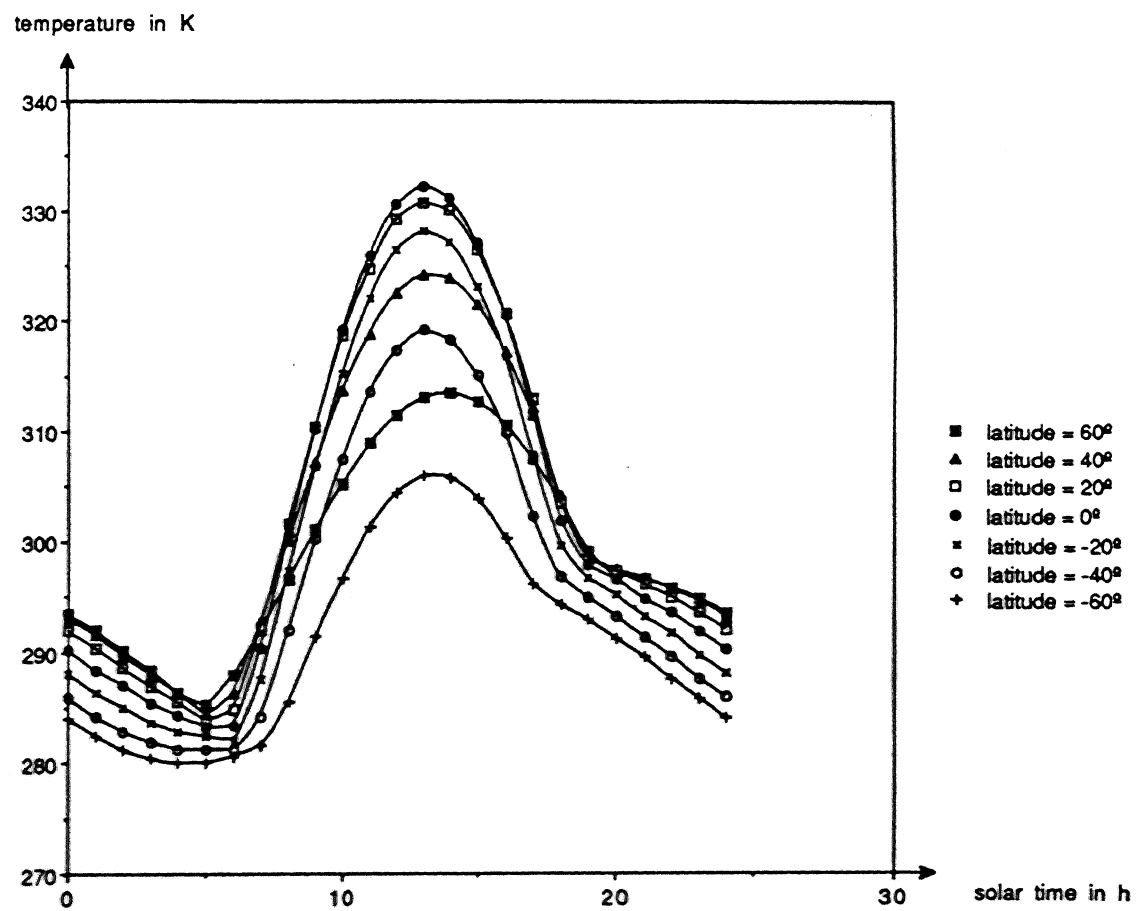


Figure 3.10: Influence of the latitude on surface temperature

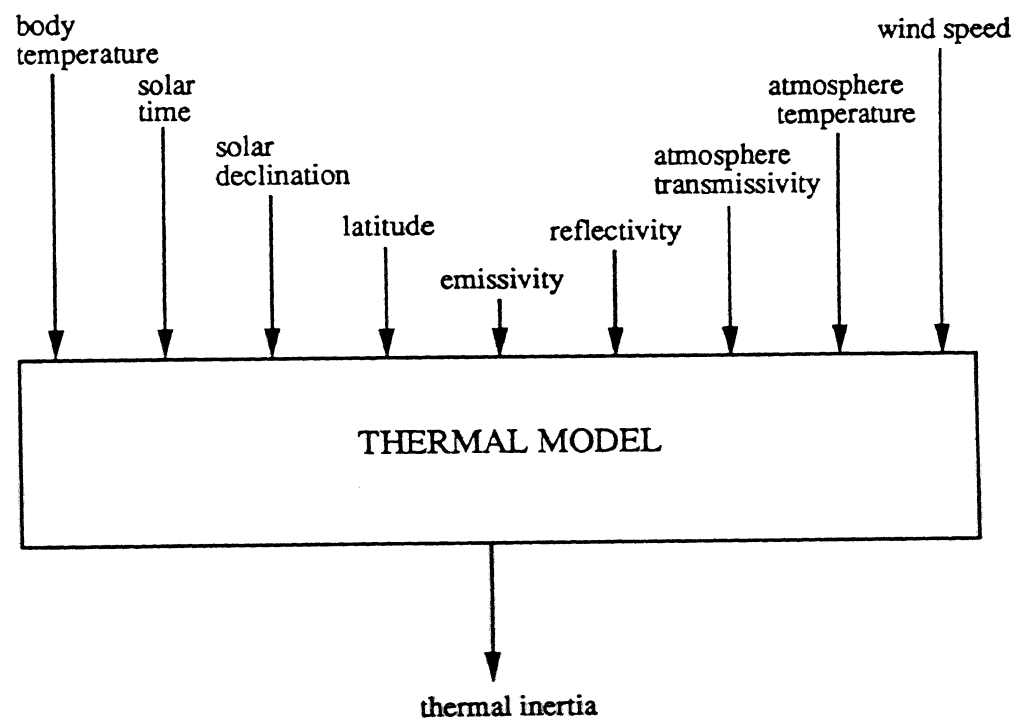


Figure 3.11: Thermal inertia as a function of input parameters

The emissivity of surfaces commonly encountered in natural environment have values close to 0.9 especially for sand and rock [11, 35, 51]. Moreover, we have seen in Section 3.6.2 that a small error in emissivity generates a small error in temperature. Therefore, we constrain our problem by setting the emissivity to a mean value 0.92. We registered experimental images after setting up the camera with this value and we set the emissivity in Equation 3.39 to 0.92 for rock and sand. The reflectivity can vary from one material to another. However, the reflectivity for sand and rock is almost the same and is approximated by the value 0.24 [11, 51]. This parameter was initialized to 0.24 in Equation 3.39. Even if this parameter varies from one material to another, we can measure it using several different techniques such as a visible camera or a laser range finder (see Section 5.4 for more details).

Although thermal inertia is now the only unknown, it can not be directly derived from Equation 3.39 because the temperature expression is too complicated. In Section 3.8.2, thermal inertia values will be calculated for every pixel in the image by using approximation methods such as the Newton's method [5].

3.8 Experiments

In this section, we first present results of the experimentation that we have conducted in an outdoor scene. The experiment consists of measuring temperature of sand and rock. Second, we interpret these results and compare them with theoretical data provided by the model. Third, we calculate the thermal inertia of sand and rock from experimental data, and compare them with values from table of physical constants.

3.8.1 Acquiring Data

We built a horizontal and flat $9m^2$ sandbox, $0.6m$ in depth in Pittsburgh ($L = 40^\circ$, $Lo = 80^\circ$) to demonstrate our model. On this sandbox, we placed a big rock about $0.8m$ long, $0.7m$ wide and $0.35m$ high (see Figure 3.12). For sand, the assumptions of the model, such as dimensions of the sandbox, flatness and horizontality were well respected. However, the dimensions needed for the rock are less than those dimensions needed for the model. During the course of one day, we acquired thermal images of this scene by placing an infrared thermal camera at about $4m$ from the sandbox. The set-up used an Inframetrics camera, model 600 whose resolution is 256×200 pixels and field of view $20^\circ H \times 15^\circ V$. This camera uses a detector HgCdTe cooled by liquid nitrogen and detects radiation in the $8 - 12\mu m$ band (see Section 2.2.1). Thermal images of the scene taken during the day and the night are presented in Figure 3.13, Figure 3.14, Figure 3.15, Figure 3.16, Figure 3.17 and Figure 3.18. The experiment was performed on August 22th 1989 when the solar declination⁶ δ is about 10° .

⁶The solar declination δ was obtained by applying the equation $\sin \delta = 0.39795 \cos[0.98563(N - 173)]$ where $N = 238$ is the N^{th} day of the year [52]. This equation is only accurate within 1° .



Figure 3.12: Sandbox and big rock at the top

Thermal cameras deliver radiosity image (i.e., the intensity level for every pixel is proportional to the radiosity noted E). The temperature T for every pixel can be calculated by using the relation (see Equation 2.7) that relates radiosity and temperature in the $8 - 12\mu m$ band:

$$E = \epsilon \sigma T^4$$

The emissivity ϵ of the bodies was set up to the value 0.92 because as we have already seen it in Section 3.7, 0.92 is a good approximation of sandstone rock emissivity and sand emissivity at ambient temperature. The cursor function of the camera allowed us to get an immediate value of the temperature for every pixel pointed with the cursor (see Figure 3.16). The sensitivity of the measurements is equal to $0.1^\circ C$. Every hour, we measured both the sand and rock temperatures in three points for each. It is possible to use different temperature ranges 5, 10, 20, 50, 100, $200^\circ C$ as a function of the temperature range of the image. During the night, we used the $10^\circ C$ temperature range that corresponded the best to temperature difference between the coldest and warmest points in the scene. During sunshine, we used both the $20^\circ C$ and $50^\circ C$.



Figure 3.13: Thermal image of the sandbox at night (10:38pm)



Figure 3.14: Thermal image of the sandbox at night (3:36am)



Figure 3.15: Thermal image of the sandbox at sunrise, close to the contrast inversion (8:16am)



Figure 3.16: Thermal image of the sandbox during sunshine (10:21am)

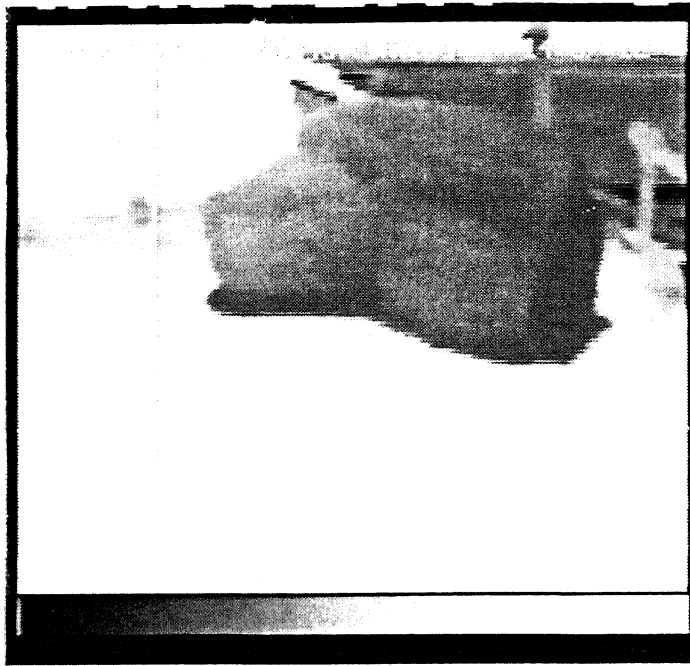


Figure 3.17: Thermal image of the sandbox during sunshine (2:37pm)

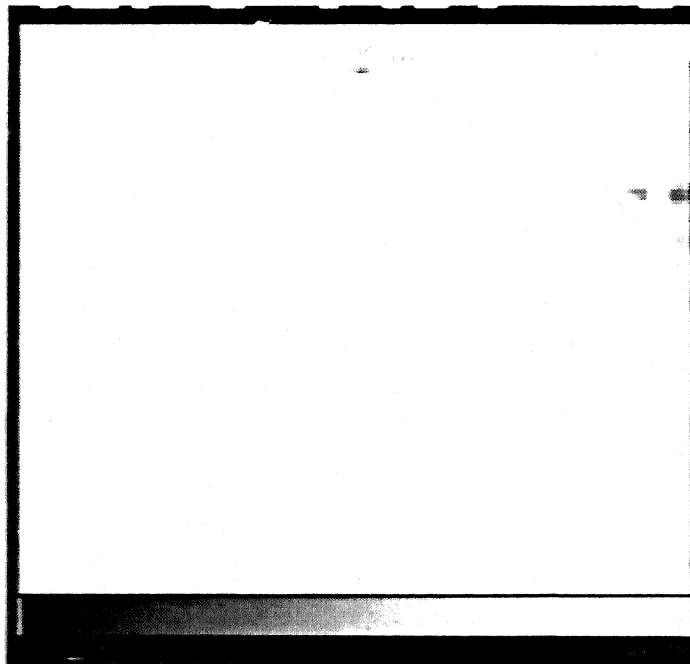


Figure 3.18: Thermal image of the sandbox at sunset, close to the contrast inversion (6:09pm)

Although convenient, the crossbars in the above image restricts us to determining the temperature of only a few points. To obtain the temperature for every pixel, we needed to determine the relation between radiosity (pixel information) and temperature. Instead of using Equation 3.19 which is cumbersome to use, we calibrated the camera as indicated in [37]. The procedure first consists on setting a temperature range (-10°C to 70°C) and then choosing a small range temperature (10°C). Then, one notices the correspondence between intensity level value (or gray level) and the range's minimum as indicated by the camera's computer. By repeating this procedure every 10°C we obtained a table that relates infrared radiosity to temperature. This procedure allows us to convert from gray scale to temperature. Figure 3.19 shows the relation between gray level and temperature. The curve radiation (or gray level), temperature is approximated by a polynomial of order 3 that best

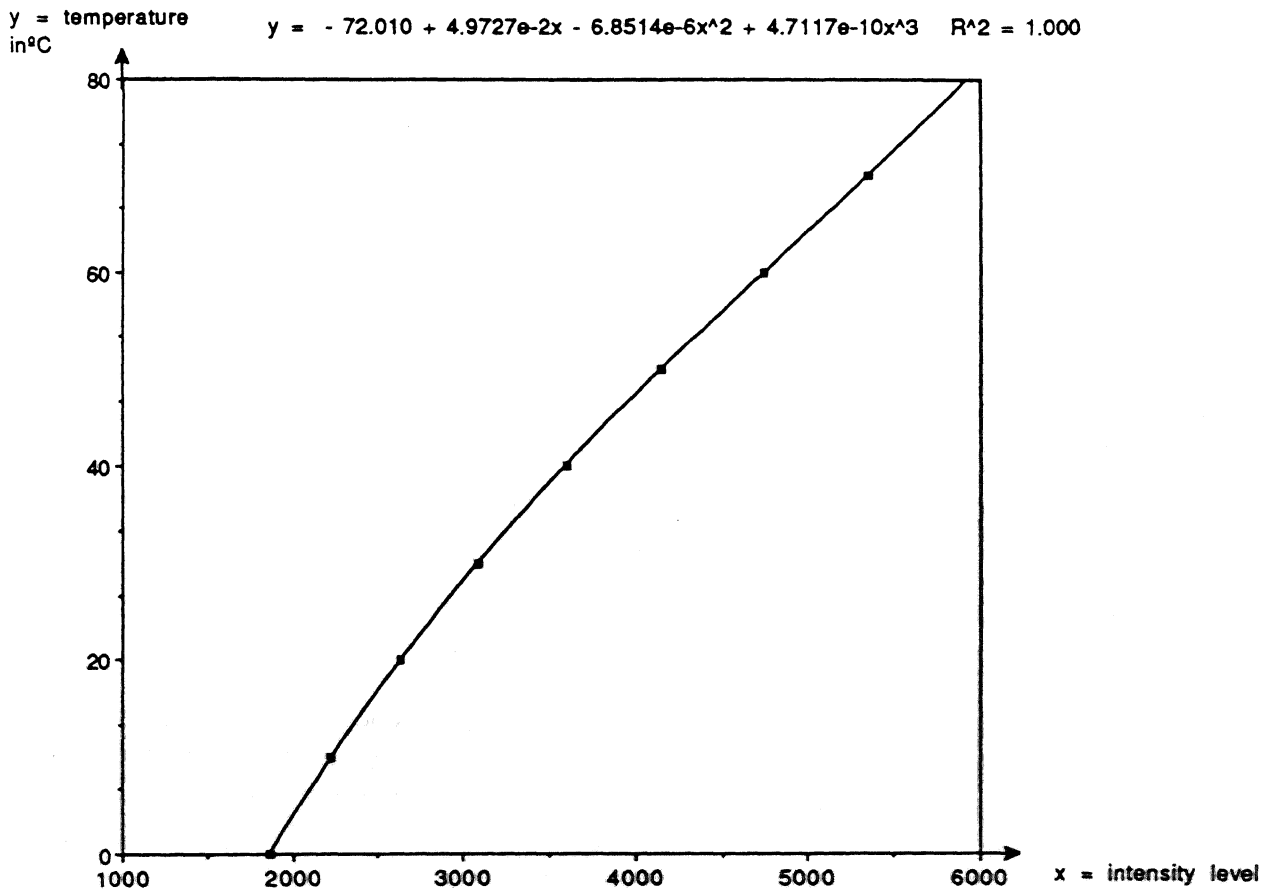


Figure 3.19: Calibration curve of the thermal camera

fits the data.

	$\rho_m(\text{kg/m}^3)$	$c_p(\text{J/kgK})$	$k(\text{W/mK})$	ϵ_s	ρ
sand	1550	800	0.3	0.90	≈ 0.24
sandstone	2560	740	2.8	0.88 to 0.95	≈ 0.24

Table 3.1: Sand and rock characteristics

For this experiment, we used natural sand from Ohio river and sandstone rock. The physical characteristics of the two materials used in this model are the specific gravity, thermal conductivity, specific heat, emissivity, and reflectivity. All of these characteristics, except for the density,⁷ were approached by using tables of physical constants [11, 17, 51]. Values are presented in Table 3.1.

Hourly temperature of the atmosphere and wind speed were delivered by the meteorological station of Pittsburgh. The daily atmospheric temperature during the day can be accurately approximated by the following function of time $T_1 - T_2 \sin(\omega t)$ where $T_1 = 294.5^\circ\text{C}$ and $T_2 = 7.5^\circ\text{C}$. During the experiment, the weather was clear and sunny and the sun was not masked by any clouds.

3.8.2 Interpreting Data

Experimental results are presented in Figure 3.20. The two curves represent the temperatures of sand and rock as a function of time. For both of these materials, the figure shows three main domains.

- Between about 8pm and 7am (night period) the temperature decreases about 12°C for both materials.
- Between about 7am and 2pm (sunshine) the temperature increases rapidly from 10°C to 50°C for sand and from 12°C to 36°C for rock.
- Between about 2pm and 8pm (sunshine), the temperature decreases (less rapidly than it increases) from 50°C to 22°C for sand and 36°C to 25°C for rock.

We can explain the results by using two complementary approaches. The first approach is purely qualitative and requires only elementary knowledge about the physics of heat transfer. The second approach is more quantitative and uses the results of our model presented in the previous chapter.

Let us begin with the **first approach**. The absence of heat source during the night leads to the decrease of the temperature since bodies restitute the energy collected during sunshine. At sunrise, the sun heats sand and rock and the temperature rapidly increases for both of the materials. The heat coming from the sun increases before the zenith and decreases after the zenith. Then, the temperature tends to behave the same. During sunshine, the sand's higher temperature is due to

⁷The density was measured experimentally for both of the materials. The measured values are close to physical values extracted from tables of constants.

sand's conducting heat inside the material less easily than rock's conducting. During the night, sand does not retain the heat as well as the rock does because more concentrated at its surface than the rock's heat. Therefore, the minimum of temperature for sand is lower than for rock. From this, it comes that the two curves of temperature must have two intersection points, one at about sunrise and the other at about sunset. The sign of the difference of temperature changes as the material's heat value crosses these two points. Since thermal images show cold pixels as being darker than warm ones, the sand appears to be whiter than rock during the night and darker than the rock during the day. This explains the name given to these two points: contrast inversion points.

The **second approach** uses the thermal model. The comparison between theory and experiment can be done by estimating the thermal inertia and then doing a point by point comparison between the experimental curve and the theoretical curve corresponding to this thermal inertia. We can not directly compare the experimental results with the results from the model since the reference of time is not the same. The time recorded during the experiment is the local standard time given by the watch while the theoretical model uses solar time. In order to compare results between theory and experiment, we must use a common time reference.

We will use solar time noted ST that is related to local standard time LST [28] by the following equation:

$$ST = LST - EoT - LA$$

where:

- EoT is called equation of time and is due to the following phenomena: because of the Earth's forward movement in its orbit during the solar day, the time required for one full rotation of the Earth is less than a solar day by about $4min$.

$$EoT = 0.1236 \sin x - 0.0043 \cos x + 0.1538 \sin 2x + 0.0608 \cos 2x$$

where

$$x = 360(N - 1)/365.242$$

N is the N^{th} day of the year. $N = 238$ (26th of August) for our experiment.

- LA is the adjustment for longitude expressed in hours. It is due to the fact that the local time is the same in Pittsburgh (longitude= 80°) and for example Washington (longitude= 77°) or for every location between 75° and 90° in longitude. Since the longitude of the standard meridian for the local time zone is 75° , the correction LA is:

$$LA = \frac{1}{\omega} [Lo - Lo(\text{local time meridian})] \quad (3.48)$$

LA is equal to $20min$ and cannot be neglected. This comparison was performed for sand and rock. Thus, about twenty five minutes have to be added to local standard time to obtain solar time.

The results that take into account this correction are shown in Figure 3.20. In the example using sand, theory and experiment agree since the difference of temperature between both is not higher than 4°C between 9am and 7pm (period that corresponds to sunshine). During the night, agreement is not so good and error between theory and experiment can reach 6°C . For rock, all the assumptions required for applying our model were not satisfied. In particular, the assumption of a semi-infinite body is not satisfied since the height of the rock (0.35m) is lower than the 0.9m required by the model and the other dimensions are only twice higher than the height. Comparison therefore shows us, as expected, a bigger error for rock than for sand between theory and experiment. The theoretical temperature for rock is always superior to the experimental one from 4 to 10°C .

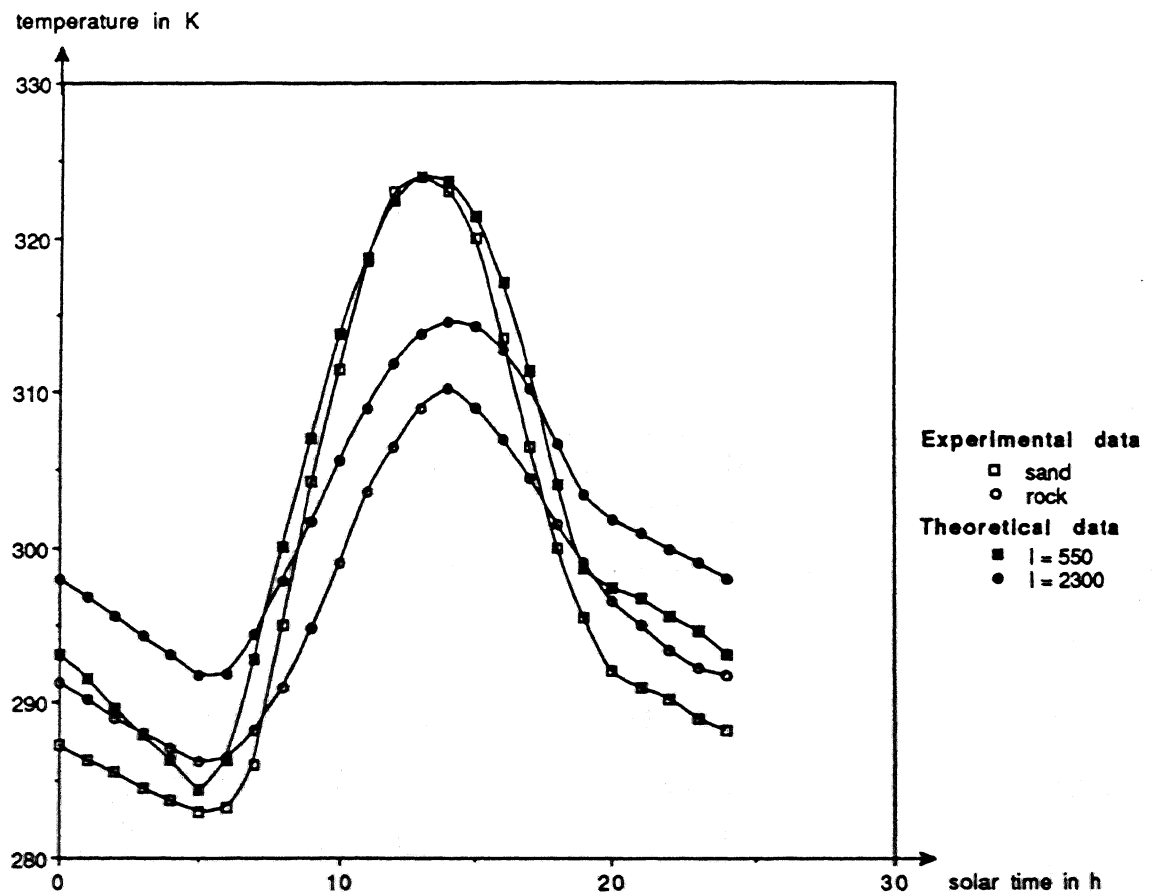


Figure 3.20: Experimental and theoretical temperature for sand and rock

$I (Ws^{1/2}/m^2K)$	rock	sand
data from table	2300	550
data from model 2:37pm	4700	500
data from model 3:36pm	1200	600

Table 3.2: Thermal inertia of sand and rock

3.8.3 Using Data to Calculate Thermal Inertia

We implemented the thermal model algorithm (See Section 3) such that it calculates the thermal inertia for every pixel in the image.

The grey level in the image is the linear representation of the thermal inertia from the minimum value (black) to the maximum value (white). We can notice, that the program requires the following input parameters: pixel temperature, location (latitude and longitude), watch time, wind speed, mean value and amplitude of the atmosphere temperature, day of the year, minimum and maximum of temperature range. Results of the segmentation are presented in Figure 3.21 and Figure 3.22. For sand, the value of thermal inertia indicated in Figure 3.21 and Figure 3.22 is calculated for a pixel located in the middle of the sandbox. For sand, the temperature is almost the same from one point to another (within a few percent of the mean value). Therefore, the thermal inertia is close for every point to the value calculated by the algorithm. For rock, we chose a point located on its top face. The larger diversity in grey level for the rock indicates a higher range of thermal inertia than for sand. If we select another point on the rock then, the thermal inertia can be very different. This shows the difficulty to calculate accurate value of thermal inertia for the rock. Indeed, higher is the thermal inertia, more sensitive the thermal inertia calculation is to temperature fluctuations (see Figure 3.6). In order to have a better idea of the rock thermal inertia, we segment rock from sand by using a computer vision algorithm (see Chapter 4). Then, we can calculate a mean value of the temperature for the region that corresponds to rock in the segmented image. Finally, we can calculate the thermal inertia corresponding to that temperature.

Comparison between theory and experiment is presented table 3.2,

3.9 Limitations of the Model

The model suffers from several limitations that do not allow us to obtain accurate values of the temperature and, consequently, thermal inertia.

- The model of the shape of the body is very simple. The assumption of a semi-infinite body requires that the dimensions of the body are sufficiently large. We can derive from Equation 3.27 that the daily temperature variations is a function of ξ (where $\xi = x\sqrt{\frac{\omega}{2a}}$ is

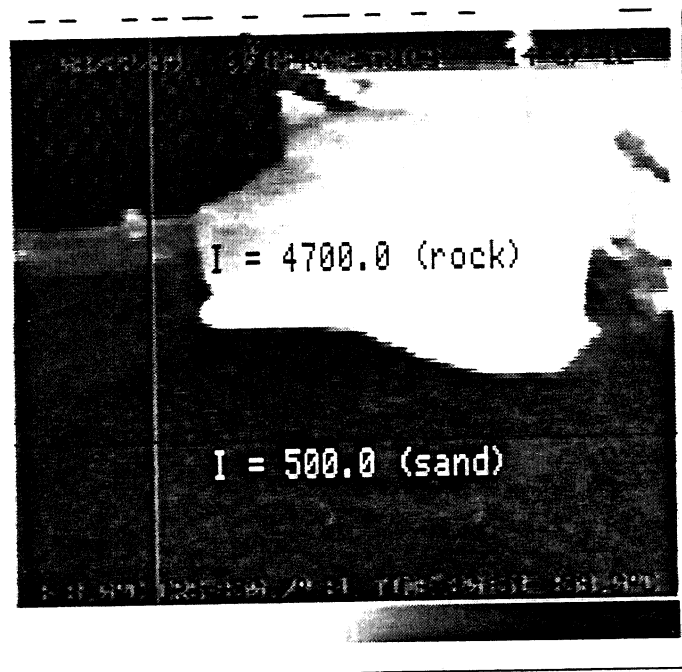


Figure 3.21: Image of thermal inertia during sunshine (2:37pm)



Figure 3.22: Image of thermal inertia at night (3:36am)

proportional to the depth x in the material as expressed by Equation 3.34) and approximately vanishes according to an exponential law:

$$\frac{T_M(x) - C_0}{T_M(0) - C_0} \approx \exp(-\xi) \quad (3.49)$$

where $T_M(x)$ represents the function's $T(x, t)$ temperature maximum for the depth x and C_0 is the constant term in Equation 3.27. For sand, the temperature is attenuated more than 99% for $x \geq 0.4m$. Consequently, the depth of the material has to be at least equal to $0.4m$ to consider the body as being semi-infinite. The other dimensions need to be greater than its depth in order to neglect heat fluxes emanating from the body's lateral faces. For the sandstone rock used in the experiment, the depth of the material should be greater than $0.9m$.

- To establish Equation 3.17 (heat conduction equation), we assumed that the **conductivity** does not depend on x . However, if the soil is not homogeneous (mixed composition of rock and sand for example), the conductivity can be a function of x [48]. In that case, accurate values of the temperature can be found only if this dependence is known.
- The influence of the **emissivity** and the **reflectivity** has been discussed in Section 3.7 and Section 3.8. In our model, we have estimated these parameters by using a priori knowledge of the types of objects in the scene. Although natural objects have an emissivity close to 0.9 and a reflectivity close to 0.24, we commit an error in assigning these values. Indeed, it would be more precise to measure these parameters. For the emissivity, there is no simple means. For the reflectivity, it is possible to use the reflectivity image delivered by a laser range finder (see Section 5.4).

Although body characteristics limit the application of the model, there are other limitations due to the meteorological conditions such as wind and solar radiation:

- **Wind influence** is also another limitation for the model since the temperature depends on wind speed that can change with time and location. Figure 3.9 shows the important contribution of the wind speed on the temperature's final value. Therefore, it is not satisfactory to approximate the wind speed by the mean value during one entire day (see Section 3.5). To be accurate, the model should take into account the variation in wind speed by, for example measuring its instantaneous value with an aerologic central and using a numerical model to calculate the temperature.
- The **solar radiation** falling on the scene was theoretically approached by considering a clear sky. In the general case, clouds can mask the sun from time to time and change the amount of radiation reaching the objects. Due to the presence of clouds, sun radiation can then be scattered by a factor of 80%. Then, the model is not appropriate for determining accurate temperature values. Moreover, the solar intensity reaching the Earth is theoretically

approached in Section 3.3 where it is assumed that the transmissivity of the atmosphere can be modeled by a constant transmission factor. Indeed, the transmissivity of the atmosphere depends on several factors such as the elevation angle of the sun and the composition of the atmosphere [52].

- **Shadows** are due to the presence of obstacles on the way of solar beams. During the experiment (see Section 3.8), the rock projected its shadow on the sand area (see Figure 3.18). The difference of temperature between the shady area and the sunny one on sand can reach more than 5°C . Differentiating rock from shadow is therefore delicate.

All the previous limitations of the model lead to approximate quantitative values for the temperature and the thermal inertia. Since quantitative results are not always reliable, we need to answer the question: How to Use the Model?

3.10 How to Use the Model?

The quantitative values of thermal inertia calculated by using the thermal model are not accurate enough to know at any time of the day that we used coarse sand and a sandstone rock. This is due to the limitations of the model presented in the previous section. However, the model indicates at any time of the day and night that the thermal inertia for sand area is lower than for rock area as it is in reality. Even if quantitative data of thermal inertia are not always accurate enough to determine the nature of the material, the model can reliably classify the materials by increasing value of thermal inertia.

Indeed, if we take two materials whose thermal inertia are I_1 and I_2 such that $I_1 < I_2$, then, the results of the model (see Section 3.7) show that:

- $T(I_1) < T(I_2)$, during the night
- $T(I_1) > T(I_2)$, during sunshine

with a short shift in time depending on the material.

This is true for the particular values of emissivity, reflectivity, latitude and wind speed of our experiment (see Figure 3.6). But, simulations in a broad class of conditions (different values of these parameters) have shown that the temperature behavior as a function of the thermal inertia is still the same as the one described before. Indeed, for other values of emissivity, reflectivity, latitude and wind speed than those of the experiment, we also obtain a graph similar to that in Figure 3.6 with two contrast inversion points, one at about sunrise the other one at about sunset. Figure 3.23 and Figure 3.24 represent two particular cases of these simulations performed at the equator (instead of Pittsburgh latitude) and for two different conditions of wind ($V_a = 0$ and $V_a = 10\text{m/s}$). This result is important because it means that the thermal behavior of materials described above is a

constant behavior. Then, it can be used to discriminate materials of different thermal inertia. On the qualitative point of view, our model is more reliable than on the quantitative one.

We think that the qualitative thermal behavior of materials described before is still the same as the one described before even if the different assumptions of our model are not respected (small dimensions of the object instead of semi-infinite body, cloudy sky instead of clear sky, ...). Results from an experiment performed by a cloudy sky (see Section 4.1) tend to confirm that point. Although the smaller rock does not satisfy the assumption of semi-infinity (see Figure 4.3), its temperature is lower than sand during sunshine as foreseen by the model. Moreover, an image of the sandbox taken at about sunrise showed that the temperature of rock is the same as sand one (as foreseen by the model). Further experiment should however be done to verify the limits of the domain of validity of our model.

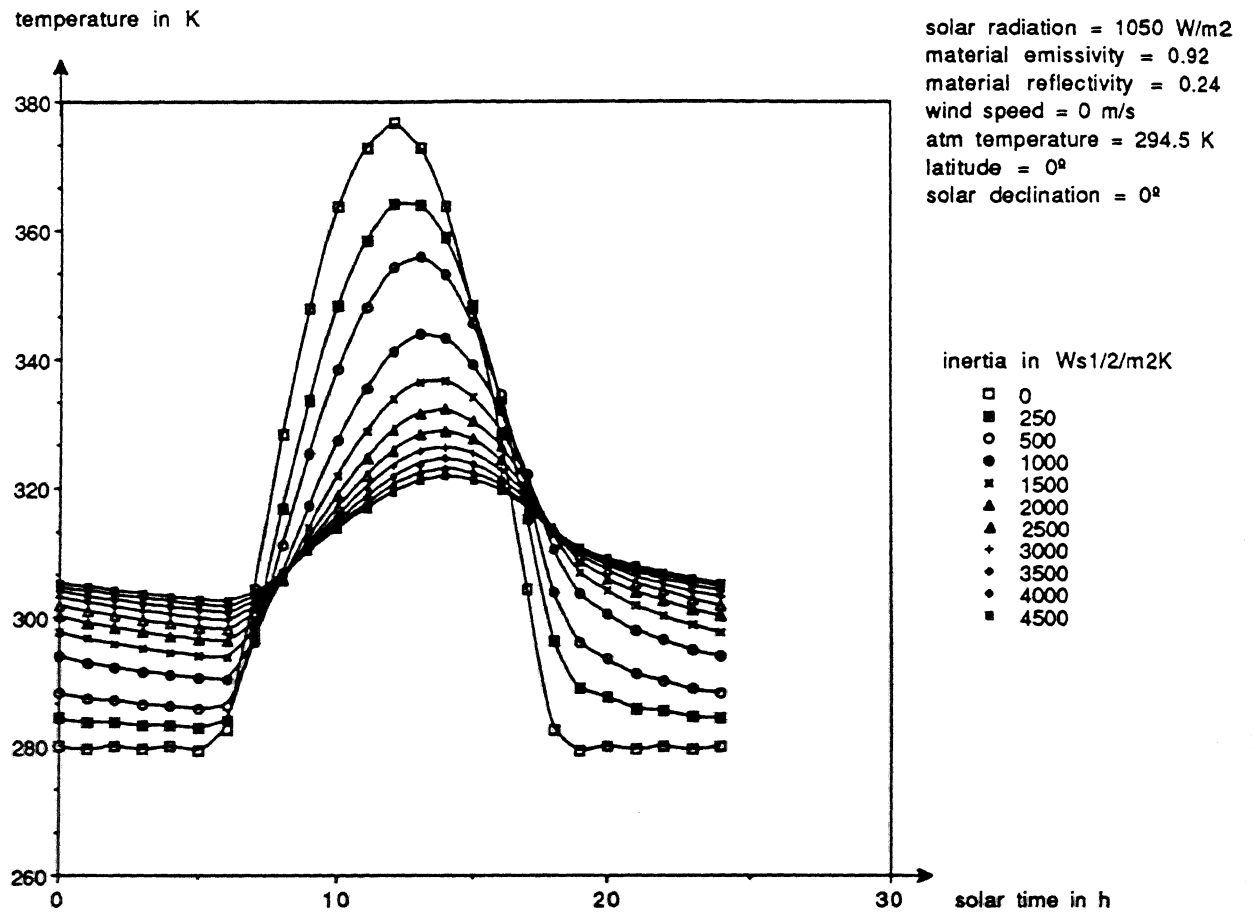


Figure 3.23: Surface temperature of material as a function of time and thermal inertia at the equator, for $V_a = 0 \text{ m/s}$

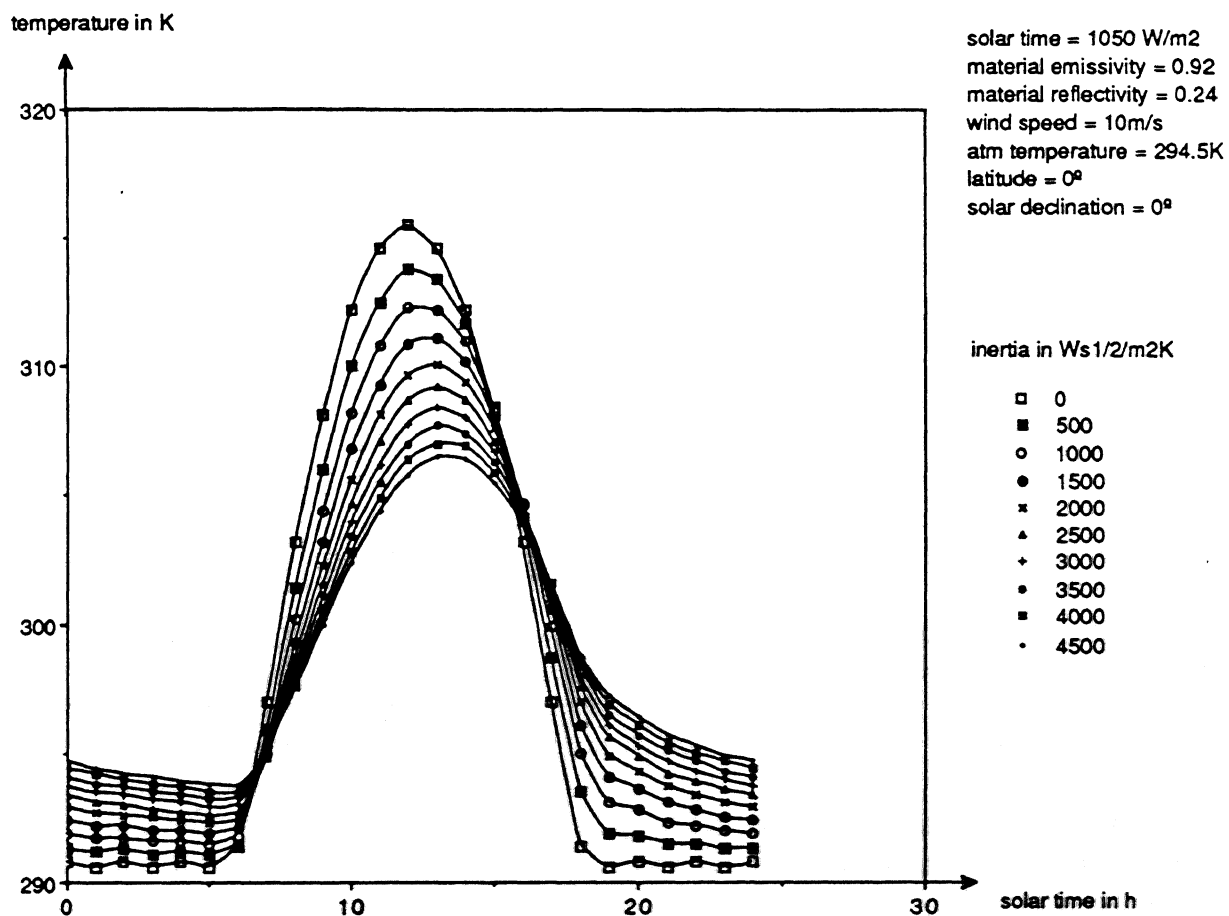


Figure 3.24: Surface temperature of material as a function of time and thermal inertia at the equator, for $V_a = 10 \text{ m/s}$

Chapter 4

Thermal and Range Fusion

The model that we have developed in the previous chapter allows us to understand the qualitative thermal behavior of materials and to recognize them by calculating their thermal inertia. Thermal inertia values are however often unaccurate because we modeled our problem very simply by making, in Section 3.1, restrictive assumptions about the shape of the body (horizontal plane) and about its heat exchanges with the environment (for instance, sun never masked by clouds).

Since segmentation is the starting point in image understanding to recognize objects, we explore in Section 4.1, as a complementary approach to the calculation of thermal inertia, the field of image segmentation applied to thermal images.

Then, we apply through previous work carried out at Carnegie Mellon University, 3D vision techniques for determining the regions and boundaries of objects in outdoor scenes [18, 21, 30]. 3D segmentation can be seen itself as a complementary approach to thermal image segmentation since it provides information about the geometry of the terrain while thermal imaging provides information about the nature of the materials.

Finally, by combining (or fusing) thermal and range information, we show on an example of outdoor scene that it is possible to obtain a better segmentation than by using thermal only, in the case of occluding objects that have the same temperature. In the following, we focus our attention on an outdoor scene composed of sand and rock (see Figure 3.12). The only difference is that we put another smaller rock on the sandbox.

4.1 Thermal Imaging Segmentation

4.1.1 Splitting Method

There are three predominant segmentation techniques in use today: Edge detection, Region growing and Region splitting. Of these, we have chosen to use Region splitting technique because a powerful algorithm using this technique has been developed at Carnegie Mellon University [43]. This algorithm is known as recursive region segmentation by analysis of histograms. More precisely, we

used Phoenix system that is the last version of region segmentation program using this algorithm [43]. The algorithm consists of splitting the image into portions along sharp intensity boundaries, then recursively splitting each part along intensity boundaries until all parts exhibit uniform intensity. At the beginning of the process, the entire image is taken as the first region. The starting point for splitting the region is the analysis of its histogram.¹ Valleys that correspond to minima of the histogram are detected. They are then used to split the image since they usually separate regions of different intensity level.

This method appears to be well adapted to thermal images since pixels belonging to the same portion of the image usually have similar intensities and their histograms therefore present well defined valleys. In fact, for usual scenes where rocks have rather small dimensions ($\leq 0.9m$) the temperature or the intensity level in the image essentially depends on the type of material and not on the geometry of the objects (case of the rock in Figure 4.2).² This can be explained in terms of heat transfer process. For relatively small objects (dimensions the same or less than the model's theoretical dimensions), the heat is not only diffused in the perpendicular direction of the patch of surface but also in other directions. The temperature at the surface of body tends therefore to be more uniform.

Region growing could also be an interesting technique to investigate since intensity similarity is the basic criteria for segmenting the regions.

4.1.2 Results

We applied Phoenix to two thermal images of the sandbox, one was taken at night (10:38pm) and one during the day (2:37pm). Before applying Phoenix, we reduced the noise³ in the image by applying a 3×3 median filter whose effect is to eliminate the noise without affecting much the boundaries of regions. The principle of the median filter is to replace each gray level in the image by the median value of its neighbors in a 3×3 window. The original thermal images, before applying the median filter, are presented in the upper left corner of Figure 4.1 and Figure 4.2. It was sufficient to limit the recursive process of Phoenix to one iteration because contrast between rock and sand was already good in the original images.⁴

Segmentation results are presented in the lower right corner of Figure 4.1 and Figure 4.2. The upper right corner contains the histogram of the original image and the threshold chosen by Phoenix for splitting the image. The two histograms show two peaks separated by a deep valley where the

¹The histogram represents the number of points in the image for each possible value of gray level (from black to white).

²Too small dimensions of object were a limitation to apply the thermal model. Here, small dimensions are preferred to large one because segmenting algorithms such as Phoenix are looking for regions of the same gray level.

³The noise present in nightly thermal images is like small aberrant points certainly due to the very small range of temperature during the night.

⁴The mean variation in intensity level between rock and sand is more than 35% of sand intensity level whereas the mean variation within sand or within rock is less than 5%.

threshold is chosen. All image points having a gray level below the threshold are classified in the same region. Conversely, all the points having a gray level above the threshold are classified in the second region. In the lower right corner are presented the two uniform regions and their edges. One of the region corresponds to sand and the other one to rock. For Figure 4.1, rock and sand are well segmented. For Figure 4.2, notice that the top most side of the rock is fused with the background because the gray level for the background is almost the same as the rock. In fact, those points are not directly interesting in the context of our problem because they belong to building materials and not to rock or sand. On the lower left corner are presented the edges of the segmented regions superposed to the original image.

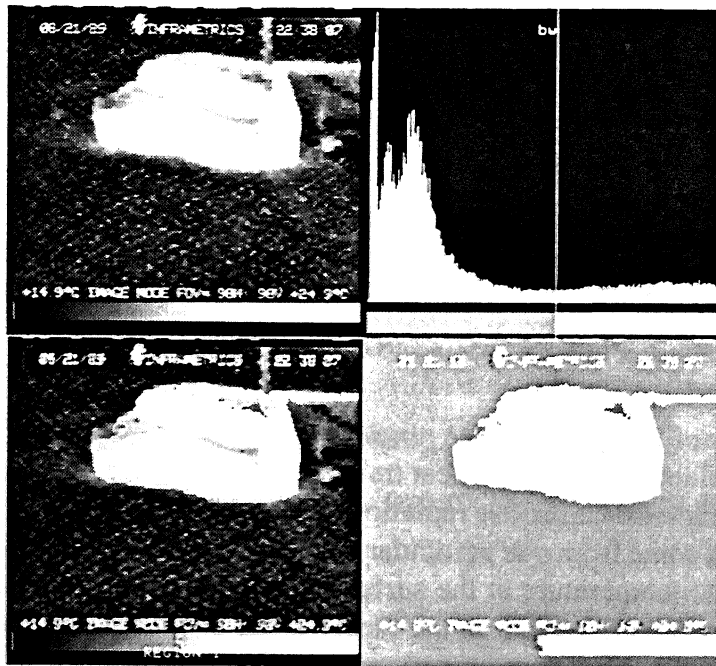


Figure 4.1: Phoenix applied to nightly thermal image (10:38pm)

A few days after the first experiment, we performed a second set of experiment with a thermal camera and a black and white camera. The sky was entirely covered by clouds. The main interest of this experiment is first to apprehend the sensitivity of segmentation techniques to variation of sky conditions (clear or cloudy) and second to compare results of segmentation with well known sensors such as black and white camera.

Let us begin with thermal images. Original thermal image and result of the segmentation are presented in Figure 4.3. The segmentation is fairly good for the small rock and the lower part of the big rock. However, the above part of the big rock is not as well segmented because it is fused with the background that is almost at the same temperature as the rock. Indeed, like in Figure 4.2, the background is neither sand nor rock but building materials that are not interesting for the experiment

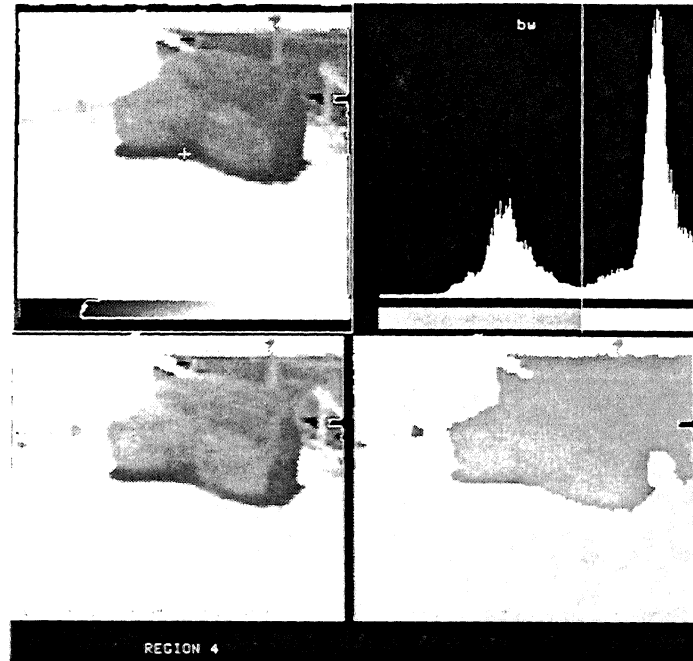


Figure 4.2: Phoenix applied to daily thermal image (2:37pm)

(see the upper left corner of Figure 4.4 to see precisely those materials). The good contrast between sand and rock can be explained in terms of heat transfer process. If the sky is predominately cloudy, then the major source of radiation is diffuse radiation. That is, direct solar radiation is minimal. Since diffuse radiation does not come from one particular direction, the different facets of bodies are heated uniformly. Therefore, the temperature at the surface of the body tends to be uniform. Conversely, if a body is receiving direct solar radiation, the facets of the body that are oriented towards the sun will be preferentially heated. For large objects, surface temperature is very dependent on surface orientation. For small objects like the rocks we are using (i.e., dimensions lower than those required to satisfy model's conditions presented in Section 3.9), the temperature is in fact, not much dependent on surface orientation (see Figure 3.17). The reason why surface temperature is little dependent on surface orientation for small objects, even by clear sky, is that heat interactions from different parts of the body are important. The surface temperature then tends to be more uniform than for bigger rocks.

Application of the Phoenix algorithm to images from a black and white camera are presented in Figure 4.4 and Figure 4.5. Phoenix's segmentation does not differentiate between the rocks and the background as well as it does for thermal images. This is because the reflectivity or the reflected visible energy (what will be recorded by a black and white camera) for sand and rock are almost the same. For the same reason, the result of the segmentation is very sensitive to illumination conditions: applying Phoenix to the same scene with only a few hours difference leads to very different results.

This is illustrated by Figure 4.4 and Figure 4.5. A major advantage of thermal over black and white cameras is of course the possibility to use thermal during the day and the night while black and white is limited to daytime.

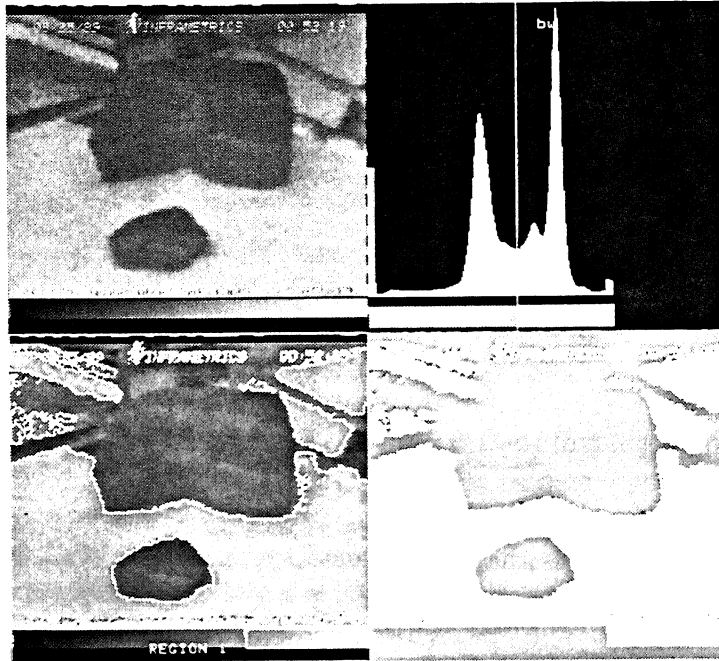


Figure 4.3: Phoenix applied to a thermal image: two rocks one big and one small are in the scene (10:38am)

4.2 Range Segmentation

A geometric representation of the terrain can be constructed by using data from a laser range finder. The laser range finder that we used is developed by the Environmental Research Institute of Michigan and called ERIM [54]. The basic principle of this sensor is to measure the difference in phase between the emitted signal from the sensor and the reflected signal from the scene. A two-mirror scanning system allows the beam to be directed anywhere within a $30^\circ \times 80^\circ$ field of view. The data produced by the ERIM sensor is a 64×256 range image. The range measurement is encoded in 8 bits. The position of any point is given in terms of range D and orientation of the laser beam θ and ϕ .

The cartesian coordinates (x, y, z) of a point can be derived from the spherical coordinates (D, θ, ϕ) by using the following relations:

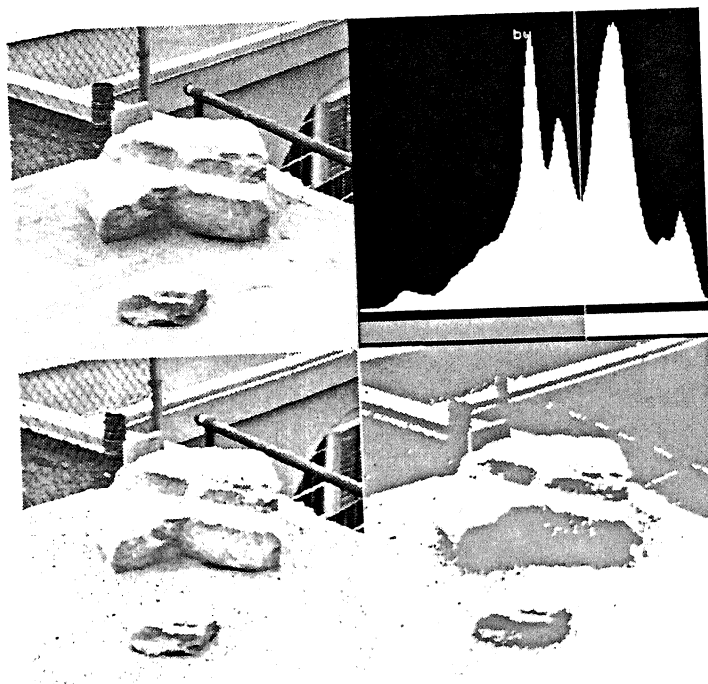


Figure 4.4: Phoenix applied to an image of the sandbox taken by a black and white camera (10:38am)

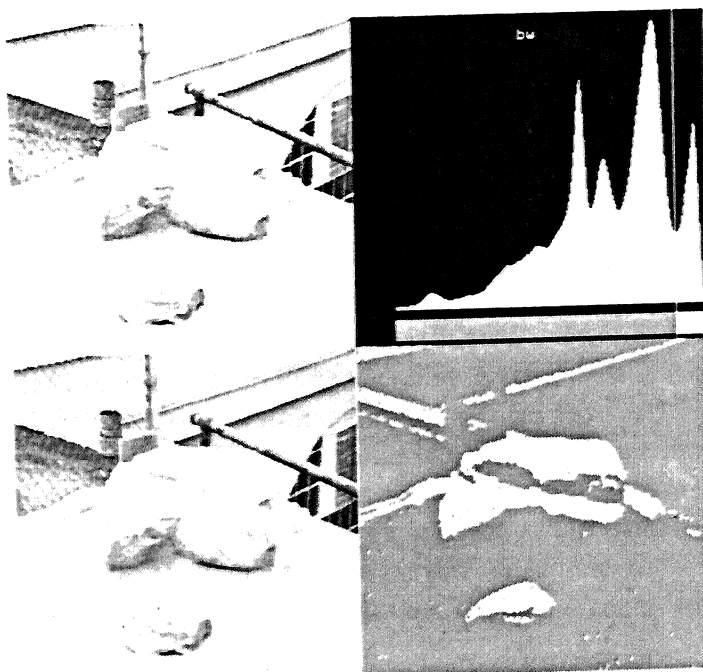


Figure 4.5: Phoenix applied to an image of the sandbox taken by a black and white camera (1:45pm)

$$\begin{cases} x = D \sin \theta \\ y = D \cos \phi \cos \theta \\ z = D \sin \phi \cos \theta \end{cases} \quad (4.1)$$

From this representation, techniques have been developed to find curvatures and 3D edges such as range jumps or surface normals in range images which will allow us to find objects [18]. Techniques to understand surfaces in range images are analyzed and discussed in [4]. We will limit our analysis to the extraction of 3D edges that provide important pieces of information about the shape of the terrain and the presence of objects or obstacles.

4.2.1 Range Jumps and Normal Variation Detection

We computed edges by detecting first, range jumps and second, surface normal variation [18]. The range jump detection could be done directly by thresholding range jump information but unfortunately, this quantity depends on the range and tends to be higher for longer distance than for shorter distance. A better quantity to threshold is the ratio $\Delta D/D$ that less depends on the range D [14]. This approach is well adapted to find edges of objects that lie on a plane. In first approximation, we may consider the outdoor soil as being a planar surface.

The principle of normal variation detection is to approximate locally the surface of the terrain by portions of planes, calculate plane normals $\vec{n} = (n_x, n_y, n_z)$ and their variation. The plane normal variation is estimated by computing the following quantity:

$$\sqrt{(\Delta n_x)^2 + (\Delta n_y)^2 + (\Delta n_z)^2} \quad (4.2)$$

where Δn_x , Δn_y and Δn_z are respectively the squared gradient of n_x , n_y and n_z .

$$\Delta n_x = \sqrt{\left(\frac{\partial n_x}{\partial x}\right)^2 + \left(\frac{\partial n_x}{\partial y}\right)^2 + \left(\frac{\partial n_x}{\partial z}\right)^2} \quad (4.3)$$

We estimated the partial derivatives by using discrete approximations of the following form:

$$\frac{\partial n_x}{\partial x} \approx \frac{1}{2} [(n_x(i+1)(j+1) - n_x(i)(j+1)) + (n_x(i+1)(j) - n_x(i)(j))] \quad (4.4)$$

where $n_x(i, j)$ represents the projection of the normal along the x axis at the point (i, j) in the range image.

4.2.2 Results

Results of applying range jump detection to range image of the sandbox Figure 4.6 leads to the image presented in Figure 4.7. The edges of the sandbox and the upper frontier of the big rock are clearly

extracted. The upper frontier of the small rock is in part extracted but not so clearly as the big rock because range jumps are of the order of the resolution of the range finder.

In Figure 4.8, we present the projections of the normal vector along the x , y , z axis. Black patches correspond to places where the projection of the normal is equal to zero whereas white patches correspond to places where the normal vector is parallel to the direction of projection.

In Figure 4.9, we present the result of applying the algorithm of normal variation. The algorithm is only applied to points that are not too far from the sensor because we are interested by points belonging to the sandbox.⁵ The lower edge of the big rock at the junction with the sand area is well extracted. Moreover, edges that correspond to variation of surface normal within the big rock are extracted. The lower edge of the small rock is not extracted because the normal variation is too small to be detected.

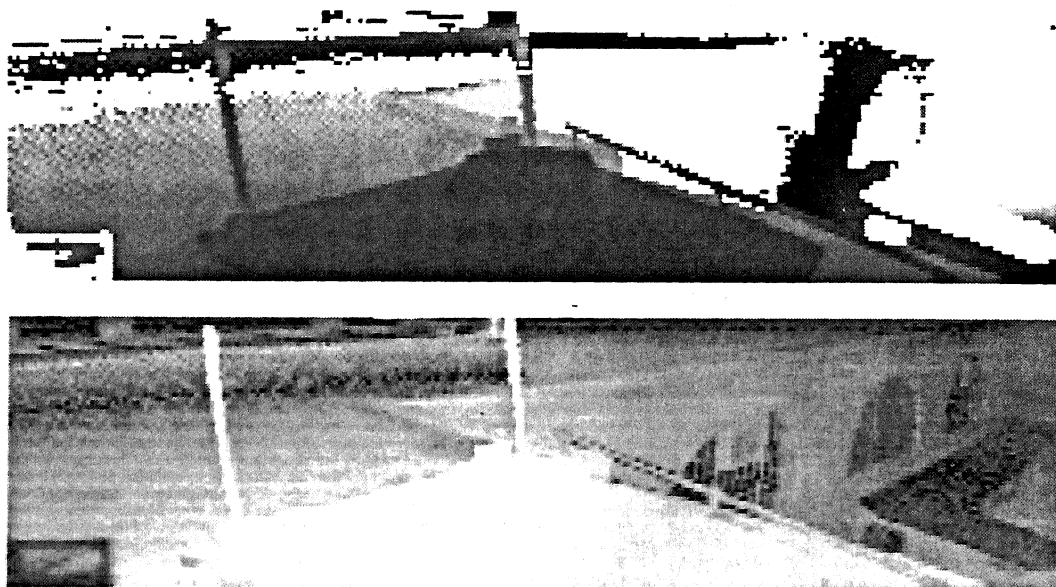


Figure 4.6: Range image of the sandbox (top) and reflectance image (bottom)

4.3 Thermal and Range Fusion

4.3.1 Principle of the Fusion

Thermal and range sensor are used in this section in a complementary fashion. The idea is to utilize the advantageous characteristics of one sensor in overcoming the disadvantages from the other one.

⁵The sandbox is at about 6m whereas the sensor can see points as far as 20m.



Figure 4.7: Range jump detection of the sandbox

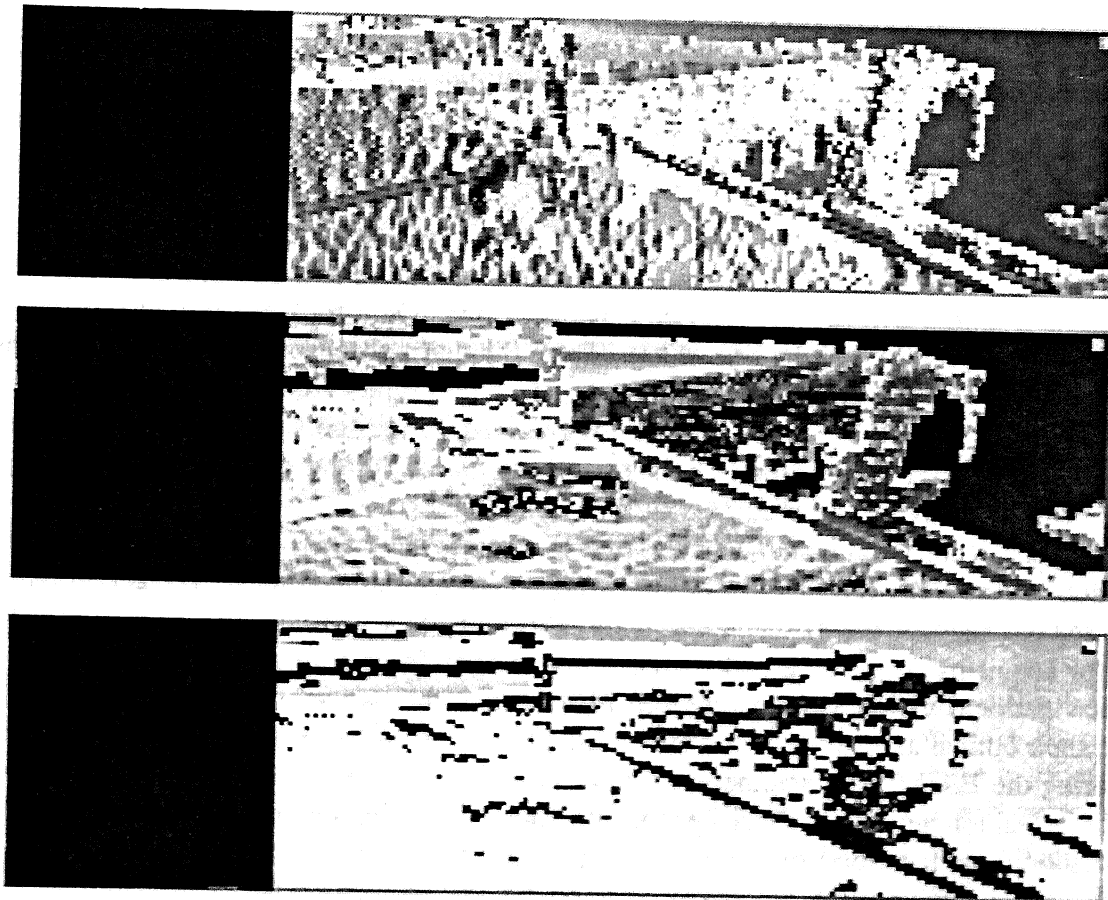


Figure 4.8: Normal vector along x,y,z axis

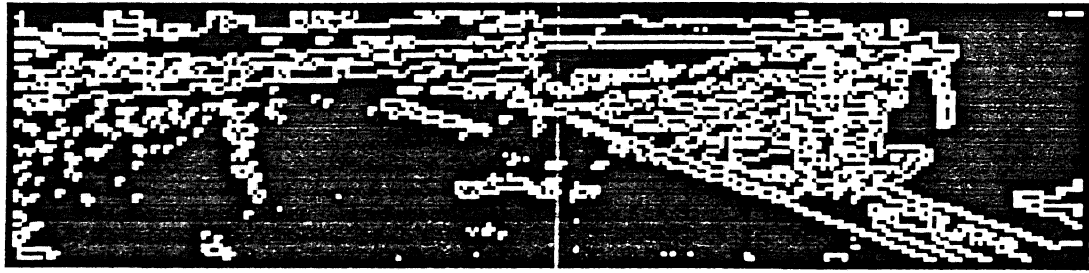


Figure 4.9: Normal variation detection of the sandbox

By combining the information from the two sensors, it is possible to better perceive the environment. Such an approach has been used in [15] with sonar and infrared information on a mobile robot. In that example, the sonar range finder measures the distance to an object but has poor angular resolution. The infrared sensor has good angular resolution that allow to detect the absence or presence of an object but it cannot measure distance accurately.⁶

In our case, the range sensor will detect edges and surface normals variation that usually correspond to the boundaries of objects. Thermal sensor will detect regions of uniform temperature that correspond to objects of different thermal inertia (i.e., different kinds of materials). The problem that we want to solve by combining information from the two sensors is the problem of occluded objects. Although thermal imaging allows to well discriminate objects that have different thermal inertia (for example, the small rock surrounded by sand in Figure 4.3), it can happen that two objects can not be distinguished because they have the same temperature and occlude each other. In that case, the thermal image will portray the two objects as one. On a rock covered terrain such as the martian terrain (see Figure 5.2), the line of sight from the thermal sensor usually includes rocks that occlude each other (see Figure 4.10). One example of this type of occlusion is the big rock and the background in Figure 4.3. In the case of Figure 4.10, range sensing can complement thermal imaging because a range jump usually exists between the occluding objects. By detecting those jumps it is possible to locate the boundary of the occlusion.

Before detecting the occlusions, we need first to register the thermal image and the range image of the sandbox in the same reference. The two imagers were mounted on the Navigation Laboratory (NavLab) for the need of the experiment. This laboratory is a van that contains on board all the facilities for acquiring, digitizing and memorizing images from several cameras. The Navlab is used for navigational vision system research [49]. Since the two sensors are located at different places and their optical axis are oriented differently, the two sensors must be calibrated. Techniques for calibrating the ERIM laser scanner and color camera [30] are well adapted for calibrating the range and thermal images. This is true because the thermal imager and the color camera are both 2D sensors. Although such calibration techniques are needed for precise and automatic data registration, we solved this problem manually by looking for the best correspondence between the edges of objects recognized by both thermal and range imager. We can consider that the two images are registered

⁶The infrared sensor is not a thermal camera. It emits a pulse of near-infrared light to sense any returned energy.

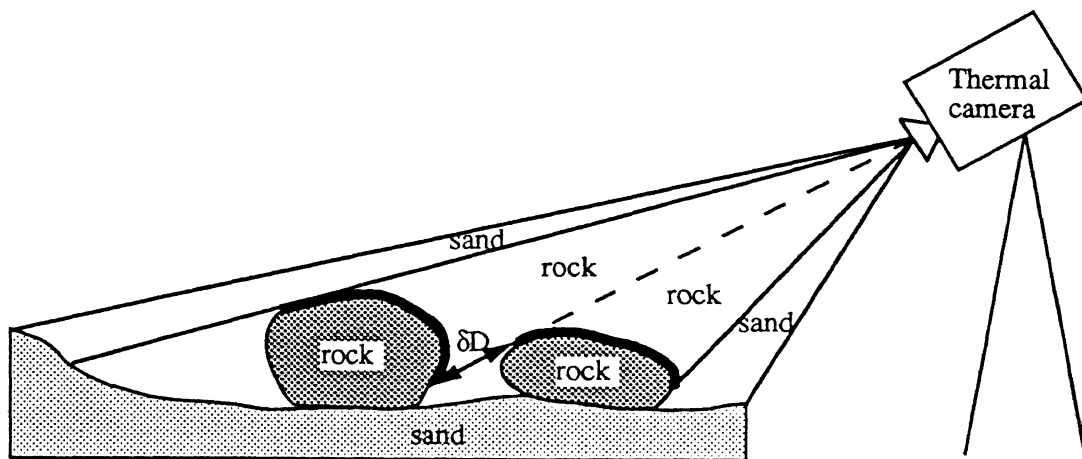


Figure 4.10: Occlusion of two rocks in the field of view of the imager

when edges are very clearly superposed (see Figure 4.11). To perform the correspondence, we looked for the set of parameters $\theta_R, \phi_R, M_x, M_z$ where θ_R and ϕ_R represent, respectively, the rotation angles of the 3D scene around the z-axis and the x-axis. M_x and M_z are the magnification factors along the axis ox and oz of the 3D scene. The determination of these parameters was performed "by hand" - a limited useful approach - on the particular case of our image. The fusion result is approximate since the true values for $\theta_R, \phi_R, M_x, M_z$ are unknown. The precision of the matching is of the order of the lowest resolution in distance of the two sensors at a distance of about $4m$ ($4m$ is the approximate distance between the cameras and the center of the sandbox). The horizontal angular resolution of the laser range finder is about 0.3° and the angular resolution of the thermal camera is about 0.08° . The lowest resolution in distance at a distance of $4m$ is obtained for the laser range finder and is about $2cm$ (corresponds to the distance between dots in Figure 4.11).

4.3.2 Results

Results of the fusion between the thermal and the range images of the sandbox are presented in Figure 4.11. The fusion method is considered successful since it is possible to relatively precisely extract the two rocks from the background. The upper edge of the big rock is well extracted because there is a depth jump between the rock and the background. In the upper left corner is presented the original thermal image. In the upper right corner is presented the segmented thermal image. In the lower left corner is presented the cartesian representation of the range image of the sandbox. Each dot represents a measurement from the laser range finder. As said in the previous section, the distance

between these points show that the spatial resolution of the laser range finder is much lower than the thermal imager.⁷ On this cartesian representation is superposed the segmented thermal image. The superposition is done as follows:

- If pixel intensity in range image = 255 and pixel intensity in segmented thermal image is = 255 then, pixel intensity in superposed image = 255.
- If pixel intensity in range image = 255 and pixel intensity in segmented thermal image is \neq 255 then, pixel intensity in superposed image is equal to intensity in segmented thermal image.
- If pixel intensity in range image = 0 then, pixel intensity in superposed image = 0.

In the lower right corner is presented the fusion of the two segmented images. The points are information from range data.

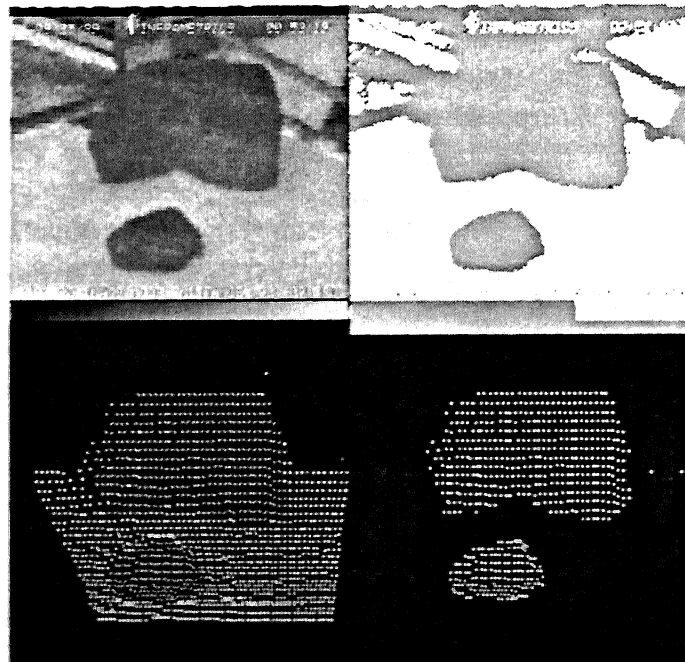


Figure 4.11: Segmentation of the two rocks

⁷256 × 64 with a field of view of 80° × 30° for the laser range finder while it is 256 × 200 with a field of view 20°H × 15°V for the thermal imager.

Chapter 5

Application for Autonomous Vehicles: a Case Study, the Mars Rover

A six legged robot called Ambler is being designed at Carnegie Mellon University (see Figure 5.1). The mission of this robot is the exploration of other planets, possibly Mars. The robot needs to know the geometry of the terrain in order to determine good paths over the very rugged terrain that can be encountered on the surface of other planets such as Mars [1, 24] (see Figure 5.2). For that purpose, the prototype of the robot is equipped with a laser range finder that allows constructing a geometric map of the terrain [19, 21]. Knowing the geometry of the terrain is however insufficient to certify the safety of a traverse path. Information about material nature is also needed.

In this chapter, we analyze thermal imaging techniques to acquire material information. Notice that the interest of using thermal imaging has already been anticipated in the context of the general requirements and alternatives for a mission on the planet Mars [47] (page 3-2).

First, we present simple calculation for determining the wavelength bands allowing thermal sensors to see material temperature on Mars. Second, by using thermal imaging techniques such as calculating thermal inertia and calculating size of the grain, we show that it is possible to identify materials found on the martian terrain. Third, we propose a complete vision system composed of a thermal camera and a laser range finder. Fourth, we show how this system can determine good footfall positions and gather samples of materials.

5.1 Infrared Technology for Mars

The mean atmosphere temperature on Mars is about 200K which is about 100K colder than on Earth. On Mars, the mean temperature in south polar regions can even reach less than 140K [26]. Viking primary missions [26] showed the atmospheric temperature ranged from 130K to 290K.

In order to see the possible use of thermal imaging for the exploration of a planet such as Mars, we need to answer to the following question: Can temperature this low be detected by current thermal

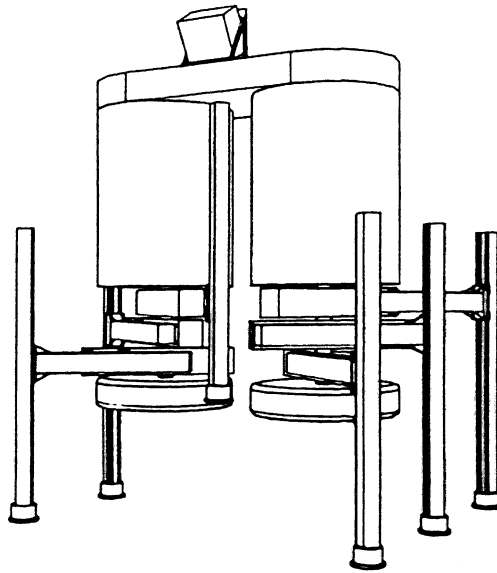


Figure 5.1: The Ambler



Figure 5.2: Martian landscape viewed by the Viking 2 lander

cameras?

So far, manufacturers have built thermal cameras for terrestrial applications. For that purpose, two wavelength bands are used, the band $8 - 12\mu m$ for detecting common terrestrial temperatures ($300K$) and the band $3 - 5\mu m$ to preferentially detect high temperature ($600K$) for industrial applications (see Chapter 2). Figure 2.2 illustrates in terms of emitted energy, why manufacturers use these two bands. At $300K$ the peak of the emitted energy curve is in the $8 - 12\mu m$ band and at $600K$ the peak is in the band $3 - 5\mu m$.

Since our problem is the detection of lower temperatures, we need to determine which bandwidth is the best suited. At the temperature of $200K$, bodies could not be detected by cameras using the $3 - 5\mu m$ since they do not emit any energy in the $3 - 5\mu m$ band (see Figure 2.2). The $8 - 12\mu m$ band is also non adequate since the current best cameras using this band only allow to detect temperature as low as $223K$. The emitted energy for temperature below $223K$ is too low to be detected in the band $8 - 12\mu m$. Which technological improvements are needed to perceive martian temperature?

First, notice by applying Equation 2.5 (Chapter 2) that the available energy (in all the spectrum) on Mars is only $91W/m^2$ at $200K$ while on Earth, it is $460W/m^2$ at $300K$. By using the technique presented in [51] (page 441), we find¹, that the energy in the band $8 - 12\mu m$ is $115W/m^2$ on Earth. Since only $91W/m^2$ are available on Mars, detecting energy in all the spectrum is not sufficient for collecting the $115W/m^2$ collected on the Earth. To collect a large amount of the available energy on Mars, we need to use a wider band than $8 - 12\mu m$. In fact, there is a tradeoff between the bandwidth and the energy collected: collecting much energy requires the sensor to be sensitive to a wide band; however, the wider the band is, the more difficult it is to build the sensor. Fortunately, most of the energy is concentrated in the lower part of the spectrum (see comments in Section 2.1.3). For example, we can obtain a large amount of the energy available on Mars (for instance 85%) by using the $8 - 40\mu m$ wavelength band.² The energy gained by increasing the bandwidth would be minimal since the band $8 - 60\mu m$ can only collect 8% more energy. By using the $8 - 40\mu m$ band, we can collect about $77W/m^2$. Although this energy is of the same order of magnitude as the energy available on Mars, it is still lower than the energy available in the $8 - 12\mu m$ on the Earth. Therefore, we also need to develop sensors more sensitive to thermal radiation than are currently available.

In summary, technological improvements in sensing matter is required to see the $200K$ usually encountered on the planet Mars. The two major improvements are firstly, using wide wavelengths band such as $8 - 40\mu m$ and second, increasing the sensor sensitivity. Moreover, although the military needs have already created robust systems for tactical applications, the thermal camera like the overall robot must work under the severe conditions of temperature. A special design for the electronics and the mechanics of the thermal device will certainly be needed.

¹The calculation is done by considering the tabulated equation of the emitted energy of a blackbody (for definition of a blackbody, see Chapter 2) at any wavelength and temperature.

²The determination of this band is performed by applying the technique presented in [51] page 441.

5.2 Known Characteristics of Martian Materials

The two Viking missions of 1977 allowed us to record large amounts of data about the planet Mars [22]. During these two missions, important information about the type of materials at the surface of the planet Mars was acquired by using an infrared mapper on board of an orbital station [26]. Physicists derived thermal inertia information from temperature measurements acquired by this mapper. The idea of deriving thermal inertia from temperature is the same as the one at the origin of our model (see Chapter 3). The only difference is that the thermal mapper was a telescope radiometer instead of a thermal camera and the resolution of the measurements on the planet was $120\text{km} \times 120\text{km}$ instead of a fraction of centimeters for a camera mounted on a robot scanning portions of terrain not larger than a few ten meters. For martian conditions, the principal thermophysical property determining the thermal inertia is the size of the particles. This dependence is a significant factor when describing the type of soils that can be encountered on Mars. We will show in detail in the following section why there is a direct relation between thermal inertia and grain size.

The thermal inertia range detected by orbiters' instruments was 70 to $500\text{Ws}^{1/2}/\text{m}^2\text{K}$. No areas were found where the thermal inertia exceeded $500\text{Ws}^{1/2}/\text{m}^2\text{K}$. Measurements at different points on the planet revealed several large well-defined areas of low thermal inertia ($I \leq 170\text{Ws}^{1/2}/\text{m}^2\text{K}$). Most likely, this is where the surface is covered by fine grained materials (dust whose diameter $\leq 100\mu\text{m}$) sand and has very few exposed rocks. The upper limit of $I = 500\text{Ws}^{1/2}/\text{m}^2\text{K}$ corresponds to sand thermal inertia (such as the one we used for the experiment described in Section 3.8). The low value found by the thermal mapper does not mean that there is only sand exposed on the surface of Mars. The fact that any value superior to $500\text{Ws}^{1/2}/\text{m}^2\text{K}$ has been found is due to the sample size ($120\text{km} \times 120\text{km}$) of the mapper. With such a resolution, the mapper determines a mean value of the thermal inertia. In fact, to produce such a low thermal inertia value, other materials exposed at the surface, such as rocks ($I \approx 2100\text{Ws}^{1/2}/\text{m}^2\text{K}$), must likely be associated with the fine material ($I \leq 170\text{Ws}^{1/2}/\text{m}^2\text{K}$) [26]. This was confirmed at the scale accessible to the two landers Viking 1 and 2 since there was ample evidence of exposed rock and bedrock surrounded by sandy areas (see Figure 5.2). Notice that for these two sites, the thermal inertia derived from orbiter's thermal measurements orbiter were about 380 and $335\text{Ws}^{1/2}/\text{m}^2\text{K}$ respectively.

5.3 Determining Size of the Grain

In this section, we address the problem of determining grain size of martian materials by using thermal imaging. Firstly, we demonstrate the relation between thermal inertia and grain size for martian conditions. Then, we show that the thermal model that we have developed theoretically allows us to reliably classify granular materials by increasing order of grain size.

5.3.1 Relation Thermal Inertia, Grain Size

In this section, we present and analyze the dependence between thermal inertia and size of the grain of materials on Mars. To do this, we will successively analyze the influence of the different parameters present in the thermal inertia equation:

$$I = \sqrt{k\rho_m c_p}$$

where k is the thermal conductivity, ρ_m is the density and c_p is the specific heat. This general relation, already seen in Section 3.6, is an expression of the temperature calculation (Equation 3.27).

For materials such as rock or sand, the conductivity can vary by several orders of magnitude from one material to another while density and specific heat change are much less. For example, for the sand and the sandstone rock used in the experiment in Section 3.8, conductivity for rock is about ten times sand value while density is only one and half times sand value and specific heat is almost the same. On the Earth, typical values for the density are $1500\text{kg}/\text{m}^3$ for sand and $2500\text{kg}/\text{m}^3$ for rock [24, 33, 34]. On Mars, sand and rock density is fairly similar to that of Earth since it is between 1000 and $1600\text{kg}/\text{m}^3$ for sand and between 2300 and $2900\text{kg}/\text{m}^3$ for rock [24, 33, 34]. For the specific heat, we could also expect values similar to those on Earth.

In fact, the determinant factor for the thermal inertia is the **conductivity**. We therefore concentrate on analyzing this parameter for the rest of this section. The conductivity itself depends on three main parameters [41]: **atmospheric pressure**, **moisture**, and **grain size** of the material. To understand the behavior of the conductivity, we have to analyze each of these three parameters.

- **Atmospheric Pressure**

The atmospheric pressure is the same for all the materials at the scale of the robot (a few hundred meters). Although this is a constant for a given location, the atmospheric pressure can vary with the altitude of the location. For example, if our location moves from the top of a mountain to the bottom of a crater, the ratio of atmospheric pressure variation can be ten (see Figure 5.3). This variation needs to be taken into account when calculating the thermal inertia for fine grained materials³ for which the atmospheric pressure has a strong influence.

Moreover, the magnitude of the atmospheric pressure leads to important information relating to thermal inertia of materials on different planets. The difference of atmospheric pressure between Mars ($10^2\text{N}/\text{m}^2$) and Earth ($10^5\text{N}/\text{m}^2$) explains the difference of thermal inertia for the same fine-grained materials located on Mars or Earth. The effect of gas pressure on thermal conductivity is represented in Figure 5.3. By using this graph, we determine that for the same material (sand used for our experiment in Section 3.8), $I \approx 200\text{Ws}^{1/2}/\text{m}^2\text{K}$ on Mars and $I \approx 60\text{Ws}^{1/2}/\text{m}^2\text{K}$ on the Moon while $I \approx 600\text{Ws}^{1/2}/\text{m}^2\text{K}$ on the Earth. Thermal inertia

³Fine grained materials are made of elementary grains separated by layers of atmosphere. To be fine grained, the diameter of the grain must be small enough (inferior to a few mm).

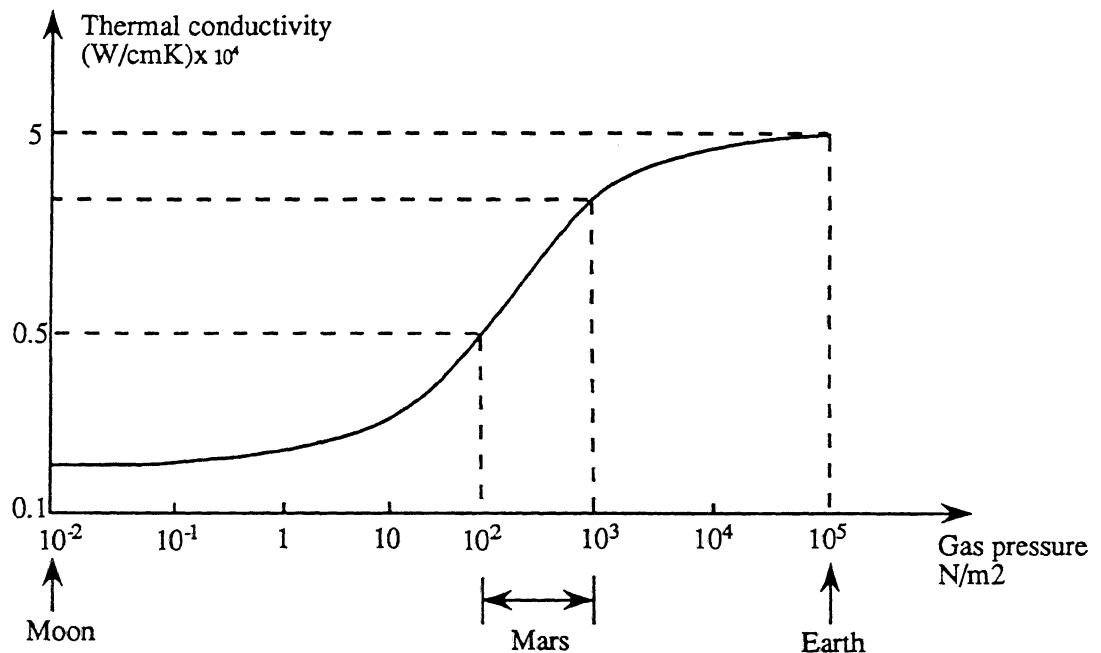


Figure 5.3: Conductivity as a function of gas pressure

for rock would be approximately the same on the three planets since gas pressure does not affect the thermal inertia of large grain [26].

This has an important meaning in terms of material temperature: the lower the thermal inertia, the higher the difference of temperature during the day. Since the thermal inertia of fine grained materials is lower on the Moon than on Earth, its variation of temperature during one entire day, should be higher on the Moon than on Earth. The temperature variation on Mars for the same rock, should be higher but in a smaller ratio than on Earth. The contrast in temperature between rock and sand on Mars should then be higher (see [26]). The discrimination between rock and sand would be then much easier on Mars than on Earth.

- **Moisture**

The moisture is an important parameter in the determination of the thermal inertia since the conductivity is largely dependent on the moisture. Conductivity as a function of moisture has been studied in [41]. The thermal conductivity increases with the moisture. Therefore, the thermal inertia increases with the moisture according to Equation 3.33. On Earth, the moisture must be taken into account to determine the thermal inertia of materials. On Mars, there is almost no moisture and the conductivity of fine grained materials is not affected by this parameter.

- **Size of the grain**

The parameter that can significantly change from one material to another on the planet Mars is the size of the grain. First, temperature measurements allow to know the thermal inertia. Secondly, in first approximation, thermal inertia allows to know the size of the grain.⁴ Higher the thermal inertia is, higher the size of the grain. Third, the size of the grain itself, is the parameter used to classify soils in different categories: Clay, Silt, Sand, Gravel, Cobbles and Boulders (see Figure 5.1). This classification [13] is called British Soil Classification. Therefore, from temperature measurements, we have a means to determine the place of the material in this classification. This relation is very important since it means that on Mars, it should be possible to determine in advance, without any probe of the terrain, the type of materials by using a thermal camera. For example, from the analysis done in Section 3.8, we can classify the sand in coarse sand category ($0.6 \leq \text{diameter} \leq 0.9$) and the rock among the boulders ($\text{diameter} \geq 0.9$).

Clay	Silt			Sand			Gravel			Cobbles	Boulders
	fine	medium	coarse	fine	medium	coarse	fine	medium	coarse		
	↓	↓	↓	↓	↓	↓	↓	↓	↓		↓
	0.002	0.006	0.02	0.06	0.2	0.6	2	6	20	60	200

Table 5.1: British Soil Classification

5.3.2 Using the Model to Determine Grain Size

On Mars, there are mainly two kinds of materials: rocks and sand. We know from the analysis lead in Chapter 3 that our model can reliably predict the qualitative behavior of these materials but cannot calculate precise value of their thermal inertia. Although erroneous, thermal inertia value for sand calculated from experimental data (see Section 3.10) is, as expected, lower than rock value at any time of the day. From this, we can conclude that the differentiation between rock and sand is ensured. But, on Mars there are several varieties of sand. We know for example that there is some dust that is composed of very fine particles and some sand whose grain is larger (see Section 5.2). Can we distinguish between these materials? Can we determine their grain size?

To answer these questions, we will use our model developed in Chapter 3. We know the thermal inertia for dust ($I \approx 200Ws^{1/2}/m^2K$) and for sand ($I \approx 550Ws^{1/2}/m^2K$). From our model, we know

⁴On the Moon for example, the conclusion is the same. Since there is no moisture on this planet, there is a direct relation between conductivity and size of the grain [9, 26, 32]. As soon as there is moisture, the problem is much more complicated since the thermal conductivity then depends on two parameters (size of the grain and moisture) that are a priori unknown.

that:

- $T(\text{dust}) < T(\text{sand})$, during the night
- $T(\text{dust}) > T(\text{sand})$, during sunshine

Furthermore, to distinguish between these two granular materials, the difference of temperature between both of them must be sufficient (superior to the resolution in temperature of the thermal camera). Indeed, a few degrees are sufficient since the difference of experimental temperature between sand and rock (only 3 to 4°K during the night) allows us to discriminate sand from rock (see Figure 3.14).

One of the curves in Figure 5.4 represents the difference of theoretical temperature between sand and dust for different values of time through the day. The other curve represents the difference of theoretical temperature between sand and rock. On this graph, except for time around the two contrast inversion points (sunrise and sunset), the difference of temperature is always superior to 2°K which is of the same order of magnitude as the experimental temperature difference between sand and rock. Therefore, we should be able to discriminate between sand and dust.

Although determined for Earth conditions, the thermal behavior of materials on Mars is fairly similar to the one on the Earth. From a qualitative point of view, the same type of graph would be obtained on Mars. Only the magnitude of the temperature would be different.

Calculating the thermal inertia by using the model will tell us which material has the larger grain size. Lower is the thermal inertia, lower the grain size. Unfortunately, we can not determine the precise value of grain size because there may be a large incertitude on the thermal inertia value calculated by the model.

From the previous analysis, we can distinguish between dust and sand and even classify fine-grained materials by increasing grain size. But, we cannot precisely calculate grain size value.

5.4 Vision Architecture to Identify Objects

In this section, we present a vision architecture for the Mars rover that uses a thermal imaging device and a laser range finder. The basic idea of this architecture is to use the thermal imager to acquire soil nature information, in particular the type of the material, and use the laser range finder to model the geometry of the terrain. There are two major blocks in this architecture (see Figure 5.5). The first block concerns the fusion of segmented thermal image and segmented range image as described in Chapter 4, while the second one is to calculate thermal inertia information of segmented regions generated by the fusion part.

The model as presented in Chapter 3 suffers from several limitations that have already been described. Those limitations are essentially related to the accuracy of the calculated thermal inertia. To be practically useful, several improvements can be done:

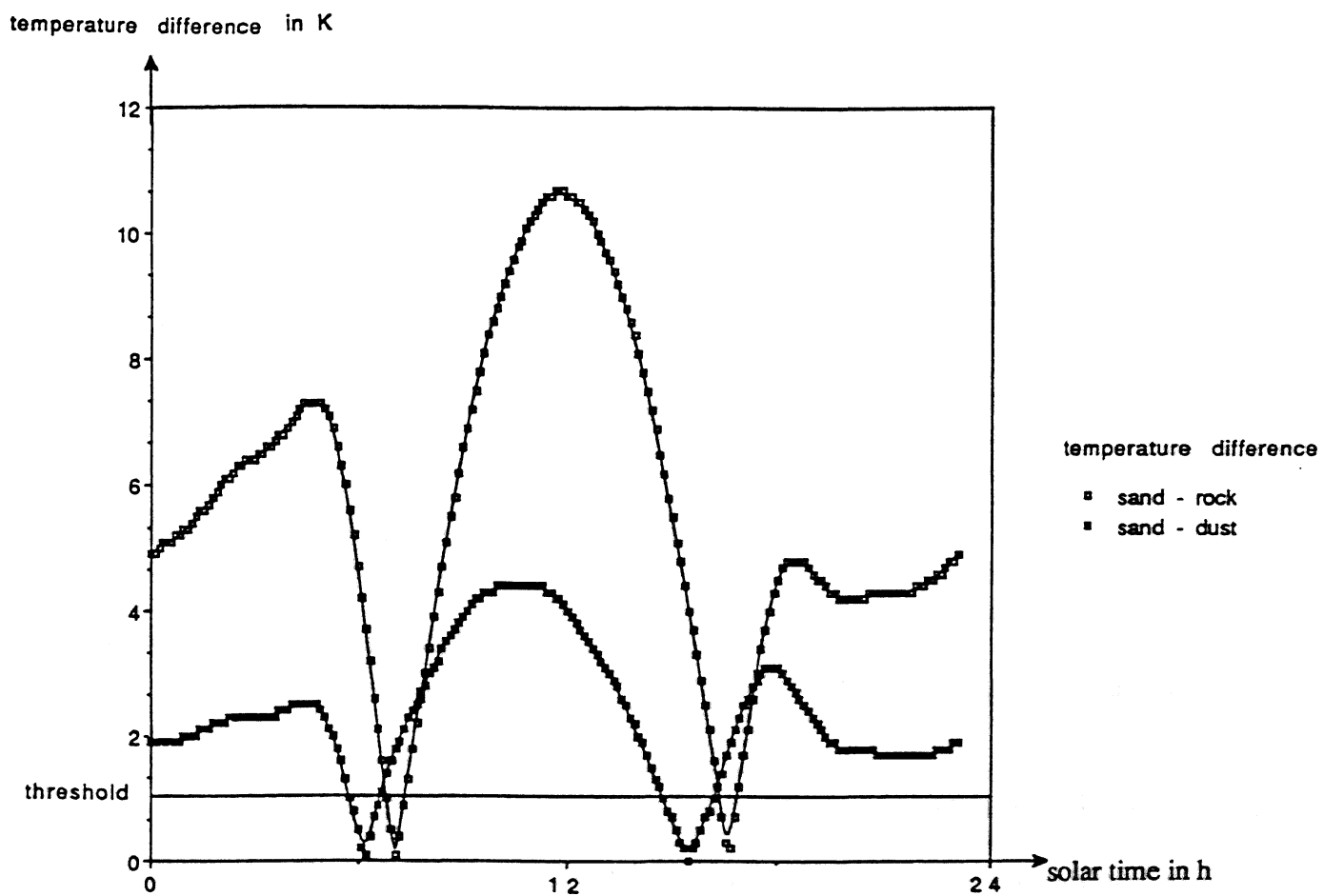


Figure 5.4: Temperature difference between several materials

- As mentioned in Chapter 3, instead of modeling the thermal radiation from the sun, it would be better to measure it by using a specific sensor such as a radiometer. Thus all the problems of cloud effect, transmissivity of the atmosphere, influence of the solar altitude on the direct solar radiation would be avoided at the same time.
- The influence of wind speed could be taken into account in a more precise way than what we have done in Chapter 3. Again, instead of modeling wind speed, it would be better to measure it and to integrate in the model its time dependent value.
- We have hypothesized that the reflectivity of the materials is a priori known because we know the type of environment in which the robot is evolving. For example, on Mars, material reflectivity is close to 0.24 for any material. In fact, to be much more accurate about this parameter, we propose to use reflectance map data from the laser range finder. The reflectance map is the same image as the range image but the pixel information is a quantity related to the reflectivity instead of being the range (see Figure 4.6). Thus, by registering pixel by pixel the information of reflectivity and thermal radiosity information, it could be possible to use precise reflectivity information in the model. We can notice that the grey level of rock and sand in Figure 4.6 is the same which means that the reflectivity for the two materials is the same.
- The knowledge of the atmosphere temperature is necessary to calculate emitted radiation from the atmosphere and convection energy between the body and the atmosphere. We have modeled the temperature of the atmosphere by a sinusoidal function but a better way to take into account the atmosphere temperature would be simply to measure it during the day and use these measurements in a numerical model.

5.5 Applications

In the two following sections, we describe how thermal imaging could be used to determine safe positions for the feet of the Ambler and interesting sites of collection for sampling in the context of an exploration of the planet Mars.

5.5.1 Determining Footfall Positions

The robot will have to place its six legs several millions of times on the martian landscape to cover the one hundred kilometers run specified for a sampling mission on Mars. Determining good footfall positions therefore appears to be a major task for the Mars Rover. It is particularly important on the very rough terrain that can be encountered on other planets such as Mars. At every step, the robot must know where to set its feet. Placing a foot at the wrong place, for example where the terrain is not stable, can be dangerous for the robot since it could slip or sink in the terrain. Probe

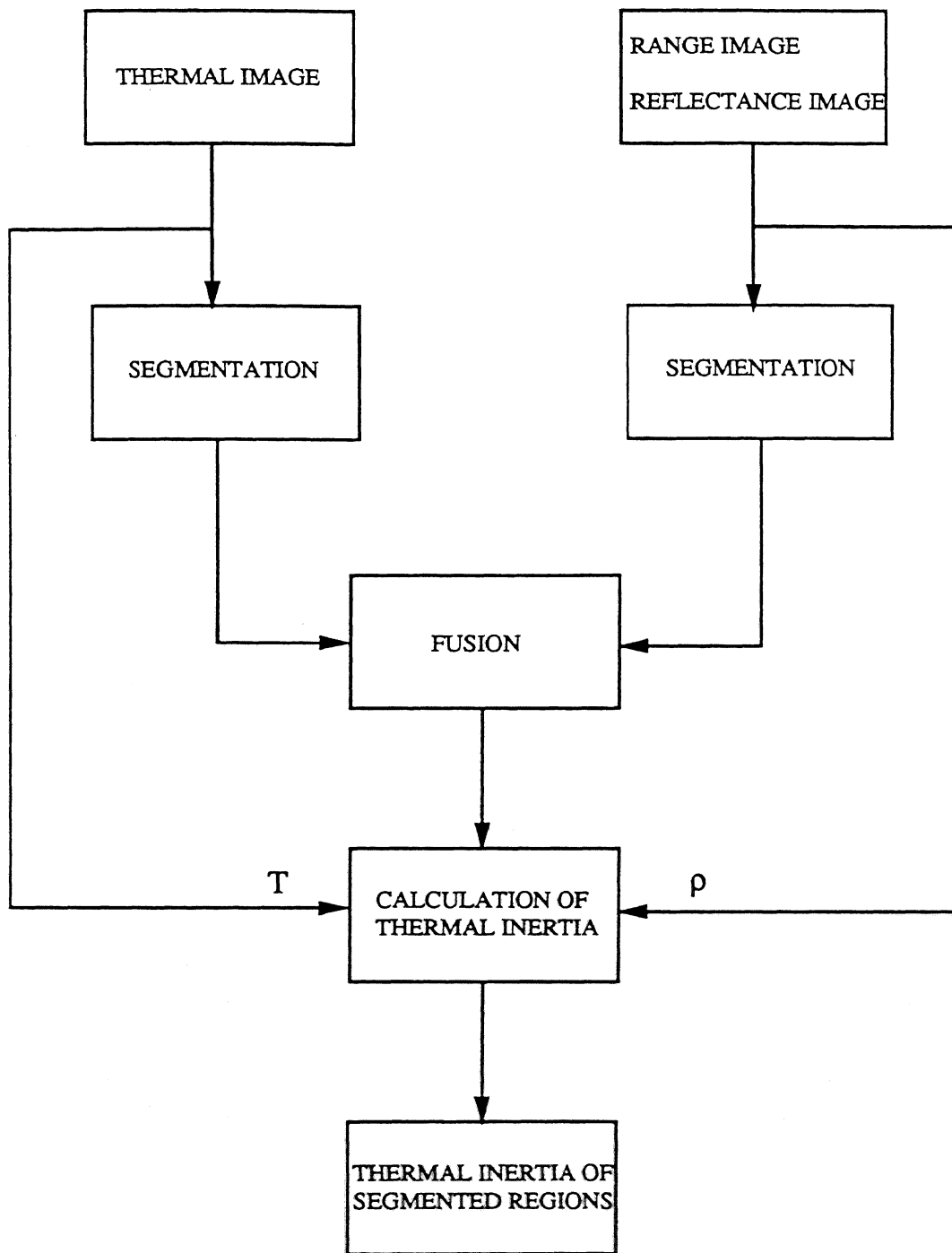


Figure 5.5: Vision architecture for the Mars Rover

of the terrain with the foot itself is certainly the best way to know the compliance of the terrain and its mechanical characteristics but it requires the robot to move the foot to the possible position. Since energy minimization is crucial for a complete autonomous robot, preselection by using vision sensors should allow the robot to decrease the energy and time required for walking.

We have developed several methods [7, 8] that use the geometric information of the terrain delivered by the laser range finder. These methods determine locations where the soil is flat. All of these methods have been tested on the single leg testbed that is currently working at Carnegie Mellon University. Unfortunately, although flatness is necessary to get good footfall positions, it does not ensure that a footfall position is completely safe.

As a complementary approach to these geometric methods, thermal imaging information can be used to infer soil nature information. As presented in Section 3.7, the temperature information allows us to derive thermal inertia information. Our model is not always accurate enough for determining true values of the thermal inertia. However, applying the model to experimental (see Section 3.8) data has shown, as expected, that sand has a lower thermal inertia than rock at any time of the day or the night. In the case of the martian surface mainly composed of sand and rock, we can therefore reliably discriminate sand from rock. Since the robot has the knowledge of the type of material in front of its feet, it can decide whether or not to set its feet on sand rather than rock. We think that the discrimination between several types of sand, distinct from each other by the size of their grain, is also possible. Since different kinds of sand have different thermal inertias, applying the model as presented in Section 3.10 should allow us to discriminate them. No experiment has yet been done to verify this hypothesis. In the future, we intend to do this type of experiment to evaluate whether their practical performance live up to their theoretical promise.

5.5.2 Determining Material Collection Site

The principal mission for the robot will be to collect samples of materials. It seems that interesting samples of material have typically a size of the grain in the range of 0.1mm for sand and a few centimeters in diameter for pebbles.

Nowadays, laser range finder can have a good resolution in distance, typically 0.1cm . They can see pebbles a few centimeters in diameter and are therefore interesting for sampling. Although it is possible to do much with range techniques [20], they present several limitations. First, to be seen by a range sensor a pebble must present some apparent geometric features such as surface normal variation or range jumps. These features allow the pebble to be discriminated from its surrounding environment. Discriminating a pebble that is at the same level as the soil or presenting too smooth geometric features is delicate (see Figure 5.6). Secondly, the range finder can not differentiate several types of fine grained materials because the diameter of the grain is too small. For example, the range finder can not discriminate a sample of granular material whose size of the grain is 0.1mm from another sample whose size of the grain is 1mm .

In the first case thermal imaging can discriminate a pebble that is at the same level as the surrounding environment because the discrimination is based on material characteristic and not on

geometric features (see Section 4.1.1). In the second case, we think that thermal imaging should be able to determine an approximate value of the thermal inertia of the two fine grained materials (the theoretical values are $I = 200Ws^{1/2}/m^2K$ for $0.1mm$ and $I = 550Ws^{1/2}/m^2K$ for about $1mm$). The difference of theoretical temperature between these two materials during the day is of the order of 2 to $4K$ (Figure 5.4). This difference suffices to the camera to see two different kinds of materials since the range of temperature does not usually exceed a few ten of degrees. We intend to perform this type of experiment to verify if the differentiation between the two materials is possible. On Mars, we could expect a higher difference of temperature between those materials because the thermal inertia would be lower than on Earth for each of the materials. In fact, the fusion of range and thermal information could improve the capacity to detect (see Section 4.3), to locate and to determine to some extent possibly interesting samples of material.



Figure 5.6: Pebble set on the soil (left), pebble at soil level (right)

Chapter 6

Discussions and Future Work

We have presented new techniques based on thermal imaging to discriminate objects in outdoor scenes. In this chapter, we will both summarize and discuss the thermal model results, results of pure segmentation algorithms and the interest of thermal imaging to explore Mars by an autonomous robot. We will precise the different promising areas and future directions of research.

First, the **thermal model** that we have developed theoretically allows to discriminate materials by calculating their thermal inertia. In the development of our model, we have presented two kinds of results:

- Quantitative results

On one hand, comparison of theory with experiment shows that relatively accurate quantitative values of thermal inertia can be obtained during day time for sand. But, this is not true during the night. On the other hand, inaccurate quantitative values are obtained for the rock during day and night because the dimensions of the rock are not suitable for the model. Furthermore, it seems that the strong sensitivity of the model to parameters such as wind speed and body shape limits its applicability for acquiring precise quantitative value for the thermal inertia. Major improvements for calculating the temperature and then the thermal inertia would be:

1. measuring solar radiation, wind speed and atmospheric temperature instead of modeling them.
2. taking into account a more realistic shape for the body such as the juxtaposition of elementary planar facets instead of the assumption of a semi-infinite body. In that case, the orientation of the facets relating to the sun direction must be taken into account.

and then, used a numerical model to obtain more accurate quantitative values for the temperature and the thermal inertia.

- Qualitative results

On the qualitative point of view, we have shown that our model is much more reliable than on the quantitative point of view.

1. The experiment showed, as predicted by the model, the existence of two points called contrast inversion points corresponding approximately to sunrise and sunset. For those two points, temperatures of the two materials are the same. Rock is warmer than sand during the night while it is colder during sunshine.
2. We performed some simulations in a large range of values of wind speed that showed that the previous thermal behavior of rock and sand is still the same. Another way to express this, is to calculate the thermal inertia. We found that the thermal inertia value calculated by using the model is, as expected, lower at any time of the day for sand than for rock.
3. In the development of our model, we made some restrictive hypothesis about solar irradiation since we supposed a clear sky without any clouds. Experimental results presented in Figure 4.3 tend to confirm that even by cloudy sky, sand is still warmer than rock during sunshine. This is true although the small rock does not satisfy the condition of semi-infinite body (its dimensions are much lower than the dimensions imposed by the model). From this, we think that the qualitative thermal behavior of rock and sand is the same as the one predicted by our model in a much broader class of conditions than those foreseen by the model. Further experiment should however be done to verify the truth of this statement and its exact limits.

Second, we applied, in Chapter 4, a **segmenting algorithm** to thermal images of a scene composed of rock and sand. We obtained fairly good results due on one hand to important difference of temperature between sand and rock and on the other hand to the relatively uniform brightness of body surface (see Figure 4.1 Figure 4.2 and Figure 4.3). Segmenting thermal images by using pure vision algorithms is therefore a promising area of research to distinguish between materials such as rock and sand. Segmenting images from a black and white camera did not lead to so good results as thermal ones because brightness for rock and sand in a black and white image are almost the same and are largely dependent on surface orientation. This tends to prove that a thermal sensor would be an excellent candidate to explore sandy and rocky areas.

Third, **occluding objects** such as rocks cannot be distinguished by thermal cameras because their temperature is almost the same. 3D vision techniques can discriminate between them because there is usually a range jump between these objects. Combining thermal and range data has been successful to discriminate between one rock that occludes the background whose temperature is almost the same as the rock. This technique seems promising to discriminate occluding bodies composed of the same material. In the future, we intend to do further research to combine thermal and range information.

Fourth, we have studied an **application for these techniques**: an exploration of the surface of Mars by a legged robot. Walking requires to know what the soil is made of (sandy, rocky,...)

while sampling that is the main mission of the robot requires to be able to discriminate and locate materials such as boulder, gravel, sand, ... We know from the results of Chapter 3 that we can reliably distinguish between rock and sand by calculating their thermal inertia. Furthermore, we showed that on Mars, the thermal inertia is essentially related to grain size. We intend to experiment with dust and sand to evaluate whether the practical performance lives up to the theoretical promises. We can notice that discriminating between dust and sand seems not to be possible with laser range finders or visible light cameras since the reflectivity of those materials are almost the same. Distinguishing between dust, sand and rock is a major advantage for walking since the knowledge of the type of material should allow the robot to infer certain soil features such as compliance, load-bearing strength, and coefficient of friction. Moreover, differentiating between granular materials finds interesting applications for sampling materials.

In conclusion, thermal imaging techniques seem to be promising for discriminating different kinds of materials in outdoor scenes, in particular for a planetary exploration. More work has to be done before incorporating a thermal sensor on the robot. For that, we have precised in this chapter, several directions of research: **thermal modeling**, **segmenting** and **thermal combined with range data** that should allow us to build a complete vision system for a planetary rover.

Appendix A

Analytical Calculations

A.1 One-dimensional Heat Equation

In this section, we establish the heat equation in the one dimensional case. The basic differential equation of heat conduction is a combination of the energy conservation law and Fourier's law [51]. Let us consider a slab of material whose width is taken very small Δx and adjacent surfaces are plane parallel of area S as represented in Figure A.1. The density of the material is ρ_m , its specific heat c_p and conductivity k . We assume that the heat flux $E_{cd}(x)$ crosses through the slab in direction x . No heat can come from the lateral facets of the slab.

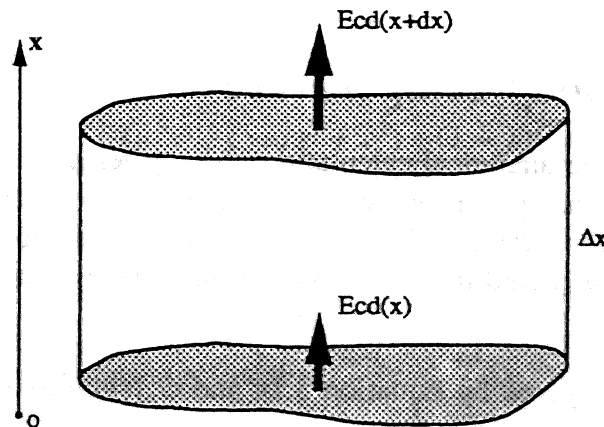


Figure A.1: Heat flux along the x-axis

First, if we make the hypothesis that all properties vary smoothly enough to use numerical

calculus then:

$$E_{cd}(x + dx) = E_{cd}(x) + \frac{\partial E_{cd}(x)}{\partial x} \Delta x \quad (\text{A.1})$$

Second, Fourier's law relates flux of energy to gradient of temperature by the following relation:

$$E_{cd}(x) = -k \frac{\partial T}{\partial x} \quad (\text{A.2})$$

Third, the law of energy conservation applied to the element of volume limited to the cube represented in Figure A.1 leads to the equation:

$$(E_{cd}(x) - E_{cd}(x + dx))S = (\rho_m S \Delta x) c_p \frac{\partial T}{\partial t} \quad (\text{A.3})$$

then, by substituting Equation A.1 and Equation A.3 in Equation A.2 it comes:

$$\frac{\partial}{\partial x} \left(k \frac{\partial T}{\partial x} \right) = \rho_m c_p \frac{\partial T}{\partial t} \quad (\text{A.4})$$

If the conductivity k is a constant (i.e., does not depend on x, y, z) then Equation A.4 can be written:

$$\frac{\partial T}{\partial t} = \frac{k}{\rho_m c_p} \frac{\partial^2 T}{\partial x^2} \quad (\text{A.5})$$

This is the heat equation presented in Section 3.4.

A.2 Calculating Body Temperature

In this section, we present the analytical calculation of body temperature in outdoor scene. The problem consists of solving the system of two equations that govern the temperature behavior of bodies (see System 3.25). The first equation is the equation of heat conduction, the second is the boundary condition. As already said in Section 3.4, to solve the system, we have to replace in the boundary equation:

- $G_s(t)$ by its expression given by Equation 3.14 and $G_a(t)$ by its expression given by Equation 3.13.
- the non-linear terms (T^4) in this equation by a linear expression (see Equation 3.26).

To solve the system of the differential equation and the boundary condition we use the Laplace transformation of variable noted s with respect to the variable t . This powerful method is very often

used to solve physical problems in which differential equations are involved. By definition, the Laplace transformation $\bar{f}(x, s)$ of a function $f(x, t)$ is defined as follows:

$$\bar{f}(x, s) = \int_0^{\infty} e^{-st} f(x, t) dt \quad (\text{A.6})$$

After Laplace transformation, the system of two equations become:

$$\begin{cases} s\bar{T} = a \frac{d^2 \bar{T}}{ds^2} \\ (1 - \rho)\bar{G}_s + \frac{\mu}{s} + \frac{\lambda\omega}{s^2 + \omega^2} = \nu\bar{T}(0, s) - k \left(\frac{d\bar{T}}{dx} \right)_{x=0} \end{cases} \quad (\text{A.7})$$

where \bar{T} denotes the Laplace transform of the function T . In order to symplify the notation, we have set:

$$\mu = A [(1 - \rho)\epsilon_a - \epsilon_s] + T_1 [(1 - \rho)\epsilon_a B + h] \quad (\text{A.8})$$

$$\lambda = -(\epsilon_a B + h)T_2 \quad (\text{A.9})$$

$$\nu = h + \epsilon_s B \quad (\text{A.10})$$

$$\omega = \frac{2\pi}{24} \quad (\text{A.11})$$

We recognize in Equation A.7 the well known differential equation of the second order of constant coefficients. The general solution of this equation is

$$\bar{T}(x, s) = G_1 \exp \left[-x \left(\frac{s}{a} \right)^{1/2} \right] + G_2 \exp \left[x \left(\frac{s}{a} \right)^{1/2} \right] \quad (\text{A.12})$$

G_2 is necessarily equal to 0 because $T(\infty, s)$ must be finite. By replacing the previous expression of \bar{T} in the boundary condition equation, we obtain the expression that allows to extract G_1 as a function of the other parameters.

$$G_1 = \frac{(\mu/s) + (\lambda\omega/s^2 + \omega^2) + (1 - \rho)\bar{G}_s(t)}{\nu + k(s/a)^{1/2}} \quad (\text{A.13})$$

Then, the general solution of the system of equations in the Laplace domain is

$$\bar{T}(x, s) = \left[\frac{(\mu/s) + \lambda\omega/(s^2 + \omega^2) + (1 - \rho)\bar{G}_s(t)}{\nu + k(s/a)^{1/2}} \right] \exp \left[-x \left(\frac{s}{a} \right)^{1/2} \right] \quad (\text{A.14})$$

$\bar{T}(x, s)$ is the sum of three elementary functions $\bar{T}_1(x, s)$, $\bar{T}_2(x, s)$ and $\bar{T}_3(x, s)$ such that:

$$\begin{aligned} \bar{T}_1(x, s) &= \frac{\mu}{s(\nu + k(s/a)^{1/2})} \exp \left[-x \left(\frac{s}{a} \right)^{1/2} \right] \\ \bar{T}_2(x, s) &= \frac{\lambda\omega}{(s^2 + \omega^2)(\nu + k(s/a)^{1/2})} \exp \left[-x \left(\frac{s}{a} \right)^{1/2} \right] \\ \bar{T}_3(x, s) &= \frac{(1 - \rho)\bar{G}_s(t)}{\nu + k(s/a)^{1/2}} \exp \left[-x \left(\frac{s}{a} \right)^{1/2} \right] \end{aligned} \quad (\text{A.15})$$

In order to find the expression of the temperature as function of time and distance, we have to calculate the residues for each of the poles of the three functions \overline{T}_1 , \overline{T}_2 and \overline{T}_3 . The poles are defined as being the values of s for which the denominators of \overline{T}_1 , \overline{T}_2 and \overline{T}_3 are equal to zero. The pole can be simple if the denominator is equal to 0 once, double if the denominator is equal to 0 twice and so on. The rest of the calculation in this section aims to determine the residues of these three functions. The sum of all the residues gives the expression of the temperature as function of t and x .

- **Case of \overline{T}_1**

The only pole of T_1 is $s = 0$ that is also a critical point. $\overline{T}_1(x, s) \simeq \mu/\nu s$ then, $\overline{T}_1(\infty, s) = \mu/\nu$ and

$$T_1(x, t) = \mu/\nu \quad (\text{A.16})$$

- **Case of \overline{T}_2**

T_2 has two poles $s = \pm i\omega$ and $s = 0$ is a critical point. To calculate the residues for these two poles, we have to calculate the two following limits:

$$\lim_{s \rightarrow +i\omega} (s - i\omega) \overline{T}_2(x, s) \exp(st) \quad (\text{A.17})$$

$$\lim_{s \rightarrow -i\omega} (s + i\omega) \overline{T}_2(x, s) \exp(st) \quad (\text{A.18})$$

To simplify the notation, we set for the remainder of this appendix:

$$\begin{aligned} p &= \frac{\lambda}{\nu} \\ q &= \frac{k}{\nu} \sqrt{\frac{\omega}{2a}} \\ \xi &= x \sqrt{\frac{\omega}{2a}} \end{aligned} \quad (\text{A.19})$$

Then, the limits for $s = i\omega$ and $s = -i\omega$ are respectively:

$$\frac{p}{2i[1 + q(1 + i)]} \exp[-\xi(1 + i) + i\omega t] \quad (\text{A.20})$$

$$\frac{-p}{2i[1 + q(1 - i)]} \exp[-\xi(1 - i) - i\omega t] \quad (\text{A.21})$$

The inverse function of the Laplace function is then:

$$T_2(0, t) = \frac{p}{\sqrt{1 + 2q + 2q^2}} \exp(-\xi) \sin(\omega t - \xi - \theta) \text{ where } \theta = \tan^{-1} \left(\frac{q}{1 + q} \right) \quad (\text{A.22})$$

• Case of \bar{T}_3

In order to calculate the poles of T_3 , we have first to find the expression of the Laplace transform of $G_s(t)$. By definition of the Laplace transform, we have:

$$\bar{G}_s = \int_0^{\infty} e^{-st} G_s(t) dt \quad (\text{A.23})$$

where $G_s(t)$ is given by Equation 3.9. Since G_s is a periodic function whose period is equal to $2\pi/\omega = 24$ the Laplace transform can be written:

$$\bar{G}_s(t) = \frac{1}{1 - e^{-24s}} \int_0^{24} e^{-st} G_s(t) dt \quad (\text{A.24})$$

The complete calculation of the Laplace transform of $G_s(t)$ leads to a rather complicated expression that can be written as the sum of three elementary functions \mathcal{G}_{p1} , \mathcal{G}_{p2} and \mathcal{G}_{p3}

$$\bar{G}_s(t) = \frac{\bar{G}_{p1} + \bar{G}_{p2} + \bar{G}_{p3}}{\nu + k(s/a)^{1/2}} \exp \left[-x(s/a)^{1/2} \right] \quad (\text{A.25})$$

$$\mathcal{G}_{p1}(x, s) = \frac{\bar{G}_{p1}}{\nu + k(s/a)^{1/2}} \exp \left[-x(s/a)^{1/2} \right] \quad (\text{A.26})$$

$$\mathcal{G}_{p2}(x, s) = \frac{\bar{G}_{p2}}{\nu + k(s/a)^{1/2}} \exp \left[-x(s/a)^{1/2} \right] \quad (\text{A.27})$$

$$\mathcal{G}_{p3}(x, s) = \frac{\bar{G}_{p3}}{\nu + k(s/a)^{1/2}} \exp \left[-x(s/a)^{1/2} \right] \quad (\text{A.28})$$

where

$$\bar{G}_{p1} = \frac{-uG'_0}{s(1 - e^{(-2\pi/\omega)s})} \left[e^{-s(\pi/\omega + (1/\omega) \cos^{-1}(-u/r))} - e^{-s(\pi/\omega - (1/\omega) \cos^{-1}(-u/r))} \right] \quad (\text{A.29})$$

$$\bar{G}_{p2} = \frac{uG'_0 s}{(s^2 + \omega^2)(1 - e^{(-2\pi/\omega)s})} \left[e^{-s(\pi/\omega + (1/\omega) \cos^{-1}(-u/r))} - e^{-s(\pi/\omega - (1/\omega) \cos^{-1}(-u/r))} \right] \quad (\text{A.30})$$

$$\bar{G}_{p3} = \frac{rG'_0[1 - (u/r)^2]^{1/2}\omega}{(s^2 + \omega^2)(1 - e^{(-2\pi/\omega)s})} \left[e^{-s(\pi/\omega + (1/\omega) \cos^{-1}(-u/r))} + e^{-s(\pi/\omega - (1/\omega) \cos^{-1}(-u/r))} \right] \quad (\text{A.31})$$

$$G'_0 = \tau(1 - \rho) \quad (\text{A.32})$$

Thus, the initial problem of finding the poles of \bar{T}_3 can be split in three smaller problems that are the determination of the poles and then the inverse Laplace transform of the three elementary functions $\bar{\mathcal{G}}_{p1}$, $\bar{\mathcal{G}}_{p2}$ and $\bar{\mathcal{G}}_{p3}$:

1. Case of $\overline{\mathcal{G}_{p1}}$

The poles for this function are $s = 0$ that is also a critical point and $s = ni\omega$ where $n \in \mathbb{Z}^*$. For $s = 0$, we find the following equivalence:

$$\overline{\mathcal{G}_{p1}}(x, s) \simeq \frac{uG'_0 \cos^{-1}(-u/r)}{\nu\pi s} \quad (\text{A.33})$$

The residue for $s = 0$ is given by $\lim_{s \rightarrow 0} s \overline{\mathcal{G}_{p1}}(x, s) \exp(st)$ whence:

$$\text{residue} = \frac{uG'_0 \cos^{-1}(-u/r)}{\nu\pi} \quad (\text{A.34})$$

For $s = ni\omega$, we calculate $\lim_{s \rightarrow ni\omega} (s - ni\omega) \overline{\mathcal{G}_{p1}}(x, s) \exp(st)$. After a rather long calculation, we find that the residues for $n > 0$ and $n < 0$ are respectively:

$$\text{residue1} = \frac{u}{\nu\pi} \frac{(-1)^n}{n(1 + q\sqrt{ni\omega})} \sin(n \cos^{-1}(-u/r)) \exp(-\xi(1 + i)\sqrt{n}) \exp(ni\omega t) \quad (\text{A.35})$$

$$\text{residue2} = \frac{u}{\nu\pi} \frac{(-1)^n}{(-n)(1 + q\sqrt{ni\omega})} \sin(-n \cos^{-1}(-u/r)) \exp(-\xi(1 - i)\sqrt{n}) \exp(-ni\omega t) \quad (\text{A.36})$$

Then, the sum of these two residues for $n \in \mathbb{Z}^*$ gives:

$$\sum \text{residue} = \frac{2uG'_0}{\nu\pi} \sum_{n=2}^{\infty} \frac{(-1)^n \exp(-\xi\sqrt{n})}{n\sqrt{1 + 2qn^{1/2} + 2q^2n}} \sin[n \cos^{-1}(-u/r)] \cos(n\omega t - \xi\sqrt{n} - \theta_n) \quad (\text{A.37})$$

2. Case of $\overline{\mathcal{G}_{p2}}$

The poles of this function are $s = \pm ni\omega$ where $n \in \mathbb{Z}^*$ and $s = \pm i\omega$ that are double poles. After a rather lengthy calculation that requires the use of L'Hopital's rule (mathematical details of this rule can be found in [29] page 131), it is possible to show that $s = \pm i\omega$ are simple poles for the function $\overline{\mathcal{G}_{p2}} + \overline{\mathcal{G}_{p3}}$.

The calculation of the two residues for $s = i\omega$ and $s = -i\omega$ leads to the following result:

$$\text{residue}(i\omega) = \frac{(uG'_0/2\pi)\sqrt{[1 - (u/r)^2]1/2 - (r/2\pi)\cos^{-1}(-u/r)}}{\nu[1 + q(1 + i)]} \exp(-\xi(1 + i) + i\omega t) \quad (\text{A.38})$$

$$\text{residue}(-i\omega) = \frac{(uG'_0/2\pi)\sqrt{[1 - (u/r)^2]1/2 - (r/2\pi)\cos^{-1}(-u/r)}}{\nu[1 + q(1 - i)]} \exp(-\xi(1 - i) - i\omega t) \quad (\text{A.39})$$

Then, the sum of these two residues gives

$$\sum \text{residue} = \frac{(uG'_0/\pi)\sqrt{[1 - (u/r)^2]}1/2 - (r/\pi)\cos^{-1}(-u/r)}{\nu\sqrt{1 + 2q + 2q^2}} \exp(-\xi)\cos(\omega t - \xi - \theta) \quad (\text{A.40})$$

Calculation of the residue of $\overline{G_{p2}}$ for $n \neq \pm 1$

$$\text{residue}(ni\omega) = \frac{uG'_0}{\nu\pi} \frac{(-1)^n}{1 - n^2} \sin \left[n \cos^{-1}(-u/r) \right] \frac{1}{1 + qn^{1/2}} \exp(-\xi(1+i)\sqrt{n} + ni\omega t) \quad (\text{A.41})$$

$$\text{residue}(ni\omega) = \frac{uG'_0}{\nu\pi} \frac{(-1)^n}{1 - n^2} \sin \left[n \cos^{-1}(-u/r) \right] \frac{1}{1 + qn^{1/2}} \exp(-\xi(1-i)\sqrt{n} - ni\omega t) \quad (\text{A.42})$$

By gathering the residues of rank n with the residues of rank $-n$, we obtain the following expression for the sum of the residues:

$$\sum \text{residue} = \sum_{n=2}^{\infty} \frac{2G'_0}{\nu\pi} \frac{u(-1)^n \exp(-\xi\sqrt{n})}{1 - n^2} \sin \left[n \cos^{-1}(-u/r) \right] \frac{\cos(n\omega t - \xi\sqrt{n} - \theta)}{\sqrt{1 + 2qn^{1/2} + 2q^2n}} \quad (\text{A.43})$$

There is no pole for $n = 0$.

3. Case of $\overline{G_{p3}}$

The poles of this function are $s = \pm ni\omega$ where $n \neq \pm 1$. The calculation leads to the following expression:

$$\text{residue} = \frac{2G'_0 r \sqrt{1 - (u/r)^2}}{\nu\pi} \frac{(-1)^n}{1 - n^2} \cos \left[n \cos^{-1}(-u/r) \right] \frac{1}{1 + qn^{1/2}} \exp(-\xi(1+i)\sqrt{n} + ni\omega t) \quad (\text{A.44})$$

$$\text{residue} = \frac{2G'_0 r \sqrt{1 - (u/r)^2}}{\nu\pi} \frac{(-1)^n}{1 - n^2} \cos \left[n \cos^{-1}(-u/r) \right] \frac{1}{1 + qn^{1/2}} \exp(-\xi(1-i)\sqrt{n} - ni\omega t) \quad (\text{A.45})$$

Like the calculation of the residues for $\overline{G_{p2}}$, we sum the residue of rank n with the residue of rank $-n$. After gathering the terms, we obtain:

$$\sum_{n=2}^{\infty} \frac{2G'_0 r \sqrt{1 - (u/r)^2}}{\nu\pi} \frac{(-1)^n \exp(-\xi\sqrt{n})}{1 - n^2} \cos \left[n \cos^{-1}(-u/r) \right] \frac{\cos(n\omega t - \xi\sqrt{n} - \theta_n)}{\sqrt{1 + 2qn^{1/2} + 2q^2n}} \quad (\text{A.46})$$

For $n = 0$, the residue is:

$$\frac{G'_0}{\nu\pi} r \sqrt{1 - (u/r)^2} \quad (\text{A.47})$$

The complete expression of the temperature as function of time t and depth x is the sum of the elementary functions $T_1(x, t)$, $T_2(x, t)$ and $T_3(x, t)$ found along the calculation. The variable x is present in the expression of the temperature via ξ .

$$\begin{aligned}
T(\xi, t) = & \frac{\mu}{\nu} + \frac{G'_0}{\nu\pi} \left\{ u \cos^{-1}(-u/r) + r[1 - (u/r)^2]^{1/2} \right\} + \\
& + p \exp(-\xi) \frac{\sin(\omega t - \xi - \theta)}{(1 + 2q + 2q^2)^{1/2}} + \\
& + \frac{G'_0}{\nu\pi} \left\{ u[1 - (u/r)^2]^{1/2} - r \cos^{-1}(-u/r) \right\} \exp(-\xi) \frac{\cos(\omega t - \xi - \theta)}{(1 + 2q + 2q^2)^{1/2}} + \\
& + \sum_{n=2}^{\infty} \frac{2G'_0}{\nu\pi} \frac{(-1)^n \exp(-\xi\sqrt{n})}{1 - n^2} \left\{ \frac{u}{n} \sin \left[n \cos^{-1} \left(\frac{-u}{r} \right) \right] + \right. \\
& \left. + r(1 - (u/r)^2)^{1/2} \cos \left[n \cos^{-1} \left(\frac{-u}{r} \right) \right] \right\} \frac{\cos(n\omega t - \xi\sqrt{n} - \theta_n)}{(1 + 2qn^{1/2} + 2q^2n)^{1/2}} \quad (A.48)
\end{aligned}$$

Appendix B

Phoenix Parameters

Phoenix can be used as an interactive or an automatic program and gives two pieces of information at each step, the histogram of the region to be processed, and the threshold in the histogram to split the region in further subregions. Phoenix is a moderately complex system with numerous execution options and variables that control the segmentation process. A set of parameters were adjusted and set up to obtain a good segmentation.

- **Maxmin** determines the lowest acceptable peak to valley height ratio expressed as a percentage. Maxmin is set to the value corresponding to a mild value 110.
- **Relarea** is the minimum acceptable percentage of total histogram area and set up to the value 10 that is a strict value.
- **Relscore** is the minimum acceptable percentage of the highest set score. This parameter is intended to eliminate poor features when better ones are available.
- **Noise** is the size of the largest area that is to be considered noise. Patches larger than noise pixels will be retained. This parameter was set to a strict value of 512.
- **Splitmin** is the parameter for which any region smaller than splitmin is declared terminal. We set splitmin to a very large number. In fact, this parameter was not useful since we limited the splitting to the first step.
- **Hsmooth** is the parameter used to smooth the feature histogram. Histogram smoothing eliminates many false cutpoints that are due to texture or digitization effects. We set hsmooth to the value 5 that corresponds to a mild smoothing that allows to see small regions in large ones.

The reader who wants to know more about those parameters can refer to [31].

Table of Symbols

SYMBOL	MEANING
a	diffusivity
a_s	azimuth angle
α	absorptivity
α_s	solar altitude angle
c_p	specific heat
δ	solar declination
E	emissive power or radiosity
E_{cd}	conducted radiation
E_{cv}	convective radiation
E_r	reflective radiation
E_{rad}	emitted radiation
ϵ	emissivity
ϵ_a	atmosphere emissivity
ϵ_s	surface emissivity
G	irradiation
G_a	diffuse radiation from the atmosphere
G_g	diffuse radiation from the ground
G_s	direct solar radiation
G_0	solar constant
h	convection coefficient
i	solar incidence angle
I	thermal inertia
k	conductivity
L	latitude
Lo	longitude
λ	wavelength
ω	angular speed of the Earth
ρ	reflectivity
ρ_m	density
σ	Stephan-Boltzman constant

s	Laplace variable
t	time
t_{sr}	time at sunrise
t_{ss}	time at sunset
T	temperature
T_a	atmosphere temperature
T_1	mean value of atmosphere temperature
T_2	amplitude of atmosphere temperature
τ	transmissivity
V_a	wind speed
x	depth in the material

Acknowledgments

This research was done in the context of the CMU Mars rover project whose principal investigators are Takeo Kanade, Tom Mitchell and William Whittaker.

I thank Takeo Kanade to give me the opportunity to conduct this research in his laboratory. I thank Eric Krotkov and Martial Hebert who provided helpful discussions and comments about this report. The CMU Image Understanding group provided helpful support.

Bibliography

- [1] R. E. Arvidson, A. B. Binder, and K. J. Jones. The Surface of Mars. *Scientific American*, 238:76–89, March 1978.
- [2] L. Audaire. Imagerie Infrarouge, Specificites, Etat Actuel, Evolution Previsible. In *Opto 88*, pages 491–495, 1988.
- [3] J. Bares, M. Hebert, T. Kanade, E. Krotkov, T. Mitchell, R. Simmons, and W. Whittaker. An Autonomous Rover for Planetary Exploration. *IEEE Computer*, 22:18–26, June 1989.
- [4] P. J. Besl. *Surfaces in Range Image Understanding*. Springer Verlag, 1988.
- [5] I. N. Bronshtein and K. A. Semendyayev. *Handbook of Mathematics*. Verlag Harri Deutch, 1979.
- [6] D. Brunt. *Royal Meteorological Society*, 58:389, 1932.
- [7] C. Caillas. Imaging Sensing to Identify Footfall Positions for a Legged Robot. In *Proc. of the Second Workshop on Military Robotic Applications*, Kingston, Ontario, August 1989. Organized by the Royal Military College of Canada and the Defence and Civil Institute of Environmental Medicine.
- [8] C. Caillas, M. Hebert, E. Krotkov, I. S. Kweon, and T. Kanade. Methods for Identifying Footfall Positions for a Legged Robot. In *Proc. IEEE International Workshop on Intelligent Robots and Systems*, pages 244–250, Tsukuba, Japan, September 1989.
- [9] H. S. Carslaw and J. C. Jaeger. *Conduction of Heat in Solids*. Oxford Science Publications, Second edition, 1959.
- [10] O. Chanhee, N. Nandhakumar, and J. K. Aggarwal. Integrated Modelling of Thermal and Visual Image Generation. In *CVPR*, Computer and Vision Center, The University of Texas at Austin, June 1989.
- [11] A. J. Chapman. *Fundamentals of Heat Transfer*. Macmillan, 1987.

- [12] J. Y. Coester. Technologies Infrarouges. *L'Onde Electrique*, 68(2):40–44, Mars 1988.
- [13] R. F. Craig. *Soil Mechanics*. Van Nostrand Reinhold, Fourth edition, 1987.
- [14] M. J. Daily, J. G. Harris, and K. Reiser. Detecting Obstacles in Range Imagery. In *Image Understanding Workshop*, Los Angeles, 1987.
- [15] A. M. Flynn. Combining Sonar and Infrared Sensors for Mobile Robot Navigation. *International Journal of Robotics Research*, 7(6):5–14, December 1988.
- [16] U. Grigull and H. Sander. *Heat Conduction*. Springer Verlag, 1984. translated by J. Kestin.
- [17] G. G. Gubareff, J. E. Janssen, and R. H. Torborg. *Thermal Radiation Properties Survey*. Honeywell Research Center, Second edition, 1960.
- [18] M. Hebert. Outdoor Scene Analysis Using Range Data. In *IEEE International Conference on Robotics and Automation*, San Francisco, pages 1426–1432, April 1986.
- [19] M. Hebert, C. Caillas, E. Krotkov, I. S. Kweon, and T. Kanade. Terrain Mapping for a Roving Planetary Explorer. In *IEEE Robotics and Automation Conference*, Scottsdale, Arizona, May 1989.
- [20] M. Hebert, K. Ikeuchi, T. Choi, and H. Delingette. A Perception and Manipulation System for Collecting Rock Samples. In *Proc. of the Workshop on Space Operations Automation and Robotics (SOAR '90)*, To appear, June 1990.
- [21] M. Hebert, T. Kanade, and I. Kweon. 3-D Vision Techniques for Autonomous Vehicles. Technical Report CMU-RI-TR-88-12, The Robotics Institute, Carnegie Mellon University, 1988.
- [22] S. L. Hess, R. M. Henry, C. B. Leovy, J. L. Mitchell, and J. E. Tillman. Scientific Results of the Viking Missions. *Science*, 194:1274–1353, Decembre 1976.
- [23] J. C. Jaeger. The Surface Temperature of the Moon. *Australian Journal of Physics*, 6:10–21, November 1952.
- [24] K. L. Jones, R. E. Arvidson, E. A. Guinness, S. L. Bragg, S. D. Wall, C. E. Carlston, and D. G. Pidek. One Mars Year: Viking Lander Imaging Observations. *Science*, 204:799–806, May 1979.
- [25] A. K. Khattry, M. S. Sodha, and M. A. S. Malik. Periodic Variation of Ground Temperature with Depth. *Solar Energy*, 20:425–427, 1978.

- [26] H. H. Kieffer, T. Z. Martin, A. R. Peterfreund, B. M. Jakosky, E. D. Miner, and F. D. Palluconi. Thermal and Albedo Mapping During the Viking Primary Mission. *Geophysical Research*, 82(28), September 1977.
- [27] S. A. Klein. Calculation of Monthly Average Insolation on Tilted Surfaces. *Solar Energy*, 19:325–329, 1977.
- [28] J. F. Kreider and F. Kreith. *Solar Energy Handbook*. Mc Graw Hill, 1981.
- [29] P. K. F. Kuhfittig. *Introduction to the Laplace Transform*. Plenum Press, 1978.
- [30] I. Kweon, M. Hebert, and T. Kanade. Sensor Fusion of Range and Reflectance Data for Outdoor Scene Analysis. In *Proc. of Second Annual Workshop on Space Operations Automation and Robotics (SOAR '88)*, 1988.
- [31] K. I. Laws. The Phoenix Image Segmentation System: Description and Evaluation. Technical Report 289, SRI International, December 1982.
- [32] J. W. Lucas. *Thermal Characteristics of the Moon*, volume 28. Jet Propulsion Laboratory, 1972.
- [33] T. R. Meyer and C. P. McKay. The Resources of Mars for Human Settlement. *Submitted to the J. British Interplanetary Soc*, September 1988.
- [34] H. J. Moore, R. E. Hutton, R. F. Scott, C. R. Spitzer, and R. W. Shorthill. Surface Materials of the Viking Landing Sites. *Geophysical Research*, 82(28), September 1977.
- [35] N. Nandhakumar and J. K. Aggarwal. Multisensor Fusion for Scene Perception - Integrating Thermal and Visual Imagery. Technical Report TR-87-9-41, Computer and Vision Research Center, The University of Texas at Austin, August 1987.
- [36] D. J. Norris. Solar Radiation on Inclined Surfaces. *Solar Energy*, 10(2):72–76, August 1965.
- [37] G. L. Orlove. Practical Thermal Measurement Techniques. In *Proc. of SPIE*, vol. 371, pp. 72–81, 1982.
- [38] J. C. Perrin. Principes Generaux des Cameras Thermiques. *L'Onde Electrique*, 68(2):45–52, Mars 1988.
- [39] N. Robinson. *Solar Radiation*. Elsevier Publishing Company, 1966.
- [40] W. M. Rohsenow, J. P. Hartnett, and E. N. Ganic. *Handbook of Heat Transfer, Fundamentals*. Mc Graw Hill, Second edition, 1985.

- [41] L. A. Salomone, W. D. Kovacs, and H. Wechsler. *Thermal Behavior of Fine-Grained Soils*. U.S Department of Commerce. National Bureau of Standards, 1982.
- [42] R. F. Scott. Heat Exchange at the Ground Surface. Technical Report II-A1, U.S. Army Material Command, Cold Regions Research and Engineering Laboratory, Hanover, New Hampshire, 1964.
- [43] S. A. Shafer and T. Kanade. Recursive Region Segmentation by Analysis of Histograms. In *Proc. of ICAASP*, pp. 1166-1171, 1982.
- [44] T. Shih. *Numerical Heat Transfer*. Hemisphere Publishing Corporation, 1984.
- [45] R. Siegel and J. R. Howell. *Thermal Radiation Heat Transfer*. Hemisphere Publishing Corporation, 1981.
- [46] E. M. Sparrow and R. D. Cess. *Radiation Heat Transfer*. Mc Graw-Hill, augmented edition, 1978.
- [47] A. J. Spiessbach. Mars Rover/Sample Return (MRSR) Rover Mobility and Surface RendezVus Studies. Technical Report Contract 958073, JPL, October 1988. Martin Marieta Final Report.
- [48] A. K. S. Thakur and M. Musa Momoh. Temperature Variation in Upper Earth Crust to Periodic Nature of Solar Insolation. *Energy Conversion Management*, pages 131-134, 1982.
- [49] C. E. Thorpe and T. Kanade. Carnegie Mellon Navlab Vision. In *Proc. of DARPA Workshop of Image Understanding*, pages 273-282, 1989.
- [50] J. Turck. Les Bases de la Detection Infrarouge. *L'Onde Electrique*, 68(2):36-39, Mars 1988.
- [51] F. M. White. *Heat and Mass Transfer*. Addison Wesley, 1988.
- [52] J. R. Williams. *Passive Solar Heating*. Ann Arbor Science, 1983.
- [53] G. J. Zissis and W. L. Wolfe. *The Infrared Handbook*. Office of Naval Research, Department of the Navy, Washington, DC, 1978.
- [54] D. Zuk, F. Pont, R. Franklin, and V. Larrowe. A System for Autonomous Land Navigation. Technical Report IR-85-540, Environmental Research Institute of Michigan, Ann Arbor MI, 1985.